A Search for Star-Forming Galaxies at High Redshift

Isabelle Mary Parkes

Presented For the Degree Of Doctor of Philosophy

at the University of Edinburgh,

1994.

This thesis is solely my own composition, except where specifically indicated in the text.

Isabelle Parkes,
February 1994.

ACKNOWLEDGEMENTS

The IRCAM search was originally conceived by Bob Joseph and Chris Collins. Chris has been my supervisor throughout the project. I am very grateful for his counsel and support over these last three years. All the best, Chris, for your move to Liverpool.

I thank all those who helped with the technical aspects of the project. I am grateful to the UKIRT staff for making service observations with CGS4, and to Phil Puxley and Suzie Ramsay for their help with the reduction of CGS4 data. Karl Glazebrook supplied much of the software used in the data reduction, also valuable advice and insight into all matters cosmological. Lance Miller helped on the finer matters of statistics. I am much indebted to Phil James for his frequent advice and comments on my work. Phil and Chris tirelessly read through previous drafts of this thesis. Thank you both.

My stay in Edinburgh was made special by the students and staff of the Royal Observatory, and by all the inhabitants, past and present, of Merchiston Crescent. I thank Peter Brand for his role as University supervisor. My dear friends Ruth and Phil, thank you for the fun times. May there be many more! I am also very grateful to Durham University, the staff and the students, for making me so welcome following my move south of the border. Thank you Kath for introducing me to the opera, and for having an equally irresponsible approach to expenditure. I will always remember our Bowburn days. I thank my family; Dad, Julie, Jez, Cathy, Pete, and the little ones, for their encouragement throughout the last three years and for giving me a marvellous Cornish welcome on my trips home.

Turning to the ever crucial matter of funding, I acknowledge the support of a SERC studentship. I am also grateful to my Dad for his generous gifts in times of particular financial hardship.

Finally, Richard, to you I owe everything. Your love and encouragement over these eight years has been a great source of strength for me. I can only ask that the future holds as much happiness as you have already brought to my life.

The groundhog days are over!

ABSTRACT

This thesis describes the first search for star formation in primeval galaxies (PGs) at redshifts $z \geq 7$. Our method was to undertake deep near-infrared imaging in the J window ($\sim 1.0 - 1.5\mu$m) using four narrowband filters of 2% FWHM. Over an area of sky of $3.0\square'$, no emission line object was found to a sensitivity limit of $\approx 10^{-18}$ Wm^{-2}. Interpreting this limit in terms of a limit on Lyα emission, it has been possible to place the first constraints on star formation at redshifts $7 \leq z \leq 9$. The search is also sensitive to other emission lines at lower redshifts, of particular interest are the constraints placed on Hα emission. This line is a direct tracer of star formation (Kennicutt et al., 1987) and, at the wavelengths of the narrowband filters, it probes redshifts $0.5 \leq z \leq 0.9$. Constraints on the star formation rate at these redshifts are of great interest in the interpretation of the excess of faint blue objects seen in number counts (Tyson 1988, Lilly et al. 1991, Metcalfe et al. 1991, Jones et al., 1991).

By assuming that there is no evolution in the comoving number density of galaxies out to $z = 9$, and that the luminosity function of objects at these redshifts can be represented by a Schechter function, it is possible to use the limits of the IRCAM search to place constraints on the characteristic Lyα luminosity L^*(Lyα) of PGs. Two extremes for the bright phase $\Delta t_{\rm bright}$ of each galaxy are considered. In Case 1, $\Delta t_{\rm bright}$ spans the four narrowband filters ($\sim 10^8$ years). In Case 2, the bright period is much shorter, and the specific case of the Partridge & Peebles (1966) model is considered ($\Delta t_{\rm bright} = 3 \times 10^7$ years). The 95% confidence limits for Case 1 models constrain L^*(Lyα) to less than 1.6×10^{37} W $- 4.2 \times 10^{37}$ W, depending on the cosmological model. These limits are consistent with the Case 1 predictions for Lyα luminosity. For the model of Partridge & Peebles (Case 2), the predicted PG luminosity is $L^*(\text{Ly}\alpha) = 2 \times 10^{38}$ W. Assuming that at least some galaxies are in their luminous phase in each filter then, for high values of H_0, this luminosity is inconsistent with the IRCAM limits. For $H_0 = 75 \text{kms}^{-1}\text{Mpc}^{-1}$, luminosities greater than $\sim 1 \times 10^{38}$W are ruled out at the 95% confidence level. For low values of H_0 however, the predicted PG luminosity is consistent with the limits. Greater areal coverage would enable the models to be more severely constrained, particularly as the effects of dust would further weaken the constraints.

Using the $H\alpha$ limits it is possible to constrain star formation rates in the merging model of Broadhurst et al. (1992). Assuming a constant star formation rate over the redshift range $0.52 \leq z \leq 0.92$ then, for their best fit model, characteristic star formation rates greater than $12\,\text{M}_\odot$ yr^{-1} ($q_0 = 0.5$, $h_{50} = 1.0$) can be ruled out at the 95% confidence level. This constraint tightens for lower values of q_0 and for higher values of H_0. These are very powerful constraints, since the local star formation rate is typically 3-10 M$_\odot$ yr^{-1} for normal spirals, rising to $20\,\text{M}_\odot$ yr^{-1} in the more active spiral galaxies. If galaxy formation follows a merging scenario to $z = 0.9$ then the galaxies at these redshifts cannot be forming stars at a rate any greater than that observed locally.

In memory of my mother,
Joan Parkes

Contents

Chapter 1

Introduction

This thesis describes the first search for young star forming galaxies at very high redshifts, $z \geq 7$. Because the physics involved in the formation of galaxies is highly uncertain and embraces many astrophysical processes — such as star formation, the evolution of large scale structure and the cosmology of the early universe — the detection of a such a population of young, primeval galaxies would be of extreme importance to many branches of astronomy. Cosmological implications of a detection would reach as far as the field of particle physics. Despite several claims of objects exhibiting some of the peculiarities of young galaxies, it is generally recognised that a population of primeval galaxies (PGs) remains unfound.

Searches have been made for PGs for over 25 years, none have been successful. The majority of the searches have concentrated on looking for an emission line thought to be characteristic of a first generation of star formation, the Lyα line at 1215$\AA$. These searches have for technological reasons been limited to searching the optical window, corresponding to Lyα emission from redshifts $2 \leq z \leq 6$. By using infrared technology it has become possible to search for Lyα emission from PGs at $z \geq 7$.

In addition to searching for PGs via their Lyα line, the project is also sensitive to star formation at lower redshifts, $0.5 \leq z \leq 0.9$, by means of the Hα emission line. Even if no emission line objects are found, both the constraints on Hα emission and on Lyα emission will be of great relevance to models of galaxy formation and evolution.

Thesis Organisation

The thesis is divided into six chapters.

Chapter 1 provides a general introduction to the thesis.

Chapter 2 lays the astronomical background to the search, reviewing models of galaxy formation and describing the expected characteristics of a primeval galaxy. The importance of discovering a primeval galaxy population is discussed. Previous searches are described, and the motivation for a high redshift search is justified.

Chapter 3 describes the IRCAM search. Design considerations, instrumentation details, and particulars of the observations and of the data reduction are given. The final reduced IRCAM images and details of the two candidate PGs are presented.

Chapter 4 describes the followup investigation of the PG candidates using CGS4. Details of the observations and of the data reduction are given. The reduced spectra of the candidates are presented.

Chapter 5 uses the limits of the IRCAM search to constrain Lyα emission at $7.2 \leq z \leq 9.3$ and to constrain Hα emission at $0.52 \leq z \leq 0.90$. Corresponding limits on the star formation rate at these redshifts are calculated. The Lyα limits are used to constrain models of formation in which there is no evolution in the comoving number density of galaxies. The Hα limits are used to constrain models of galaxy merging.

Chapter 6 summarises the implications of the Lyα and Hα limits for models of galaxy formation and evolution. Future developments in the quest for primeval galaxies are proposed.

Chapter 2

Cosmology and Primeval Galaxies

This chapter provides the astronomical background to the searches, starting with a description of the standard cosmological model and predictions for the growth of structure on all scales, moving on to models of galaxy formation and the expected characteristics of the primeval galaxy. Previous primeval galaxy searches are reviewed, and the relative merits of the techniques used in these searches are considered. An explanation for the failure of the searches to date is provided, and the motivation for a new high redshift search is justified.

2.1 The Standard Model

The model used most commonly to describe the early evolution of the Universe is known as the Standard Model, and it is this model that will be used throughout this thesis. In the Standard Model, the Universe is homogeneous and expanding, and its dynamics are described by Einstein's general relativity theory. The Standard Model Universe expanded from a hot, dense state where its mass was dominated by thermal blackbody radiation. It is frequently named the hot Big Bang model.

The Standard Model is based on a powerful assumption known as the Cosmological Principle. The Cosmological Principle states that to all observers, looking from any galaxy, the Universe appears homogeneous and isotropic. The Cosmological Principle satisfies the very fundamental belief, known as the Copernican Principle, that the location of our Galaxy in the Universe is not special. For the Universe to be homogeneous every fundamental observer (defined as being at rest with respect to the local Universe) must see the same general picture of the Universe as a function of time. Every fundamental observer is equivalent to every other, and the Universe seen by each looks the same as the Universe seen by us.

For the Universe to be isotropic it must look the same to a fundamental observer in what ever direction he chooses to look. The most convincing evidence for an isotropic Universe is the smoothness of the microwave background radiation. On angular scales of 10^o the microwave background is isotropic to 1 part in 10^5 (Smoot et al. 1992), indicating that at least in the early stages of its evolution the Universe was highly isotropic. Isotropy together with the Copernican Principle implies homogeneity. Homogeneity on the other hand does not require isotropy. Homogeneity can never be strictly tested.

The most general metric in a spatially homogeneous and isotropic spacetime is the Robertson-Walker Metric (see Longair 1984);

$$\mathrm{d}s^2 = \mathrm{d}t^2 - \frac{R^2(t)}{c^2}[\mathrm{d}r^2 + \Re^2 \sin^2(r/\Re)(\mathrm{d}\theta^2 + \sin^2\theta \mathrm{d}\phi^2)] \,, \qquad (2.1)$$

where the spatial coordinates are measured with respect to the frame of reference of a fundamental observer. $R(t)$ is the scale factor describing the dynamics of the Universe, and the constant $\Re$ is given by $\Re = \sqrt{1/K}$ where K is the spatial curvature of the

Universe at the present epoch. For a uniformly expanding Universe

$$x = R(t)r \ , \tag{2.2}$$

where x is the proper distance. It follows that

$$\frac{\mathrm{d}x}{\mathrm{d}t} = \frac{\dot{R}}{R}x \ . \tag{2.3}$$

This relation between recessional velocity and distance is known as Hubble's Law, an empirical relationship discovered by Edwin Hubble in the 1920's;

$$v(t) = H_0(t)x \ , \tag{2.4}$$

where H_0 is the Hubble constant, defining the expansion rate of the Universe. Its value at the present time probably lies in the range of $50 \leq H_0 \leq 100$ kms^{-1}Mpc^{-1}. The main source of uncertainty in the value of H_0 lies in making distance measurements of galaxies.

Combining the Robertson-Walker metric with Einstein's general theory of relativity allows a description to be made of the dynamics of the evolving Universe, the parameters of which govern the origin and ultimate destiny of the Universe. For a gas with pressure p Einstein's field equations are

$$\ddot{R} = -\frac{4\pi GR}{3}\left(\rho + \frac{3p}{c^2}\right) + \left[\frac{1}{3}\Lambda R\right] \ , \tag{2.5}$$

$$\dot{R}^2 = \frac{8\pi G\rho}{3}R^2 - Kc^2 + \left[\frac{1}{3}\Lambda R^2\right] \ . \tag{2.6}$$

The terms in square brackets are associated with the cosmological constant Λ which represents the vacuum energy density of the Universe. The cosmological constant was introduced by Einstein in an attempt to produce a static Universe. Non-zero values of Λ have been reincarnated several times, particularly to explain the discrepancy between the age of the Universe indicated by the value of H_0 and by the age of the oldest stars in globular clusters (Gunn & Tinsley 1975). The calculations that follow assume $\Lambda = 0$.

Substituting the present day values of R and $\dot{R}$ ($R = 1$, $\dot{R} = H_0$) into Equation 2.6 and introducing a critical density $\rho_c = 3H_0^2/8\pi G$, and a density parameter $\Omega = \rho_0/\rho_C$ then the spatial curvature of the Universe is

$$K = \frac{\Omega - 1}{c^2/H_0^2} \ . \tag{2.7}$$

The parameter Ω is the ratio of the mean density to the density at which gravity is just strong enough to cause the expansion of the Universe to halt and eventually to collapse. If $\Omega > 1$ the geometry is spherical, if $\Omega < 1$ the geometry is hyperbolic, and if $\Omega = 1$ the geometry is flat (zero curvature). The deceleration parameter q_0, defined by

$$q_0 = -\frac{\ddot{R}(t_0)}{\dot{R}^2(t_0)} = 1/2\Omega \tag{2.8}$$

determines the deceleration of the Universe at the present epoch.

Consider the fate of the Universe when R becomes very large ($R \to \infty$). Then from Equation 2.6

$$\dot{R}^2 = H_0^2(1 - \Omega) \tag{2.9}$$

In the case $\Omega = 1$, $\Lambda = 0$ (known as the Einstein-de Sitter model) this gives

$$t_0 = \frac{2}{3H_0} \tag{2.10}$$

i.e. $t_0 = 6.5 - 13 \times 10^9$ years. A major problem in modern cosmology is how to reconcile this range with the age of the oldest globular stars in the halo of our Galaxy of $16 \pm 2 \times 10^9$ years (Demarque et al. 1991). One possible explanation (Turner 1993) is that the local expansion rate differs significantly from the global rate, such a difference could result in measurements of H_0 higher than the global value.

2.1.1 Challenges for the Standard Model

Support for the Standard Model is considerable, for example it can explain the observed Hubble expansion, the existence of the microwave background radiation and its Planckian spectrum, and the origin of the light elements. Heavy elements such as carbon, nitrogen and oxygen are produced prolifically in nuclear reactions in centres of stars. It is however hard to produce light elements such as D, ^{2}He, ^{3}He, and ^{7}Li by stellar nucleosynthesis, as these are fragile elements rapidly destroyed in the cores of stars. Detailed computations of element production have shown that the elements produced in the Big Bang are exactly those difficult to account for by stellar nucleosynthesis. The observed light element abundances can be reproduced for a baryon density of $\Omega_B = 0.013 \pm 0.003h^{-2}$ (Walker et al. 1991).

The Standard Model does however leave a number of problems. The first problem is generally known as the *flatness problem*. In the Standard Model, for the value of Ω_0 to

be close to unity it must at early times have been extraordinarily close to unity. Even taking a conservatively low value for the present density, $\Omega_0 = 0.01$ say, then at the Planck time (the epoch at which general relativity breaks down due to quantum effects, $t_{\rm pl} = \sqrt{hG/c^5} = 10^{-43}$ s) the density would have been $|\Omega - 1| \sim 10^{-61}$. Whatever the nature of the initial conditions of the Universe, Ω was very finely tuned to unity. Why should this be?

The second problem, the *horizon problem*, relates to the observed large scale uniformity of the Universe. COBE observations of the microwave background radiation have revealed it to be extremely isotropic on large angular scales. After removing the dipole moment caused by the motion of the Earth relative to the radiation, variations in the temperature of the background are very small. The rms quadrupole amplitude $\Delta T/T$ is $\approx 5 \times 10^{-6}$ (Smoot et al. 1992). Now the microwave background radiation originates from the surface of last scattering (z=1000), when protons and electrons combined to form hydrogen and the Universe became optically thin. In the standard Big Bang model, patches of sky $> 2^\circ$ apart could never have been in causal contact. This means that the high isotropy in temperature seen in the quadrupole cannot be created by any equilibrium process. The problem is that the large-scale uniformity of the Universe cannot be explained by the Big Bang model but must be interpreted in terms of the initial conditions.

Another problem concerns the origin of the density fluctuations that have given rise to structures such as galaxies and galaxy clusters. In order for these structures to have evolved the early Universe must have contained a spectrum of density fluctuations. These primordial perturbations, whose large-scale imprint on the cosmic background radiation have now been detected by COBE, are not explained by the Big Bang theory and must be imprinted in the initial conditions. This is the *structure problem.*

Motivated by these and other problems Guth in 1981 proposed the inflationary Universe scenario. The key ingredient of an inflationary Universe is the occurrence of a phase transition shortly after the Planck time. In this scenario, the Universe experienced a brief period of extremely rapid expansion — what was a very small initial volume was inflated up to the entire observable Universe of today. Sources of the microwave background from all regions of the sky were once in causal contact and so had time to reach a common temperature before inflation, accounting for the horizon problem. Inflation can

also lead to a prediction for the spectrum of initial perturbations from quantum fluctuations (e.g. Bardeen et al. 1983), solving the structure problem. Another success is that the period of inflation drives the value of Ω very accurately to 1, no longer requiring the initial value to be fine tuned. Inflation has been very successful in explaining broad properties of the Universe.

2.1.2 Dark Matter

Inflationary models make some robust predictions. One such prediction is that assuming that the cosmological constant is either zero or negligible, the present density of the Universe equals the critical mass density to a high degree of accuracy. Results from various determinations of value of Ω_0 are summarised in Table 2.1. On large scales, there is some observational evidence to support a high Ω_0 Universe. For example from a sparse sampled redshift survey of IRAS galaxies, Rowan-Robinson et al. (1990) determine the gravitational acceleration that would drive the large-scale velocity field of the Local Group. They find a value of $\Omega_0 = 0.7$ $(+0.3, -0.2)$ assuming that the IRAS galaxy distribution traces the total mass, though other authors have suggested that the value determined for Ω in this way should be considered as an upper limit (Plionis et al. 1993).

At the very least, the comparison between the luminous and dynamical mass in galaxies indicates the presence of some form of dark mass in galaxies. Estimates made from the visible light in a galaxy are an order of magnitude less than the dynamic estimates made from their rotation curves (see Table 2.1). Once the presence of some dark matter has been established it is not unreasonable, although a measure of expedience, to consider the possibility of more dark matter outside galaxy systems, of sufficient density to bring Ω_0 up to unity.

The nature of the dark matter is not clear. Primordial nucleosynthesis indicates that Ω_B the density in baryons is $\Omega_B = 0.013h^{-2}$. Although it is possible for this value of Ω_B to be raised, for example by an inhomogeneous primeval baryon distribution, it is hard for the value to be increased sufficiently to match the large scales observational results. If $\Omega_0 = 1$ then some other, non baryonic form of matter must account for the discrepancy between Ω_B and Ω_0. The nature of this non baryonic dark matter has been a matter of great debate. Before 1980 dark matter was usually assumed to be baryonic matter in not readily detectable form, for example low mass stars, gas, stellar remnants

Table 2.1: Estimates of Ω_0 compiled from Rubin (1991) and Peebles (1993) ($h_{100} = H_0/100$ kms^{-1}Mpc^{-1}).

System	Approximate Scale (kpc)	Method	Ω_0
Galaxy	25	Visible light	0.002
Galaxy	25	Dynamical	0.01-0.02
Binary	50	Dynamical	0.05
Group	150	Dynamical	0.15
Cluster	250	Dynamical	0.25
Supercluster	2×10^4	Dynamical	$0.15- < 1.0$
Light elements		Estimate of density of baryons from Big Bang nucleosynthesis	$0.013 \pm 0.005 h_{100}^{-2}$

such as white dwarfs and neutron stars, or black holes. Then the idea that some of the dark matter might be of non baryonic form triggered particle physicists to suggest a host of exotic dark matter candidates. The candidates can be classified into two main types, differentiated by the thermal energy of the particles.

Hot Dark Matter

One of the first candidates for dark matter was the neutrino with a mass of a few tens of eV. This has the advantage that the neutrino is known to exist, although it is not established if it has mass. The characteristic of hot dark matter (HDM) particles is that they have low rest mass and hence are relativistic at early times. Relativistic velocities damp out formation of small-scale structures in the early Universe and consequently the first structures to form in this scenario are large pancakes of $\sim 40(\mathrm{m}_\nu/30\mathrm{eV})^{-1}$ Mpc, sizes characteristic of a galaxy supercluster. Smaller structures such as galaxies form by subsequent fragmentation of the pancakes, in what is designated a 'top down' cosmology. These cosmologies been found to have severe difficulties regarding the formation of galaxies. It is difficult to arrange for galaxies to form a reasonable time before the

present without making the Universe excessively inhomogeneous on large scales (White et al. 1983). To reproduce the observed galaxy-galaxy correlation function requires the epoch of 'pancaking' to have happened at relatively recent times, $z \leq 1$. This is difficult to reconcile with the many galaxies with redshifts $z \geq 1$ and indeed with the numbers of quasars at $z \geq 3$ (Frenk et al. 1983).

Cold Dark Matter

In the mid 1980's it was realised that many other particles — whose existence, although unconfirmed, was predicted by elementary particle physics — can provide features for galaxy formation that are more attractive than those offered by HDM scenarios. These particles have low velocities achieved either from thermal particles with a high rest mass, for example gravitinos, or from lighter particles with momenta well below kT, such as axions. A host of CDM particles have been proposed. As well as the axion and gravitino there is the photino, the scalar neutrino, the Higgsino and many others.

The growth of structure in a CDM Universe is hierarchical; smaller objects gathering to form progressively larger structures. It predicts that at $z \sim 50/b$, where b defines the amount of bias (see below), much of the hydrogen in the Universe is in gravitationally bound gas clouds with masses comparable to the Jeans mass $M_J \sim 10^5\,M_\odot$. These gas clouds then group together to form the galaxies of today. In general, CDM models predict that galaxies formed late in the history of the Universe, at redshifts $z \sim 2 \pm 1$ (Baron & White 1987, Silk & Szalay 1987). Note that in these models the epoch of galaxy formation is identified with the peak merging epoch.

The standard CDM model assumes an Einstein-de Sitter Universe ($\Omega = 1, h_{100} \sim 0.5$) in which baryonic matter represents only a small fraction of the total mass density. Non baryonic dark matter is assumed to be initially cold, and structure is assumed to grow out of scale-invariant, adiabatic, gaussian fluctuations. In adiabatic scenarios the initial local value of the entropy conserved per quantum number is a universal number, which means that the number of photons, baryons and all other contributions to the mass density fluctuate together. Scale invariance means that the rms mass fluctuation $\delta = \delta M/M$ on the scale of the Hubble length (c/H) is independent of redshift. The normalisation of the spectrum is a free parameter. The model also makes assumptions as to how the dark matter in the Universe is distributed: initial computations assumed that galaxies trace

the distribution of dark matter but this has since been modified to adopt the concept known as biasing, whereby galaxies are more strongly clustered than the underlying dark matter distribution. This appropriation was necessary to reconcile the assumption of $\Omega_0 = 1$ with the dynamical estimates of Ω_0, and was inspired (Kaiser 1984) by the observation that clusters of galaxies cluster more strongly than do galaxies.

Although the CDM model can provide a close match to many observations — it can produce objects of galactic mass and can reproduce small-scale clustering and internal dynamics of galaxies (Blumenthal et al. 1984) — the model fails to match the observed large-scale coherence in the galaxy distribution (Maddox et al. 1990, Saunders et al. 1991, Collins et al. 1992) and underestimates the cluster-cluster correlation length (Bahcall & Soneira 1983). Many modifications to the basic CDM model have been suggested in an attempt to overcome these discrepancies. Non gaussian initial perturbations, strings, textures, explosions, tilted spectrum, non-zero Λ, and particularly hybrid models in which cold and hot dark matter are mixed have all produced varying degrees of success.

2.1.3 Forming Galaxies

One of the biggest problems in modern cosmology is how to explain the formation of structure; the galaxies, clusters and superclusters that make up today's Universe. How did the Universe evolve from the low amplitude, large-scale fluctuations detected by the COBE satellite at $z \sim 1000$ to the structures on all scales that we see about us today? Comparing the predictions of cosmological models with the observed properties of galaxies is an extremely complex process. Cosmological models tell us about the evolution in the distribution of mass, not about the formation and evolution of galaxies. As well as having to assume the physics involved in the formation of the galaxies, any comparison must take into consideration subsequent stellar evolution and the effects on the galaxy of its environment.

An alternative route would be to study the galaxies at their very youngest age, before environment and the progression of time have modified their appearance. If we could establish when galaxies started to form, observe their physical properties and ultimately determine how they are distributed in space, we would have found a vital link in understanding the formation and evolution of structure in the Universe.

The aim of this thesis is to detect such a population of primeval galaxies (PGs). The remaining half of this Chapter establishes the expected appearance of PGs, and gives an explanation for the failure of PG searches to date, namely that all sample too low a redshift space. The discovery of a PG population at a high redshift would manifest severe difficulties for both CDM and HDM models, as both predict the relatively late formation of stars. As we shall see there is much empirical evidence to suggest a high redshift of galaxy formation.

2.2 A Model of a Primeval Galaxy

Primeval galaxies are defined as being the high redshift progenitors of the local galaxy population, so young that they are forming the bulk of their first generation of stars. This definition is very much from the observer's prospective; it is while young galaxies are forming the bulk of their stars that we might expect them to be at their most luminous and therefore most detectable stage. More esoteric definitions are possible, such as PGs as being objects in which the dark halos are assembling or in which the density fluctuations are turning around from the general expansion of the Universe, but these are more suited to theoretical simulations than to observational searches.

There are two major processes involved in the formation of a galaxy: the assembly of its mass via gradual infall or mergers, and the conversion of its gas into stars. In the simplest scenario, initial density perturbations give rise to over densities with masses on galaxy scales, whose subsequent gravitational collapse triggers the first generation of star formation. It is possible, for example in CDM scenarios, that the perturbations are subgalactic in scale in which case the situation is more complicated, with galaxies forming from mergers of smaller (and possibly collapsed) subunits. These mergers may trigger subsequent star formation. The following discussions assume that the galaxy mass is assembled prior to gravitational collapse, the consequences of merging are however an important issue and will be considered to some depth in Chapter 5.

A very simplified model of galaxy formation is illustrated in Figure 2.1. Space is expanding in the aftermath of the Big Bang. Small over dense regions of early Universe are expanding too, though at a slower rate because of their enhanced gravity. This retarding of growth makes the regions progressively more dense relative to their surroundings

and their expansion is slowed even more. Eventually local gravitational forces overcome the expansion and these protogalaxies, consisting primarily of hydrogen gas, collapse releasing large amounts of energy and triggering the first generation of stars.

2.2.1 Energetics

There are three principal energy sources of a PG; binding energy released during the PG collapse and during subsequent star formation, the energy released in nuclear burning in the primordial star bursts, and energy released in supernovae. Rough estimates of their contributions to the total energy of the PG can be made as follows.

1. Binding Energy. The binding energy of a galaxy is

$$E_{\rm bind,gal} \approx M_{\rm cool} V_{\rm D}^2 \tag{2.11}$$

where $M_{\rm cool}$ is the total mass which can cool radiatively and $V_{\rm D}$ is the velocity dispersion of the galaxy. For values typical of $z = 0$ galaxies, i.e. $M_{\rm cool} = 10^{11}\,{\rm M}_\odot$ and $V_{\rm D} = 250$ kms^{-1} this gives $E_{\rm bind,gal} \approx 10^{52}$ J. This energy may have been released via inverse Compton cooling on the microwave background, or through recombination line emission in shocks. The energy released by collapsing protostars is

$$E_{\rm bind,*} \approx \frac{G M_{\rm tot*} < M_* >}{< R_* >} \tag{2.12}$$

where $M_{\rm tot*}$ is the total mass converted to stars in the PG phase, $< M_* >$ the average stellar mass and $< R_* >$ the average stellar radius. For $M_{\rm tot*} = 10^{10}\,{\rm M}_\odot$, $< M_* >= {\rm M}_\odot$ and $< R_* >= {\rm R}_\odot$ this gives $E_{\rm bind,*} \approx 4 \times 10^{51}$ J. This would probably be mainly released in the far-infrared also, at least for the first protostars when little dust was present, in Lyα line emission.

2. Nuclear Burning. An estimate of the energy released from nuclear burning in primordial star bursts can be obtained from

$$E_{\rm nuc} \approx \epsilon M_{\rm tot*} c^2 \Delta X \tag{2.13}$$

where $\epsilon \sim 0.001$ is the average efficiency of nuclear reactions in stars (often termed the mass defect), and $\Delta X \sim 0.05$ is the fraction of hydrogen converted to helium and metals. This gives $E_{\rm nuc} \approx 10^{53}$J, which would be released mainly in the rest

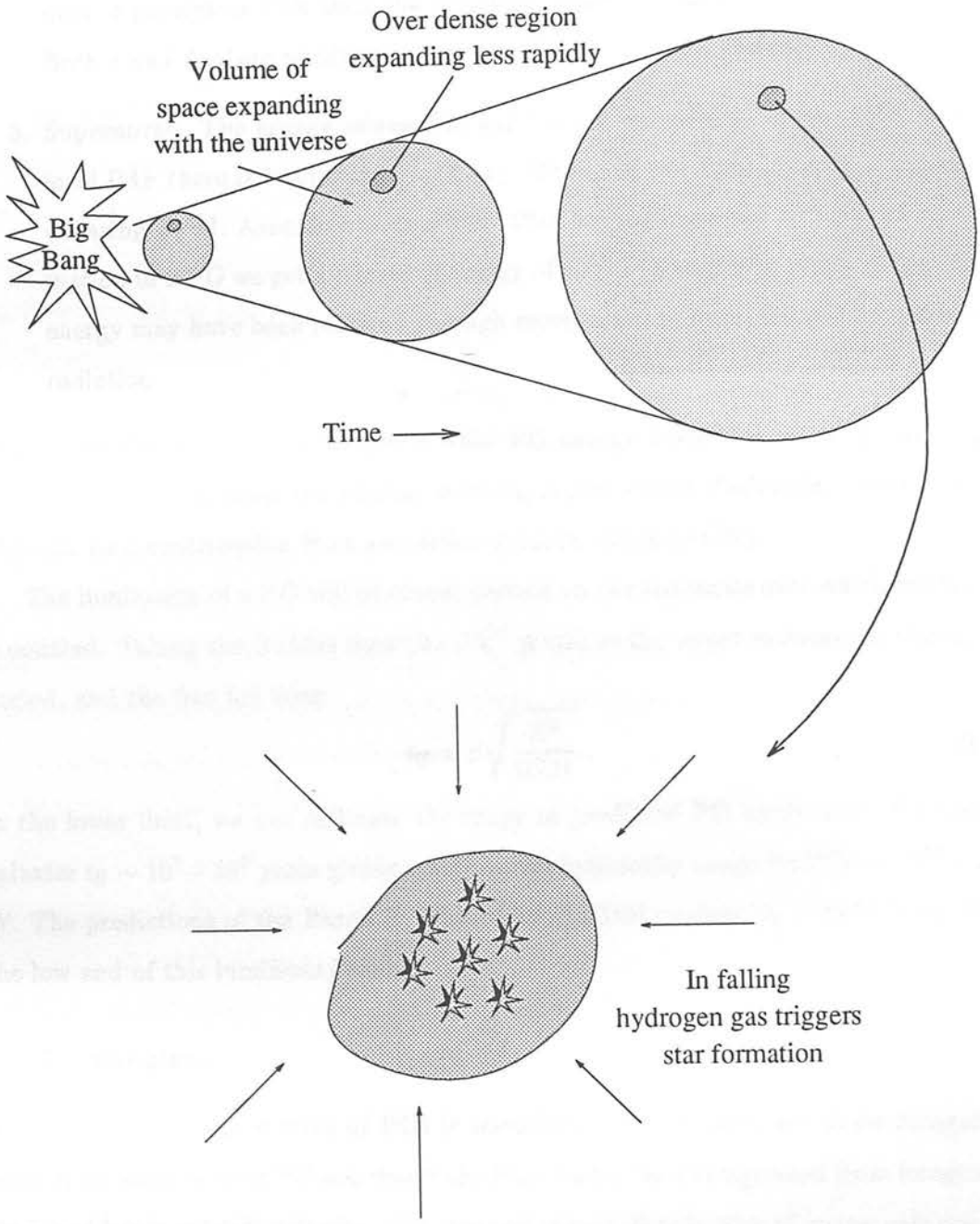

Figure 2.1: A simple model of galaxy formation.

frame UV with some fraction reradiated in recombination lines such as Lyα. If dust is present in PGs then the UV light would be degraded to the far-infrared. Both ϵ and ΔX are sensitive to the initial mass function (IMF).

3. Supernovae. The energy released in supernovae will depend on the IMF. For the local IMF there is 1 supernova for every 100 $M_\odot$ of star formation, each supernova releasing 10^{44}J. Assuming a local IMF then for the expected 10^{10} $M_\odot$ of star formation in a PG we get a release of energy of 10^{52} J (Djorgovski 1992). Some of this energy may have been released through recombination lines, the rest in continuum radiation.

These contributions add up to give a total PG energy budget of $\sim 10^{54}$J, dominated by the contribution from the nuclear burning in the initial starbursts. There may in addition be a contribution from any active galactic nuclei (AGN).

The luminosity of a PG will of course depend on the timescale over which the energy is emitted. Taking the Hubble time (2×10^{10} years) as the upper extreme for this bright period, and the free fall time

$$t_{\rm ff} = \pi \sqrt{\frac{R^3}{2GM}} \, . \tag{2.14}$$

as the lower limit, we can estimate the range in predicted PG luminosity. For normal galaxies $t_{\rm ff} \sim 10^7 - 10^8$ years giving a bolometric luminosity range for PGs of $10^{37} - 10^{40}$ W. The predictions of the Baron & White (1987) CDM models ($t_{\rm ff} \sim 10^{10}$ years) lie at the low end of this luminosity range.

2.2.2 Spectra

Some estimate of the spectra of PGs is essential if these objects are to be recognised: there is no point in deep PG searches if the PGs cannot be distinguished from foreground stars and lower redshift galaxies. The spectral energy distribution of young galaxies can be estimated from an assumed star formation rate (SFR) and initial mass function. Using a SFR obtained from Larson's (1974) hydrodynamical models and a Salpeter IMF, Meier (1976) determines the number of stars in each mass interval and then from the derived stellar population computes integrated properties for the model PG. Figure 2.2 shows the integrated stellar spectrum that he obtains. It is dominated by light from the luminous and massive O and B stars of the first starbursts, and above $\log \nu = 15.4$ appears flat.

Shortward of the Lyman limit at 912$\AA$ ($\log \nu = 15.5$) Meier predicts a large number of Lyman continuum photons, comprising 13 percent of the total galactic luminosity. No flux is predicted at energies higher than the He^{++} jump at $\log \nu$=16.1.

This spectrum assumes that absorption by interstellar gas is negligible. In fact it is likely that a large amount of hydrogen gas will be present and this will somewhat alter the PG spectrum. The effects of interstellar HI gas with a column density large enough ($N_{HI} \geq 10^{17} cm^{-2}$) to be optically thick to the Lyman continuum and to the Lyman lines are shown in Figure 2.2 by a dashed line and result in a spectrum very similar to that of the classic paper of Partridge & Peebles (1966), in which they propose that the spectrum should be similar to that of a giant HII region. The Lyman continuum from young O and B stars ionises the surrounding hydrogen gas and an appreciable fraction of the ionised electrons are subsequently reabsorbed, with photons emitted in hydrogen recombination lines, principally in the Lyα line. Other emission lines that might be expected in regions of star formation are those observed routinely in active galaxies, e.g. Hα, [OII]3727 $\AA$, [OIII]5007 $\AA$, CIV 1549 $\AA$, CIII]1909 $\AA$ and MgII 2799 $\AA$. These metal lines require significant nuclear enrichment of the interstellar medium and therefore will not be seen in the initial burst of star formation in a PG.

Most modern PG searches are for the PGs' Lyα emission. The Lyα line is expected to contain a few percent of the total luminosity of the PG, i.e. $\sim 10^{35} - 10^{38}$ W. It will be substantially stronger than the continuum flux. Partridge & Peebles predict an equivalent width of as much as 100$\AA$, recent predictions by Charlot & Fall (1993) using new models of stellar population synthesis are for equivalent widths of up to 200$\AA$. Since PGs will have velocity dispersions typical of normal galaxies (< 600 kms^{-1}), their emission lines can be discriminated from lines of other high redshift objects such as quasars by their narrow widths, less than 5$\AA$ in the rest frame.

Lyα photons emitted from young stars will suffer a large amount of resonant scatterings in the surrounding neutral atomic hydrogen. In the absence of dust this will not affect the total Lyα emission, since each Lyα photon absorbed by the HI would be re-emitted as a new Lyα photon. Resonant scattering does however increase the chance of absorption of the Lyα by any dust grains. The exact amount of attenuation is highly uncertain, as it depends sensitively on the structure of the interstellar medium. Charlot & Fall (1993) show that Lyα emission is attenuated when the dust-to-gas ratio exceeds

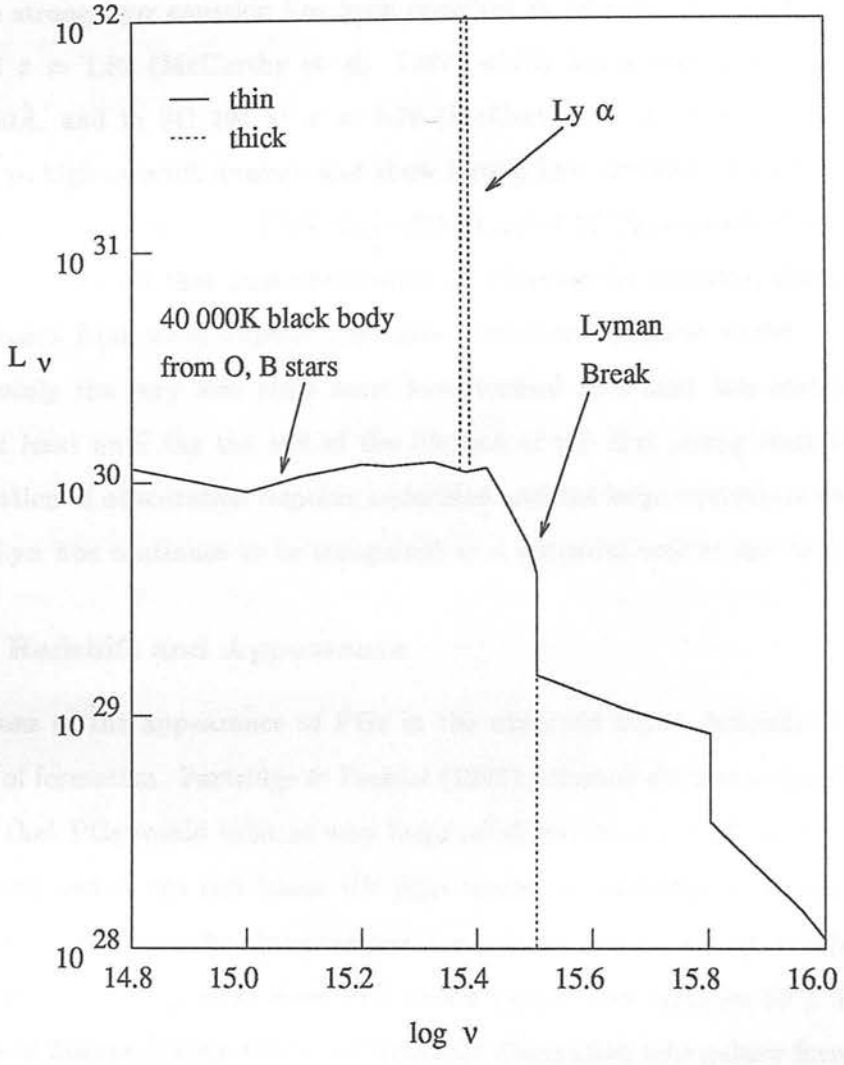

Figure 2.2: The theoretical integrated spectrum of a primeval galaxy in the rest frame, after Meier (1976). The dashed line includes the effects of interstellar hydrogen gas which is optically thick to the Lyman lines.

1-10% of the value of the Milky Way.

Lyα attenuation has been observed in some of the known high redshift objects, such as IRAS FPS 10214+4724 (Rowan Robinson et al. 1991) and in some high redshift radio galaxies (Eales & Rawlings 1993). It is unlikely that these galaxies are representative of the general galaxy population, and it is not clear that their properties can be extrapolated to a primeval galaxy population at higher redshifts (Djorgovski & Thompson 1992). For example strong Lyα emission has been observed in powerful radio galaxies such as 3C 326.1 at $z = 1.82$ (McCarthy et al. 1987) which has a rest frame equivalent width of $\geq 350\mathring{A}$, and in 3C 294 at $z = 1.79$ (McCarthy et al. 1990). Many companion galaxies to high redshift quasars also show strong Lyα emission, for example the mildly active companion galaxy to PKS 1614+051 at $z = 3.22$ (Djorgovski et al. 1987). These observations suggest that dust obscuration in PGs may be minimal, though some of the Lyα emission from these objects may come from active galactic nuclei.

Certainly the very first stars must have formed in a dust free environment which lasted at least until the the end of the lifetime of the first young stars ($\sim 10^7$ years). The question of obscuration remains undecided and the large equivalent width predicted for the Lyα line continues to be recognised as a potential tool in the detection of PGs.

2.2.3 Redshift and Appearance

Predictions of the appearance of PGs in the observed frame depends on the adopted redshift of formation. Partridge & Peebles (1966) assumed dissipationless formation and inferred that PGs would exist at very large redshifts, $10 \geq z \geq 30$, and would therefore appear very red as the rest frame UV light would be redshifted to substantially longer wavelengths. The angular-diameter distance relation turns over at a redshift of $z \approx 2$ and so for a high Ω Universe these PGs would appear very large ($\approx 30''$). In comparison the work of Larson (1974), which incorporated dissipation into galaxy formation models leads (Meier 1976) to predictions of PGs with longer, later formation, and hence lower redshifts ($z \sim 5$), bluer colours and smaller angular sizes. Later formation times are favoured by CDM models, consequently most recent models for galaxy formation have been based on low z formation. Baron & White (1987) make a detailed simulation of the inhomogeneous dissipative collapse of a PG and predict that galaxies are in their bright phase of star formation at $z \sim 2 - 3$, with 'lumpy' emission extended over at least 100

kpc, corresponding to an angular extent of $10'' - 20''$. Taking a more empirical approach, by deprojecting U, B, V galaxy colours Djorgovski (1992) proposes that the first burst of star formation in galaxies occurs at redshifts of $z > 3 - 5$, giving an angular diameter of $> 2''$ for a 30 kpc object.

2.3 High Redshift or Low: Empirical Evidence

There are many clues as to when galaxies formed, some of them conflicting. The clues come from studies of the rotation of galaxies at the present epoch, from the colours of galaxies and the evolution of the colours, from individual objects showing the characteristics of a youthful galaxy, and from the quasar population and intergalactic medium at high redshifts.

2.3.1 Spheroids and Disks

An associated question is whether disks formed before, after or at the same time as the spheroids (elliptical galaxies and bulges of spirals). Two pictures are possible: spheroids formed early by coherent collapse or by mergers of gas rich pregalactic units, disks then accreted slowly around them. Alternatively, disks formed first with ellipticals forming over a Hubble time by mergers of fully formed and largely stellar units. The clearest argument against ellipticals forming from mergers of spirals (van den Bergh 1990) is the high abundance of metal-poor globular star clusters around some giant ellipticals, as metal rich spiral galaxies tend to contain fewer globular clusters. This argument is however a matter of current debate following the detection of a population of objects which, it is claimed, have properties compatible with the hypothesis that the objects are young globular clusters formed in the merger of gas-rich galaxies (e.g. Whitmore et al., 1993).

2.3.2 Galactic Rotation

The origin of the angular momentum of galaxies provides intriguing clues for the timetable of structure formation. The rotation cannot be a relic of some unknown physics at very high redshift, as this would produce unacceptably dense objects (Jones 1973). It could be due to shocks during collapse (Chernin 1970), or stresses of a primeval magnetic field

(Wasserman 1978).

One popular view is that galaxies acquire angular momentum by the tidal torques of neighbouring protogalaxies (e.g. Doroshkevich 1970). N-body computations have shown that the amount of angular momentum acquired from tidal torques is consistent with slow rotation of spheroid components of large galaxies (Barnes & Efstathiou 1987). If disk angular momentum originated in this way then the disk material would have had to have contracted by the dissipation of energy so that the disks become rotationally supported. This gives a long collapse time for disks, and hence a low redshift of disk formation. In contrast, the moderate collapse factors indicated by the slow rotation of spheroids suggests that the large core mass densities of giant ellipticals are a result of the core material being produced at high redshifts. If it assembled at low z then a very high collapse factor would be required and the collapse would have to be remarkably uniform to match the uniformity in the core densities. We are led towards a picture in which the disk component of spirals forms after spheroids. Such a picture is supported by evidence that the disk stars in the Milky Way are younger than those in the spheroid (Winget et al. 1987, Peebles 1993), and the fact that the star distribution in disks is thin, making the disk structure fragile and indicating that the disks must have formed towards the end of any merging or accretion (Quinn & Goodman 1986).

2.3.3 Galaxy Colours and Evolution

A rough estimate of the age of galaxies can be made from their $z = 0$ colours (Djorgovski 1992). The distribution of U, B and V galaxy colours is generally bimodal with a narrow red peak corresponding to spheroids and a broader blue peak corresponding to the disks of spirals. By modelling the stellar evolution in galaxies, star formation histories can be fit to the observed colours. Although degenerate (it is hard to distinguish between the fits by the stellar continuum alone) these fits do indicate characteristic formation redshifts of $z \sim 0.5 - 2$ for the disks and $z > 3$ for the ellipticals. This suggests that the progenitors of disks are to be found out to $z \sim 2$, the progenitors of ellipticals and bulges beyond that.

Studies of the evolution in the colour of ellipticals in clusters also suggest a high redshift of elliptical formation, if star formation in PGs occurs primarily in a single burst. Aragón-Salamanca et al. (1993) obtained V, I, and K photometry of 180 K

selected early type galaxies in fields of 10 rich clusters with $0.5 \geq z \geq 0.9$. By $z \sim 0.9$, none of their cluster galaxies were as red as present day ellipticals. They found evolution consistent with the passive ageing of stellar populations that formed before $z \sim 2$ and most probably before $z \sim 5$. In addition, a remarkable similarity was found in the picture from cluster to cluster, suggesting that early type galaxies form a coeval, homogeneous population.

By selecting their sample in the near-infrared Aragón-Salamanca et al. minimise their sensitivity to secondary star bursts in the galaxies. This contrasts with the photometric study of galaxies in clusters in the redshift range $0.003 \geq z \geq 0.54$ by Butcher & Oemler (1978, 1984) in which the cluster galaxies are optically selected and hence the sample is very sensitive to recent star bursts. This study found the fraction of blue galaxies in clusters increases strongly as a function of redshift (the Butcher-Oemler effect), indicating strong recent evolution of some galaxies in clusters and perhaps a recent epoch of galaxy formation. Subsequent spectroscopy (e.g. Couch & Sharples 1987) has confirmed that these galaxies are cluster members, not chance projections, and has indicated that most of blue excess in cluster galaxies arises from systems which have experienced a burst of star formation between 0.1 and 1.5 Gyr prior to epoch of observation, while in the remainder a substantial burst appears to still be in progress. The physical origin of the Butcher-Oemler effect remains unclear. However, the blue galaxies tend to avoid the central regions of the clusters (e.g. Pickles & van der Kruit 1991) and the growing opinion is that we are witnessing star formation triggered by galaxies or groups of galaxies falling into the cluster and interacting with the cluster gas. Interestingly, the tendency of the blue galaxies to define rims around cores of the distant clusters appears to have a low redshift analogue: Caldwell et al. (1993) find that a find a large fraction (1/3) of all galaxies in a field 40' south west of the centre of the Coma cluster show evidence of star formation or nuclear activity, whereas very few such galaxies are found towards the centre of the cluster. It would seem that the Butcher-Oemler effect tells us more about the environment at the edges of clusters than about the evolution of the general galaxy population.

Since the Butcher-Oemler effect appears to tell us primarily about the evolution of galaxies caused by the environment in clusters, we must turn to the field galaxy population to investigate any truly intrinsic galaxy evolution. Here too evidence of substantial

galaxy evolution has been revealed, this time from faint optical surveys (Tyson 1988, Lilly et al. 1991, Metcalfe et al. 1991, Jones et al. 1991). The surveys show a significant excess of faint galaxy counts — as much as a factor of 5 at $b_J = 24$ — over the number expected in a Universe in which there is no evolution of galaxies.

Initial interpretations of this excess were that galaxies experienced more active star formation in the past, or that perhaps the deep counts were picking up a local population of dwarf galaxies. Such interpretations however had to be dismissed when subsequent deep redshift surveys (Broadhurst et al. 1988, Colless et al. 1990, 1993) revealed that the redshift distribution of faint galaxies brighter than $b_J = 22.5$ is entirely consistent in shape with that predicted by the no evolution model. The redshift distribution has a median redshift of $z \sim 0.4$ with no high nor low redshift tail. In addition, many of the spectra were found to be dominated by strong [OII] lines which are indicative of star bursts. This lead Broadhurst et al. to propose a model in which the faint excess is due to low luminosity galaxies which are temporarily brightened by short lived bursts of star formation. Such a model is consistent with the galaxy counts in the near-infrared which show far less significant excess above the non evolving prediction (Lilly et at. 1991, Glazebrook 1991). Since light at these longer wavelengths is predominantly from older stars it should be less affected by changes in the star formation rate than is the optical light.

The contemporary view of the nature of the faint blue objects is divided: one party (Broadhurst et al. 1992) invokes a model of galaxy merging and considers the faint blue galaxies to be the precursors of the normal population, another (Cowie 1991) calls upon a new population of star forming dwarfs which have decayed beyond detection at the present epoch. In this case the blue population tells us nothing about the underlying galaxy population. The merging model is discussed further in Chapter 5.

2.3.4 Young Galaxies

Moving now away from generalized studies of the galaxy population we turn to individual galaxies that show evidence of significant star formation or other characteristics of young galaxies. Perhaps such galaxies can give us an indication of the formation history of the galaxy population.

First, consider low redshift objects, for we know that some form of delayed galaxy

formation operates even at $z = 0$. Significant star formation rates are observed in local late type and irregular galaxies (see for example Sandage 1986) and also in dwarf galaxies, which may be undergoing their first major burst of star formation (e.g. Kunth & Sargent 1986). However, it is unlikely that these are young galaxies as almost all show an underlying old stellar population. Considerable star formation is found in nearby ultraluminous IRAS galaxies (Soifer et al. 1987), but again these dusty objects show an underlying old stellar population and are probably best thought of as undergoing some kind of transformation — perhaps through merging — rather than formation.

High redshift active galaxies have revealed several objects exhibiting properties suggestive of young galaxies. Such objects include the radio galaxy 3C 294 at $z = 1.79$ (McCarthy et al. 1990), which exhibits strong extended Lyα emission. Indeed infrared spectroscopy of a sample of radio galaxies at redshifts $2 \leq z \leq 4$ (Eales & Rawlings 1993), suggests that several high redshift radio galaxies may be young as their spectral energy distributions were found to be much bluer than previously realised. Another object of interest is the high ionisation emission line galaxy at $z = 2.29$, apparently associated with IRAS FPS 10214+4724 (Rowan-Robinson et al. 1991). It has been proposed (e.g. Elbaz et al. 1992) that this is an elliptical galaxy in formation. The radio, submillimetre, far-infrared and CO observations are consistent with a powerful starburst early in the life of a massive galaxy (Rowan-Robinson et al. 1993). Strong polarization, high excitation emission lines and its optical morphology on the other hand suggest the presence of an obscured AGN, perhaps contributing a substantial fraction of the total power (e.g. Radford et al., 1993). The likelihood that many of these high redshift 'young' objects are powered by AGN suggests that their discovery is a result of very strong selection effects, and hence that they are atypical of the galaxy population. A recent discovery of much interest is that made in a Hubble Space Telescope image of a quasar. Dressler (1993) reports the discovery of numerous small faint objects grouped around the quasar. The objects are blue in colour and are of smaller angular size than would be expected for galaxies. Although redshift information is needed before a clear picture can be painted, Dressler speculates that these small blue objects are galaxies in their birth throes.

An alternative to using the diagnostic of star formation is to focus on the gaseous component of young galaxies. Many high redshift gaseous systems have been discovered

by virtue of their absorption of light from higher redshift quasars. These gaseous systems have neutral hydrogen surface densities ranging over at least eight orders of magnitude, up to a density comparable to that of present epoch spirals. They are grouped into one of three types, the names of which are derived from the appearance of the absorption features.

1. Damped Lyα systems. These have HI column densities above $\sim 10^{20}$ atoms cm^{-2}, high enough to produce a very distinctive absorption trough at the Lyα resonance. Such surface densities are comparable to that of the interstellar gas in present epoch spiral galaxies, and the amount of neutral hydrogen mass in these systems is comparable to that seen in baryonic matter in the bright parts of galaxies. Absorption lines from heavy elements are present, indicating the existence of earlier generations of stars. The rate of intersection of clouds along the line of sight is comparable to what would be expected if the clouds had the size and comoving number density characteristic of present day galaxies (Wolfe 1986).

2. Ly limit clouds. These are more abundant than the damped Lyα systems, but have lower surface densities ($\sim 3 \times 10^{17}$ atoms cm^{-2}). Their surface density is high enough to block radiation near the photoionisation edge at the limit of the Ly resonance lines.

3. Lyα forest clouds. These have lower HI column densities still, $\sim 3 \times 10^{14}$ atoms cm^{-2}, producing a forest of narrow absorption lines on the short wavelength side of the Lyα emission of the quasar. The mass of atomic hydrogen in the clouds is small, but the clouds contain a large ionised mass fraction. Surprisingly the space distribution of the clouds at a given epoch is very uniform (Sargent et al. 1980), in contrast to the clustering seen in the present day galaxy population. Could this mean that the galaxy distribution at $z \sim 3$ is smooth? A more likely explanation is that the clouds are fragile and can only exist in voids. Their comoving number density shows a marked evolution with redshift: the clouds would seem to be dissipating. This could be because could be because the clouds are in pressure equilibrium with a hotter, less dense intercloud plasma (Sargent et al. 1980) or it could be that the clouds are gravitationally or inertially confined (Rees 1986).

Of these gaseous systems the damped Lyα clouds are the most promising as progenitors of

today's galaxy population. Damped Lyα systems have HI column densities comparable with that of local spiral galaxies and contain about the right amount of baryonic mass. They have a rate of intersection along the line of sight is comparable to that expected for a population having the size and number density of present day galaxies and the heavy elements in these systems show that they contain (or did contain) stars. The heavy element presence means however that they must have significant ages, and do not represent a population of objects forming their first generation of stars.

2.3.5 Quasars and the IGM at High Redshift

Although the statistics are poor at high redshift, it is believed that the comoving number density of quasars shows a peak at $z \sim 2 \pm 1$ (Hartwick & Schade 1990). Is this telling us something about the epoch of galaxy formation? We do know from the metallicity of quasars that at least some small-scale structure must have been formed at high redshifts, because the high metallicities suggest significant ages even at redshifts of $z \sim 3$ (Schneider, Schmidt & Gunn 1989). The fundamental question is whether or not the quasars trace the galaxy population.

Quasar spectra provide a valuable probe of the intergalactic medium at high redshift (for example the discovery of the Ly gas clouds) and have provided substantial evidence indicating the presence of some form of UV ionising radiation flux at high z. Perhaps this UV flux is from star bursts in young galaxies $3 \geq z \geq 5$? There are two main sources of evidence:

1. The Gunn Peterson effect. Even the most distant quasars show an absence of any significant continuous Lyα absorption from the IGM, indicating a paucity of neutral hydrogen at high redshifts due either to low abundances or to a high state of ionisation (Miralda-Escudé & Ostriker 1990). Photoionisation by quasars is an obvious ionising source, however the known population of quasars is incapable of providing sufficient flux. Perhaps there is an additional population of unseen quasars hidden by dust, or maybe the high state of UV ionisation is from a population of star forming primeval galaxies. Another possibility is shock heating of the IGM by supernova outbursts in galaxies.

2. The proximity effect. Away from quasars, the redshift distribution of absorption

lines in the Lyα forest along different lines of sight is consistent with a universal population of gaseous clouds, the density of clouds increasing with increasing redshift. However when the redshift of the quasar is approached, the density has been found to decrease (Weyman et al. 1981, Murdoch et al. 1986). The interpretation is that the quasars ionise neutral hydrogen in the clouds. This leads to a lower bound on the ionising flux. This lower bound is higher than can be provided by the observed quasar population. An additional UV source is required.

2.3.6 A Summary of Evidence Regarding the Epoch of Galaxy Formation

In summary, empirical evidence is mounting in favour of spheroids forming early ($z > 3$) and the disks later. True *primeval* galaxies are likely to be spheroids. A high redshift of spheroid formation is in accord with present epoch galaxy colours and, more significantly, with results from K selected studies of colour evolution of early type galaxies in clusters; evidence of substantial recent evolution of optically selected cluster galaxies — the Butcher-Oemler effect — should be interpreted as an effect peculiar to the cluster environment. The Gunn-Peterson and proximity effects indicate that young galaxies may well be an important source of ionising radiation at $3 \geq z \geq 5$. Field galaxies show evidence of some form of evolution in the galaxy population below $z = 1$, though it is not clear whether this evolution is representative of the underlying galaxy population or the revelation of a new population of dwarf galaxies. Although several objects at both high and low redshift have been proposed as young galaxies, the data suggest that rather than representing the progenitors of present day galaxies, many of these objects are atypical of the underlying galaxy population.

This empirical evidence favouring a high redshift of spheroid formation is in contradiction with cosmological models, such as CDM, which predict the late formation of galaxies (Section 2.1.2). The discovery of an indisputably young galaxy population at high redshift would strongly challenge these cosmological models.

2.4 The Quest for Primeval Galaxies

2.4.1 Previous Searches

The search for a primeval galaxy population began as far back as the 1970's (Partridge 1974). With the motivation of CDM models predicting late formation of structure on galactic scales, searches have concentrated on looking for emission lines from young galaxies at redshifts of $z \leq 5$. Various techniques have been employed, principally broadband imaging (e.g. Koo et al. 1986), narrowband imaging (e.g. Thompson et al. 1993), long slit spectroscopy (e.g. Lowenthal et al. 1990), and slitless spectroscopy (e.g. Koo & Kron 1980).

The merit of each technique can be assessed from its location in a three dimensional parameter space such as that shown in Figure 2.3. The axes are redshift coverage, depth (i.e. limiting magnitude), and areal coverage on the sky. The depth-area plane of the parameter space reflects the evolution of the galaxy luminosity function, and is also sensitive to the cosmology. The area-redshift plane primarily reflects the cosmology, and the redshift-depth plane the star formation history of the Universe. Increases along the depth axis are proportional to $t^{1/2}$ where t is the integration time at the telescope, increases along the redshift coverage and areal coverage axes are linear with t. Each technique sweeps out some volume in the parameter space, and these volumes can be compared to give a rough estimate of their relative powers. The relative positions for spectroscopy, narrowband and broadband imaging are indicated schematically on the figure. For example, slitless spectroscopy will cover a large area with good redshift coverage (one is not going to find a PG if the galaxies are not in their luminous phase at that redshift, so searching a reduced redshift range cuts down the chance of a detection) but cannot reach very faint limiting fluxes. Narrowband searches on the other hand in general go deeper and have good areal coverage, though the redshift coverage is much reduced. Long slit spectroscopy can go deepest of all but will cover only a small area of sky for each slit position. Obviously the best technique will depend on the expected properties of the primeval galaxies. This will be discussed in more detail in Chapter 3.

Comprehensive reviews of the observational status of this field are given by Koo (1986) and Djorgovski & Thompson (1992). A summary is given in Table 2.2. Most searches have been looking for the strong Lyα recombination line, shifted into the optical

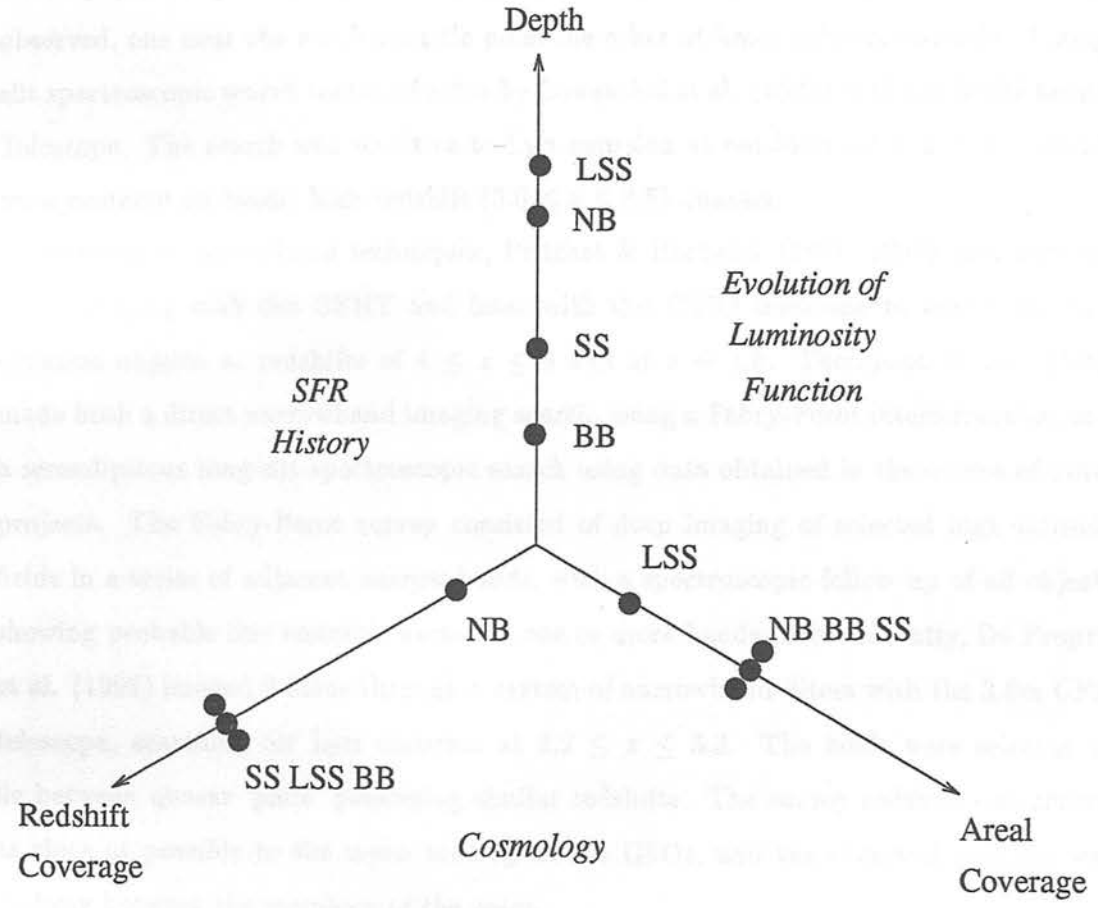

Figure 2.3: A schematic representation of the parameter space for an emission line search for a primeval galaxy. The relative coverage of different observing techniques is indicated. The power of a survey will be proportional to the volume spanned in the parameter space. Abbreviations are: BB — broadband imaging, NB: narrowband imaging, SS — slitless spectroscopy, LSS — long slit spectroscopy.

window. Some have searched random areas of sky and others have searched areas around known high redshift objects, such as quasars, in the hope that any clustering of structure around these objects will enhance the probability of intercepting a PG.

Let us start with the spectroscopic searches. Koo & Kron (1980) employed prime-focus slitless spectroscopy with CCD and photographic detectors on the KPNO 4m telescope, looking for evidence for emission lines or continuum breaks. Two fields were observed, one near the north galactic pole, the other at lower galactic latitude. A long-slit spectroscopic search was conducted by Lowenthal et al. (1990) with the Multi Mirror Telescope. The search was sensitive to Lyα emission at redshifts $2.7 \leq z \leq 4.7$. Fields were centered on bright high redshift ($3.0 \leq z \leq 3.5$) quasars.

Moving to narrowband techniques, Pritchet & Hartwick (1987, 1990) used narrow-band imaging with the CFHT and later with the CTIO telescope to search for Lyα emission objects at redshifts of $4 \leq z \leq 6$ and at $z \sim 1.9$. Thompson et al. (1993) made both a direct narrowband imaging search, using a Fabry-Perot interferometer, and a serendipitous long-slit spectroscopic search using data obtained in the course of other projects. The Fabry-Perot survey consisted of deep imaging of selected high latitude fields in a series of adjacent narrow bands, with a spectroscopic follow up of all objects showing probable line emission excess in one or more bands. Most recently, De Propris et al. (1993) imaged 9 fields through a system of narrowband filters with the 3.6m CFH telescope, searching for Lyα emission at $2.2 \leq z \leq 3.3$. The fields were selected to lie between quasar 'pairs' possessing similar redshifts. The survey redshift was chosen as close as possible to the mean redshift of the QSOs, and the observed position was midway between the members of the pairs.

None of the searches has provided any strong candidates. Their limits on the Lyα luminosity of PGs range from 10^{35} to 10^{37} W, or a total SFR of 1-100 $M_\odot$/yr ($1\sigma/\Box''$). This compares to the SFR in normal disk galaxies of 0-20 $M_\odot$/yr (Kennicutt 1983) and to the predicted Lyα luminosity in PGs of 10^{35} - 10^{38} W. Normal galaxies in the process of formation, if they existed in a relatively unobscured state at redshifts of $z \leq 5$, should have been found by the optical searches.

The lack of success of these searches at $z \leq 5$ has prompted searches for primeval galaxies at higher redshifts. As discussed in Section 2.3, there is substantial observational evidence to justify searches at such high redshifts. At $z \geq 7$ the Lyman break is

Table 2.2: A Summary of Primeval galaxy searches. Limits are for 1σ, $1\square''$, unless otherwise stated. Abbreviations are: NB — narrowband, BB — broadband, Slit. Sp. — slitless spectroscopy, LS Spectr. — long slit spectroscopy, F-P — Fabry-Perot, cont. — continuum, Koo's rev. — limits taken from Koo's review.

Authors	Method	Area arcmin^2	Limiting Flux erg/sec/cm^2	Redshift Coverage	Comments
Partridge (1974)	Imaging B,V,R	360	R=21.7		Large, red PGs. Koo's rev.
Davis & Wilkinson (1974)	Photometry	6	R=21-24		Large, red PGs. Koo's rev.
Koo Kron & Cudworth (1986)	Photometry Astrometry U,B,V,I	2000	B=23		Compact, blue PGs. Koo's rev.
Koo (1981)	Photometry U,B,V,I	1500	B=23.5		Compact, blue PGs. Koo's rev.
Collins & Joseph (1988)	BB Imaging J,K	0.4	J$\geq 33\mu Jy$	8-10.5	High z cont. 2σ limit
Koo & Kron (1980)	Slitl. Sp. I plates	4000	$2\text{x}10^{-15}$ R=20.6	4-6.4	Lyα Ly cont. 1σ assumed
Koo & Kron (1980)	Slitl. Sp. R-I CCD	200	$7\text{x}10^{-16}$ R=22.5	4-6.4	Ly α Ly Cont. 1σ assumed
Pritchet & Hartwick (1990)	NB Imaging	360	2.7×10^{-17}	1.84-1.92	Lyα
Cowie (1988)	NB Imaging LS Spectr.	32 32 0.6	3×10^{-17} 3×10^{-17} 1×10^{-17}	3.75-3.80 4.74-4.79 3.5-5.0	Lyα 1σ assumed
Lowenthal et al. (1990)	LS Spectr. centered on QSOs	0.3	$\sim 2 \times 10^{-17}$	2.2-4.7	Lyα
Thompson et al.(1993)	NB Imaging F-P	280 (1.4)	5×10^{-17} (6×10^{-18})	4.42-4.61 4.74-4.90	Lyα
Djorgovski & Thompson (1992)	LS Spectr.	3.5	$\sim 6 \times 10^{-18}$	2.3-5.6	Lyα Extent assumed.
De Propris et al. (1993)	NB Imaging between QSO pairs	86.4 57.6 57.6 23.8 23.8 24.8	2.5×10^{-16} 2.2×10^{-16} 1.3×10^{-16} 2.5×10^{-17} 2.0×10^{-17} 2.0×10^{-17}	2.17-2.25 2.25-2.33 2.33-2.41 2.58-2.66 2.83-2.91 3.23-3.31	Lyα
Pritchet & Hartwick (1987)	NB Imaging	7	R$\geq$ 26.8 R$\geq$ 27.5 I$\geq$ 26.7 I$\geq$ 26.4	4.19 4.60 6.17 5.67	Lyα Flux in mags $\Delta z \approx 0.09$

shifted into the near-infrared, where the first searches have now been made (e.g. Collins & Joseph 1988, Glazebrook 1991). So far all near-infrared searches have employed broad-band imaging techniques. Collins & Joseph (1988) undertook a deep broadband J and K (1.2 and 2.2 μ m) search using an 8" aperture at UKIRT. The one object discovered had infrared colours indicating that it is a faint foreground galaxy.

As well as searching for individual sources it is also possible to try to detect the collective effects of a young galaxy population, by either the diffuse background generated by energy release from the young galaxies, or by their imprint in the spectra and angular distributions of the x-ray and thermal cosmic radiation backgrounds. PGs may have generated a diffuse background of the order of 1% of the cosmic microwave background (see Djorgovski 1992); observations do not yet constrain such a background, which must be distinguished from local background sources such as atmospheric emission, zodiacal light (sunlight scattered by interplanetary dust), integrated Galactic starlight and light from dusty starburst galaxies. Stronger constraints are eagerly awaited.

2.5 Summary and Implications

The discovery of a population of galaxies at their very youngest age, before environment and the progression of time have modified their appearance, would be a strong tool in the understanding of the physics of galaxy formation and would have profound implications for the field of cosmology. Such a population of galaxies are described as primeval galaxies, and although individual objects have been found with certain characteristics of young galaxies, no indisputably young PG population has been detected. This has led to systematic searches for PGs, primarily based on the Lyα emission line which, provided there is little dust should be substantially stronger than the continuum flux. The searches have mainly been in the optical, covering Lyα emission from redshifts in the range $2 \leq z \leq 6$. No PGs have been found despite reaching what should have been adequate depth and covering adequate areas of sky. Combined with strong empirical evidence in favour of spheroids forming at redshifts of greater than 2, the null results of the optical searches lead us to search for PGs at redshifts of $z \geq 6$. The discovery of a high redshift PG population would strongly challenge current CDM models for the formation of galaxies. No search specifically designed to look for the Lyα emission line

has yet been made at such redshifts. This is the motivation of our high redshift search.

Chapter 3

The IRCAM Search

In Chapter 2 it was concluded that the way to progress in the quest for Primeval Galaxies is to search for the characteristic Lyα line at redshifts of $z > 6$. This conclusion came from two considerations:

1. The failure of emission line searches to detect a PG suggests that we should be looking for these objects at either lower ($z < 2$) or higher ($z > 6$) redshifts.

2. Observational evidence, particularly from studies of colour evolution in early type galaxies in clusters (Aragón-Salamanca et al., 1993.) suggests a high redshift ($z > 2$) of galaxy formation.

In this Chapter I will discuss how we designed and constructed just such a high redshift search. Our method was to employ narrowband imaging techniques in the near-infrared J window using the infrared camera IRCAM on UKIRT. This search is the first designed specifically to look for emission lines from primeval galaxies at these high redshifts. I will justify the design of the search, describe the method of the observations and data reduction, and present the results of the search.

3.1 Design Considerations

When devising a PG search the choice of techniques is large (see the review given in Chapter 2). The techniques can be classified into three main categories: broadband imaging, narrowband imaging and spectroscopy. To appreciate the relative advantages of each of these methods we must consider the factors that determine the likelihood of a PG detection. These factors are four-fold:

1. Depth. The search must be sufficiently sensitive in flux that the light from the PG will be detectable above the background noise of the sky.

2. Area. The search must cover an area large enough that at least one PG will lie in the searched area.

3. Redshift Coverage. The relevant redshift space must be searched — if galaxies first form at redshifts of say $z = 10$ and remain in their luminous young phase only until a redshift of say $z = 9$, then we may well be unable to detect them at redshifts of $z = 3$.

4. Means of identification. There must be a means by which to identify the PGs, i.e. to distinguish them (photometrically, spectroscopically or morphologically) from stars and from the local population of galaxies.

Careful consideration of these factors enabled us to design our search to optimize the chance of detection of a primeval galaxy.

3.1.1 Flux Sensitivity

In Chapter 2 I introduced the generic spectral energy distribution predicted for primeval galaxies: flat continua with very strong recombination lines of hydrogen, particularly that of Lyα at 1215Å. The Lyα line is predicted to exhibit ≥ 20 times the continuum flux (Koo 1986) and therefore can provide a powerful tool in the detection of PGs. The Lyα line can be detectable even when the continuum is below the limiting flux sensitivity. In order to maximize the contrast of line emission over the sky background (sky noise is the limiting factor in deep searches) high spectral resolution is required, and can be achieved either by means of spectroscopy or by narrowband imaging. For a given integration

time, emission line searches with high spectral resolution will reach fainter absolute flux limits than can be reached in searches employing broadband imaging techniques. For this reason, all the more recent PG searches have used slitless spectroscopy, slit spectroscopy, or narrowband imaging (Chapter 2). For the greatest flux sensitivity the spectral resolution should be just less than the Lyα line width of the PG, predicted by Koo (1986) to be $\leq 50\AA$ (the redshifted Doppler width for a velocity dispersion of 600 kms^{-1} at $z = 9$).

3.1.2 Areal Coverage

It is possible to estimate the expected number density of PGs at high redshifts by a simple extrapolation of the local (i.e. present day) number density of galaxies. This can then be compared to the coverage of modern infrared detectors to ascertain the number of fields required for a given detector. For a comoving number density of galaxies η then the number of galaxies per steradian at any redshift z in comoving volume element dV is

$$dN = dV\eta\,. \tag{3.1}$$

Assuming that there is no evolution in the value of η with time, i.e. assuming no density evolution, then the local number density of galaxies, η_o, can be taken as a good estimate of η.

Schechter (1976) showed that the luminosity function of galaxies may be well fitted by the analytic formula

$$\Phi(L)dL = \Phi^*(\frac{L}{L^*})^\alpha e^{-L/L^*} d(\frac{L}{L^*})\,, \tag{3.2}$$

where $\Phi(L)dL$ is the comoving number density of galaxies with luminosity between L and L+dL. The Schechter luminosity function is determined by three parameters: the normalisation Φ^*, the characteristic luminosity L^* (or corresponding characteristic magnitude M^*) at which the luminosity function shows a rapid change in slope, and the faint end slope of the luminosity function, α. Loveday et al. (1992) determine the field luminosity function from the Stromlo – APM redshift survey. After correction for Malmquist bias they find the luminosity function to be well fitted by the Schechter form with parameters $\Phi^* = (1.40 \pm 0.17) \times 10^{-2} h_{100}^3 \mathrm{Mpc}^{-3}$, $\mathrm{M}^*_{bj} = -19.50 \pm 0.13$, $\alpha = -0.97 \pm 0.15$. Efstathiou et al. (1988) apply maximum-likelihood estimators to

five magnitude limited redshift surveys and find $\Phi^* = (1.56 \pm 0.34) \times 10^{-2} h_{100}^3 \mathrm{Mpc}^{-3}$, $M^*_{B_T} = -19.68 \pm 0.10$, $\alpha = -1.07 \pm 0.05$.

The expected number density of objects with luminosity exceeding some limit L_{limit} is then

$$\eta(L > L_{limit}) = \int_{L_{limit}}^{\infty} \Phi(L) dL = \Phi^* \Gamma(\alpha + 1, L_{limit}/L^*) , \tag{3.3}$$

where Γ is the incomplete gamma function. Substituting $\Phi^* = 1.5 \times 10^{-2} h^3$ Mpc^{-3}, and taking $\Gamma(\alpha + 1, L/L^*) = 1$ gives $\eta(L > L_{limit}) = 1.5 \times 10^{-2} h_{100}^3$ Mpc^{-3}. The assumption $\Gamma = 1.0$ can be satisfied by $\alpha = -1.1$, $L_{Limit} \approx 0.3 L^*$, i.e. if we are able to detect the progenitors of all galaxies whose present day counterparts are brighter than $\sim 1/3\ L^*$. This gives a first estimate of the number density to expect for PGs. A more detailed calculation is possible which is dependent upon the assumed Lyα luminosity of the PGs, this calculation is given in Chapter 5.

Substituting $\eta_0 = 1.5 \times 10^{-2} h_{100}^3$ Mpc^{-3} into Equation 3.1 and using the relation for the volume element given in Chapter 5, the prediction is for approximately 2 galaxies per $\square'$ per unit redshift for the redshift range $7 \leq z \leq 9$ ($\Omega = 1$, independent of H_0), comparing favorably to the field of view of the infrared camera IRCAM on UKIRT of $1.4\square'$. These calculations are per unit redshift: the actual number of galaxies predicted for any search at these redshifts must be multiplied by a factor dz, the redshift range covered by the search. Because of this compromise between filter width and finite sampled volume, many PG searches use narrowband filters of widths $\sim 200\mathring{A}$ even though on depth considerations alone a filter width of $\leq 50\mathring{A}$ would be preferred. For a filter width of $200\mathring{A}$ (typical of narrowband searches) $dz \approx 0.2$ and so at we would expect 0.4 PG per $\square'$. To reach a 95% confidence limit of at least 1 object in the search, an area of approximately $7\square'$, or 5 IRCAM fields, must therefore be covered. If an additional n filters are used, discretely sampling redshift space over some redshift range, the volume coverage will have been increased by the factor n. If three filters are used say, only 2 IRCAM fields will be necessary.

Turning to the alternative of spectroscopy, the cooled grating spectrometer CGS4 recently installed on UKIRT has significantly more spectral coverage ($0.2 - 0.4\mu$m dependent upon the grating order) than the narrowband filters, allowing coverage of the entire redshift range $7 \leq z \leq 9$. A 3σ confidence limit can therefore be obtained from a coverage of $1.5\square'$, but the instrument itself has a much lower areal coverage, only

$0.08\square'$, and therefore ~ 20 CGS4 fields would be required. To achieve a 3σ detection of the brightest predictions for the Lyα line (10^{38}W) this would require 80 hours integration time, assuming a line width of 50$\AA$ and a CGS4 sensitivity of $7.5 \times 10^{-16}\mathrm{Wm}^{-2}\mu\mathrm{m}^{-1}$, as determined in Chapter 5. By comparison, to reach the sensitivity of a 3σ detection by narrowband imaging in five IRCAM fields would require only 18 hours integration time (see Section 3.2.4). When this project was devised, CGS4 was not yet on line, the available spectrometer CGS2 had an aperture diameter of only 5".

3.1.3 Redshift Coverage

If galaxies formed at very high redshifts, say $z = 10$, then we cannot hope to detect primeval galaxies at say $z = 2$. Figure 3.1 illustrates the redshift coverage of the searches reviewed in Chapter 2. Redshift is plotted against limiting source frame luminosity. Each search excludes, at the 1σ level, the existence of a population of PGs brighter than the marked luminosity within the indicated redshift range. The right-hand y-axis of the plot shows the equivalent star formation rate for a given luminosity in Lyα. The conversion was obtained as Kennicutt (1983) — a star formation rate of 1 $M_\odot$ per year corresponds to $\approx 10^{35}$W in Lyα (see Chapter 5). Also marked is the upper end of the star formation rate as observed in local spirals (Kennicutt 1983). It can be seen that the majority of the searches are sensitive to star formation rates considerably less than those observed in spirals, and since even greater star formation rates are predicted for PGs (10-1000 $M_\odot$/yr), all but the broadband search of Koo & Kron (1988) are easily reaching fluxes sufficiently faint to be probing a realistic PG population. Over the entire redshift range $2 \leq z \leq 6$ there is then at least one search sensitive to the existence of a PG population.

As well as reaching faint enough fluxes, the PG searches also survey enough area. This is best illustrated by Figure 3.2, which shows the limits that the searches place on the rest frame volume density of any Lyα emitters. Each limit excludes the area to the upper left. All of the limits on the volume density are well below the value of the local number density of bright galaxies. This is a reasonable estimate of the expected volume density of PGs (see Section 3.1.2), and so it can be inferred that normal galaxies in the process of formation, if they existed in a relatively unobscured state at redshifts of $2 \leq z \leq 6$, should have been found. Hence the conclusion of Chapter 2 to search at higher redshifts. At these redshifts the Lyα line (1215$\AA$) is shifted longward of optical passbands. Our

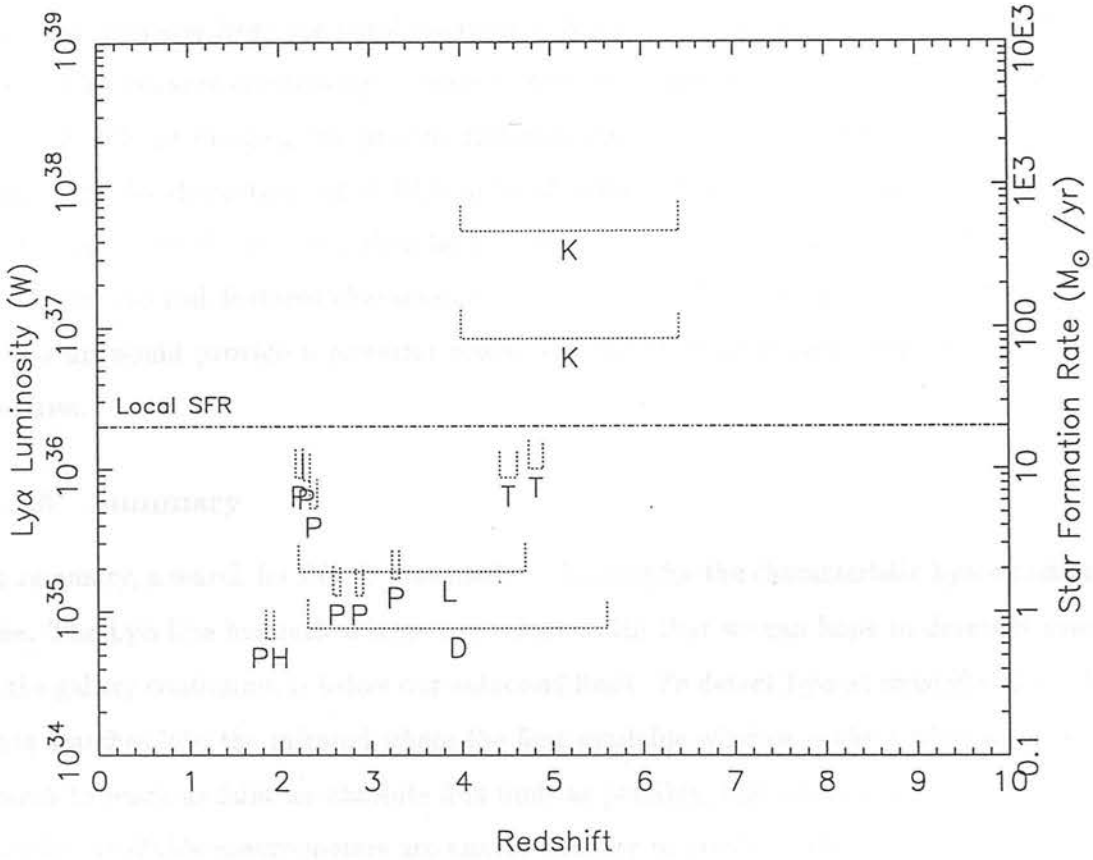

Figure 3.1: Redshift coverage of primeval galaxy searches, for Lyα emission. Luminosity limits are 1σ, and are normalised to 1 " diameters; for 2" diameters the luminosity limits shift upwards by a factor of 2. Limits are as follows; K: Koo & Kron (1980), PH: Pritchet & Hartwick (1990), L: Lowenthal et al. (1990), T: Thompson et al. (1993), D: Djorgovski & Thompson (1992), P: De Propris et al. (1993). The extended dotted line (Kennicutt 1983) represents the high end of SFR of normal disk galaxies. Ω=1.0, H_0=50 kms^{-1}Mpc^{-1}.

high redshift search was therefore conducted at the next available atmospheric window, the infrared J window, at $\sim 1 - 1.5\mu$m.

3.1.4 Identification of Primeval Galaxies

Any search will be of limited use if the PG candidates cannot be readily distinguishable from foreground stars and galaxies. The ultimate means of identification is by spectroscopy, however from the considerations of Section 3.1.2 it is clear that with present technology infrared spectroscopy cannot provide sufficient areal coverage for a PG search.

Narrowband imaging can provide sufficient colour information for emission line objects with the characteristics of PGs to be identified. Followup spectroscopy at optical and infrared wavelengths can then be used to verify the detection of Lyα and to search for other spectral features characteristic of PGs (see Chapter 2). This spectroscopic follow-up would provide a powerful probe into the physical environment of any young galaxies.

3.1.5 Summary

In summary, a search for PGs is best made by looking for the characteristic Lyα emission line. The Lyα line has such a large equivalent width that we can hope to detect it even if the galaxy continuum is below our detection limit. To detect Lyα at redshifts of $z > 6$ puts searches into the infrared where the first available window is the J window. For a search to reach as faint an absolute flux limit as possible, high spectral resolution is desirable. Available spectrometers are unable however to provide sufficient areal coverage. This can be achieved by narrowband imaging, which can also provide sufficient colour information for emission line objects with the characteristics of primeval galaxies to be identified. Subsequent spectroscopy can then be used to verify their nature.

From all these considerations it was decided to make the search for PGs at $z \geq 6$ by means of narrowband imaging in the J window.

3.2 Instrumentation

The narrowband infrared images for the PG search were made using the 3.8m United Kingdom Infrared Telescope, UKIRT. The telescope is located on the summit of Mauna

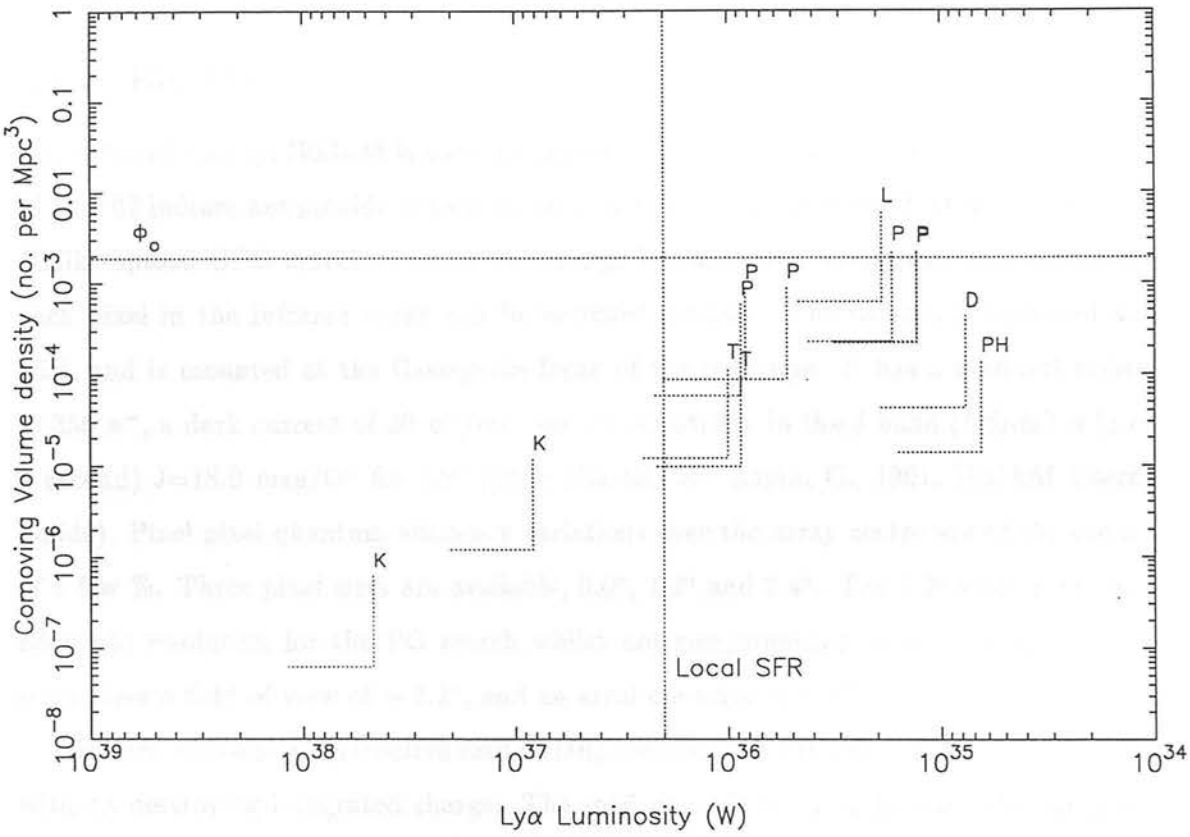

Figure 3.2: Limits on the comoving volume density of primeval galaxies as a function of Lyα luminosity. Abbreviations and limits are as Figure 3.1. The extended vertical dotted line indicates the high end of SFR of normal disk galaxies (Kennicutt 1983), the extended horizontal line the local number density of bright galaxies ($L_{\rm limit} \geq 0.3L^*$). $\Omega_0 = 1, H_0 = 50$ kms^{-1}Mpc^{-1}.

Kea, an extinct shield volcano on the Big Island of Hawaii. The site is at an altitude of 4200m and is one of the best in the world from which to make infrared observations. The volcanic peaks rise very swiftly from the ocean bed, and as a result incoming air streams, rather than rising over the peaks, divide and flow around them. This means that the inversion layer rarely rises above 3500m, making the weather at the summit usually clear and very stable, with very good astronomical seeing — typically 0.5"-1.4". The atmospheric water content at the site is 10-20 times less than at a sea level site, which is very important for infrared astronomy as water vapour contributes much of the atmospheric extinction at infrared wavelengths.

3.2.1 IRCAM

The infrared camera IRCAM is used for imaging in the 1 to 5 μm band. It uses an array of 58×62 indium antimonide detectors, bonded to an array of silicon MOSFET devices. Unlike optical CCD detectors where the charge is transferred along rows and columns, each pixel in the infrared array can be accessed directly. The camera is operated at 35K, and is mounted at the Cassegrain focus of the telescope. It has a read-out noise of 350 e^-, a dark current of 30 e^-/sec, and its sensitivity in the J band (1-5μm) is (1σ 1 second) J=18.9 mag/□" for 1.2" pixels (Casali, M., Aspin, C., 1991, IRCAM Users Guide). Pixel-pixel quantum efficiency variations over the array centre are of the order of a few %. Three pixel sizes are available, 0.6", 1.2" and 2.4". The 1.2" scale provides adequate resolution for the PG search whilst not compromising areal coverage. This scale gives a field of view of $\sim$ 1.2', and an areal coverage of 1.4□'.

IRCAM uses a non-destructive read (NDR) technique — the voltage can be measured without destroying integrated charge. The read out scheme is as follows: the array is reset, read, then after the chosen integration time is read again. The final image is the difference between the two reads. The bias, or pedestal DC offset of the detector, whose purpose is to ensure that signals are positive, is automatically removed. A multiple non-destructive (MNDR) mode became available in 1992. Because each read is non-destructive, the array may be read many times in each integration, without altering the final signal. Each read includes a measurement uncertainty so by taking multiple reads it is possible to significantly reduce the final read noise for each integration. The details of the noise reduction algorithm are described by Chapman et al. (1990), who find that

for n reads of the detector the relation between the effective MNDR read noise σ_{mult} and that for a single read σ_{single} is

$$\sigma_{mult} = \frac{\sigma_{single}}{\sqrt{n/12}} \, . \tag{3.4}$$

The number n of reads that are possible in each integration is limited by the processing speed of the data acquisition system and by the bandwidth of the electronics. The reduction of readnoise now achievable with IRCAM is a factor of ~ 4. Unfortunately however we were unable to make maximum use of MNDR due to software problems encountered on our observing run.

3.2.2 Choice of Wavelengths for the Narrow Band Filters

Sky emission at J is chiefly non thermal radiation from excited vibrational levels of the hydroxyl radical OH^- in the upper atmosphere. Figure 3.3 shows the spectrum of the sky at J at the summit of Mauna Kea (as Figure 1 of Ramsay et al. 1992). It can be seen that the continuum contribution at these wavelengths is low compared to the line emission. The domination of the background flux by emission lines makes the choice of wavelengths of narrowband filters a crucial one as a narrowband filter enclosing the stronger of the OH^- lines, for example the P branch doublets at around 1.3μm, would experience a particularly high sky flux. In addition, the OH^- emission line strengths are known to vary on both long and short timescales (Ramsay et al. 1992). Long term fluctuations are due to diffusion of the minor atmospheric constituents altering the number density of reactants. Shorter period variations, on time scales ranging from just few minutes to an hour, result from density and temperature perturbations (caused by meteorological phenomena or by man-made effects) travelling through the upper atmosphere, causing changes in the reaction rates and column densities of reactants and hence a variation in OH^- emission intensity. This gives us an additional incentive to avoid strong sky lines, as the variability of the sky flux in the filter would limit the accuracy of flat fielding (see Section 3.3.2).

We therefore selected our narrowband filters to lie between strong OH^- lines at 1.02μm, 1.14μm, 1.21μm, and 1.3μm, also avoiding absorption features at 1.12-1.16 μm and 1.32μm-1.44μm. Four filters were used, with central wavelengths at room temperature of 1.01μm (filter U1), 1.075μm (U2), 1.190μm (U3), and 1.260μm (U4), all with

bandwidths of 2% FWHM. At their operating temperature of 77K, the filter passbands shift to shorter wavelengths due to contraction, by ≈1% . The passbands were chosen in 1989, when high spectral resolution infrared sky spectra such as that shown in Figure 3.3 were not available. Instead, the wavelengths were selected by reference to models of the infrared sky emission (McCaucghrean,M., personal communication). It can be seen from Figure 3.3, in which the shaded areas represent the wavelength coverage of our filters at their operating temperature, that filters U2, U3 and U4 do in fact fit between the strongest emission lines. U1, chosen to lie just shortward of the strong OH^- line at 1.01μm, does not appear to be so well placed. Subsequent comparisons between the sky count in the four filters however (Section 3.2.4) showed that the filter U1 has a sky count no higher than that found in the other three filters and must in fact fall just shortward of the line at 1.01μm (the uncertainty is due to a lack of knowledge of the exact passband of the filters at the operating temperature).

At 1μm, a 2% FWHM bandwidth corresponds to a passband of 200$\AA$. This is significantly greater than the predicted line width of the Lyα line ($\sim$ 50$\AA$, Section 3.1.1). At 200$\AA$ the resolution is sufficient to lie between the strongest of the sky lines. Reducing the filter widths below 200$\AA$ would not significantly increase the effective depth of the search, but would reduce the volume of space sampled, and hence reduce the number of PGs intersected by the beam.

3.2.3 Manufacture of the Filters

The filters are commercially available interference filters, supplied by Infrared Engineering Ltd, Essex. The interference filter is a multilayer system based on the Fabry Perot interferometer (Figure 3.4). The device consists of two plane-parallel, partially reflecting surfaces separated by a dielectric cavity with spacing $d = \lambda/2$. The reflecting surfaces of the filters are constructed from alternating high and low refractive index dielectric stacks, each of which are multiples of $\lambda/4$. On entering the system an incident light ray is multiply reflected between the surfaces, at each reflection a small number of photons are transmitted through the second surface. Because the optical arrangement of the system is such that the beams produced by multiple reflections are in phase with the transmitted beam only at the desired wavelength λ, such beams will interfere constructively. Reflected beams at other wavelengths will be out of phase and hence will interfere

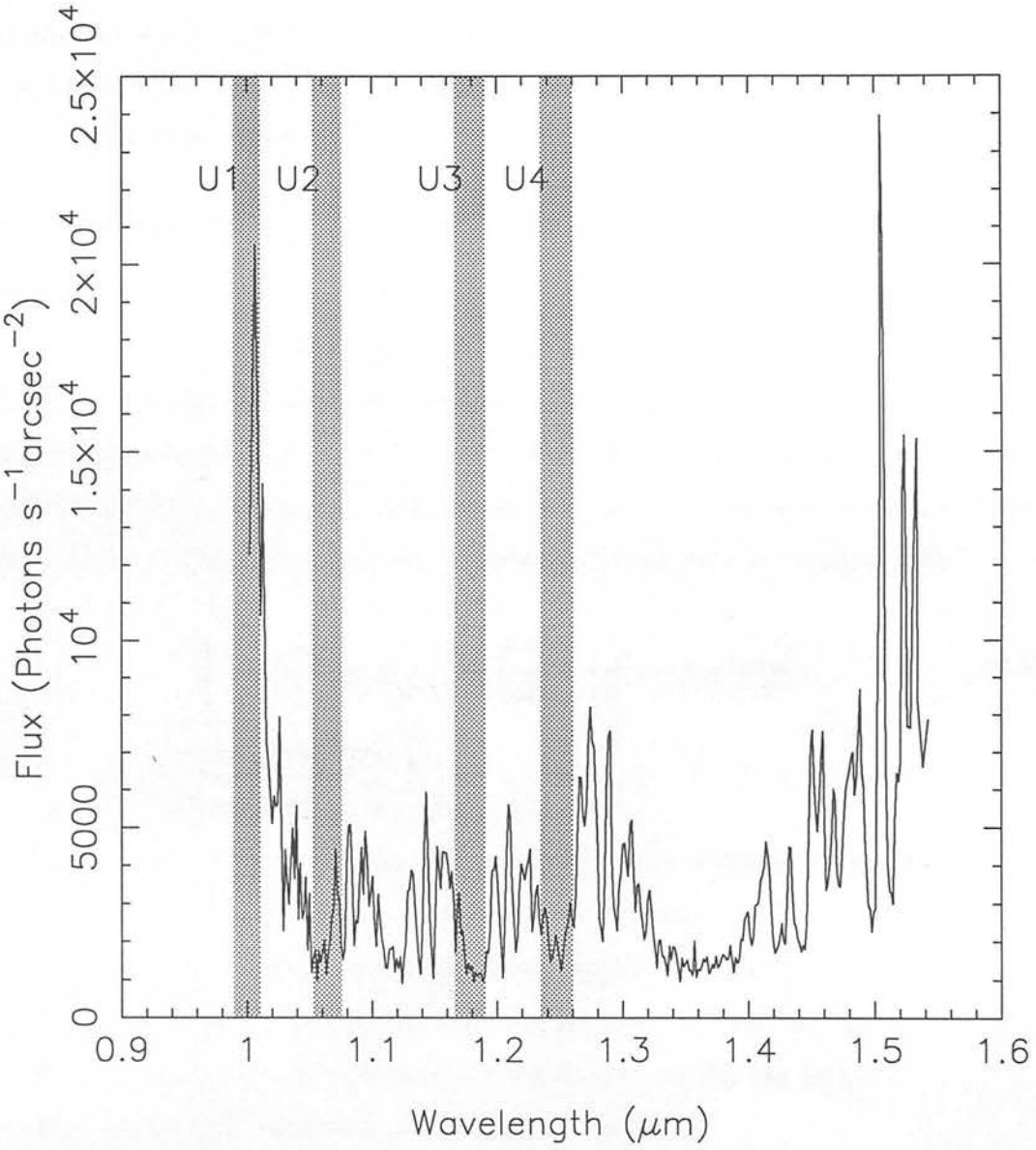

Figure 3.3: Spectrum of the OH^- emission lines in the J window (Ramsay et al. 1992). Shaded areas represent the wavelength coverage of our narrowband filters, for a 1% cooling shift.

destructively. By choice of reflectivities, number of layers and number of Fabry Perot cavities, the filter can be constructed to give the desired bandwidths and beam shape. Transmission curves for the filters U1-U4 can be found in the Appendix to this thesis.

As well as transmitting at the desired bandpass, interference filters may also transmit unwanted sidebands which must be eliminated by means of a blocking filter. The blocking filter for our project was a Schott WG 320 filter, supplied by Optical Coating Laboratories, Fife. WG 230 provides blocking out to 5.5μ m. Its transmission curve can also be found in the Appendix.

3.2.4 Sensitivities and Integration Times

The signal recorded by a detector is measured with a certain amount of uncertainty. This arises from many sources: for example the uncertainty in the counting of the photons (for n photons the uncertainty is $\sim \sqrt{n}$, assuming Poisson statistics), fluctuations in the sky background, fluctuations in the dark current of the detector, and the contribution from the read noise of the detector. The signal-to-noise ratio for a photon counting detector in the presence of sky background, dark current and read noise is (Longair 1981)

$$\frac{S}{N} = \frac{A_{\rm eff} N(\nu) \Delta\nu t}{\sqrt{A_{\rm eff} N(\nu) \Delta\nu t + \Omega A_{\rm eff} B(\nu) \Delta\nu t + D\,t + R^2}} , \qquad (3.5)$$

where t is the integration time (s),

$\Delta\nu$ is the bandwidth of the filter (Hz),

$A_{\rm eff}$ is the effective aperture of the telescope (m^2), which is the geometric collecting area multiplied by the efficiency of the system,

$N(\nu)$ is the flux density of the source (photons $m^{-2}s^{-1}Hz^{-1}$),

$B(\nu)$ is the sky background intensity (photons $m^{-2}s^{-1}$ $Hz^{-1}sr^{-1}$),

Ω is the solid angle subtended by the detector on the sky (sr),

D is the dark current in the detector (e^- sec^{-1}),

R is the readout noise (e^-).

The sky background is so high at infrared wavelengths (at the summit of Mauna Kea the sky brightness in the J band is $\sim$ 14.5 mags/$\Box''$, compare this to a typical optical sky brightness of $\sim$ 22.5 mags/$\Box''$ in B) that the contribution from the dark current can

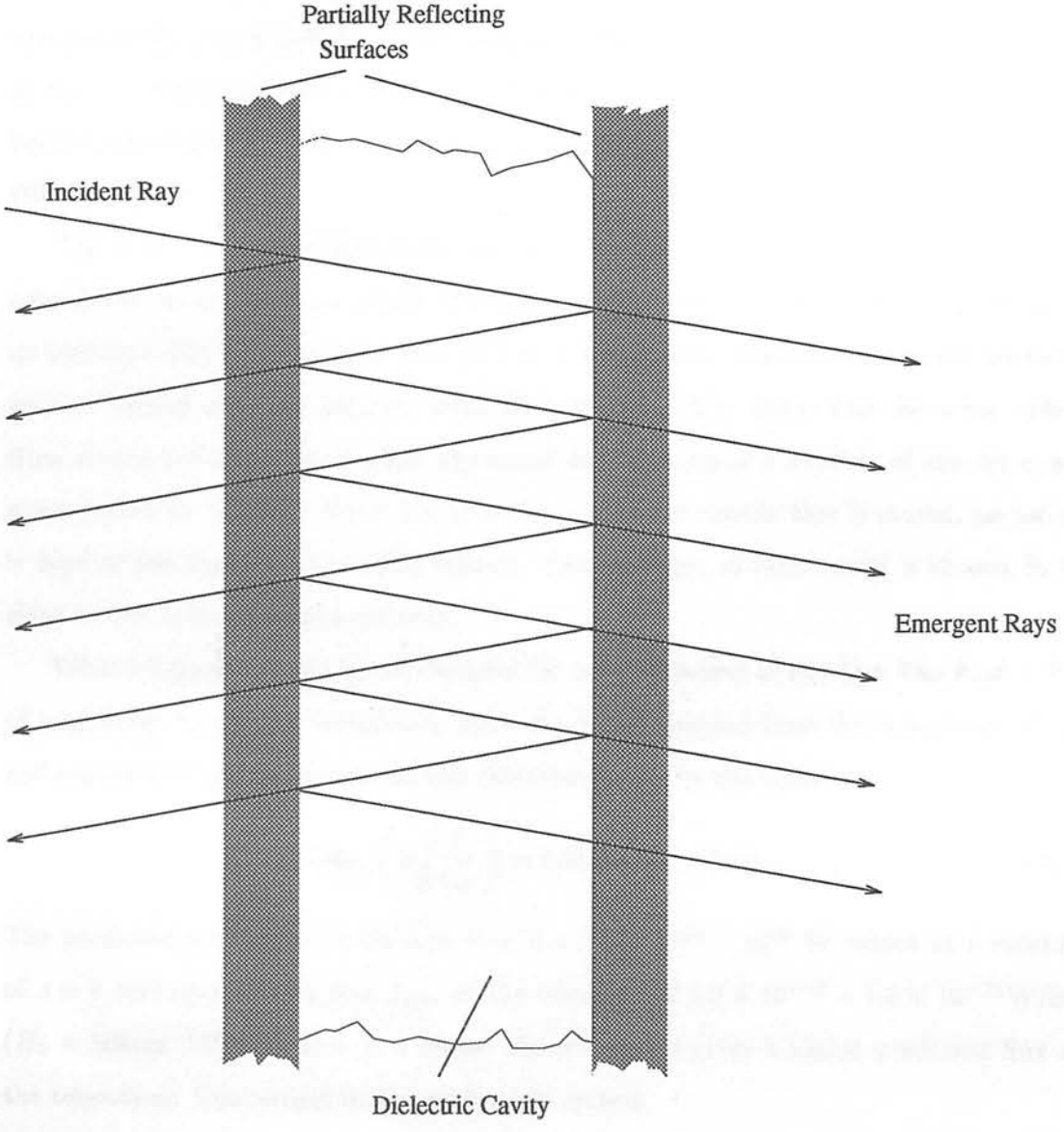

Figure 3.4: The Fabry Perot Etalon.

be neglected. In addition, for observations that are sky background limited then the read noise is negligible compared to the sky noise. For faint signals therefore the term $\Omega A_{\rm eff} B(\nu) d\nu t$ dominates and

$$\frac{S}{N} = \sqrt{\frac{A_{\rm eff} N^2(\nu) \Delta\nu t}{\Omega B(\nu)}} \,. \tag{3.6}$$

The limiting magnitude at which faint objects can be detected is therefore determined by the Poisson shot noise in the sky background. This relation can be used to calculate the sensitivity of a detector, i.e. the magnitude that an object must have to be detected at the 1σ level in 1 second ($S/N = 1$). The sensitivity of IRCAM at J for background limited exposures and 1.2" pixels is $J_{1\sigma 1s}$=18.9mag/□" (Casali, M., Aspin, A., 1991, IRCAM Users Guide).

The length of an exposure is limited by the point at which the array becomes saturated, i.e. at the point at which the detector wells become full. This limitation gives an optimum IRCAM exposure time at J of $\sim$ 40 seconds. Such exposures will be background limited with the detector wells filled to about 2/3; above this the array suffers from strong non linearity. Longer exposures are made up of a number of shorter exposures known as 'coadds'. Note that it is the sum of the coadds that is stored, no record is kept of the signal in individual coadds. The exposure of each coadd is chosen to be close to the optimum exposure time.

What integration time $t_{3\sigma}$ is required for a 3σ detection of the Lyα line from a PG of magnitude $J_{\rm PG}$? The integration time can be determined from the sensitivity of the instrument and the magnitude of the observed object by the relation

$$\log_{10}\left(3\sqrt{\frac{1}{t_{3\sigma}}}\right) = 0.4(J_{1\sigma 1\rm sec} - J_{\rm PG}) \,. \tag{3.7}$$

The predicted luminosity in the Lyα line of a PG is $10^{35} - 10^{38}$ W, which at a redshift of $z = 9$ corresponds to a flux $f_{{\rm Ly}\alpha}$ at the telescope of $1.3 \times 10^{-18} - 1.3 \times 10^{-21}$W/m^2 ($H_0 = 50$kms^{-1}Mpc^{-1}, $\Omega = 1$, a higher H_0 or lower Ω gives a higher predicted flux at the telescope). Converting to the magnitude system

$$J_{\rm PG} = 2.5\log_{10}\left(\frac{f_0}{f_{\rm J}}\right) \,, \tag{3.8}$$

where f_0 is the J flux of a 0th magnitude star. $f_0 = 1.77 \times 10^{-23}$ Wm^{-2} Hz^{-1} over the J filter width of 9.6×10^{13} Hz. Assuming negligible contribution to the J magnitude

from the PG continuum, i.e. $f_J = f_{Ly\alpha}$, Equation 3.8 gives a predicted magnitude J_{PG} of 22.8 at the brightest. Inserting $J_{1\sigma 1s}$=18.9mag/□" into Equation 3.7 then gives an integration time for a 3σ detection of at least 3.3 hours, and substantially longer for low PG luminosity predictions. Note that this calculation is appropriate for an object of $\sim$ 1" in extent: the integration time for an extended object will be increased in proportion to its area. An extended PG would require a longer integration time for a 3σ detection.

Turning now to the narrowband filters, the sky count in the filters U1, U2 and U4 was found to be an order of magnitude less than that in the broadband J filter. The widths of the narrowband filters is approximately 1/15th of the J filter, and so somewhat disappointingly they experience no less sky flux than would be expected from their smaller bandwidths (it was hoped that by selecting the filters to lie between the strongest of the OH^- lines the sky flux could be substantially reduced, the filters must in fact encompass some sky lines). Although this means that for detections of continuum objects there is no gain in sensitivity, the small width of the filters and the fact that the values of sky flux indicate that at least the strongest of the OH^- lines have been successfully avoided means that there will be a gain in sensitivity to emission line objects.

U3 was found to have a sky count of approximately twice that of the other narrowband filters. For this reason, on the first observing run in February 1991 only filters U1, U2 and U4 were used. On the second observing run in March 1992 it was discovered that the filter U4 had degraded to the extent of being unusable. It is likely that this was caused by thermal shock suffered as the camera was raised from liquid nitrogen temperatures to room temperatures. As a result, on the second run we imaged through U3 instead of through U4.

Assuming that the J magnitude limit $J_{1\sigma 1s}$ is determined primarily by sky flux (i.e. the observations are background limited), it is possible to estimate the integration time needed in one of the narrowband filters to achieve a 3σ detection of the Lyα line from a PG. The sky flux in the narrowband filters is an order of magnitude less than in J, and since $t \propto f^2$, the integration times required to detect an emission line will be 100 times or so less through one of the narrowband filters than through the broadband J filter (assuming that the line is unresolved in the narrowband filters). The advantage of using narrowband filters for emission line searches now becomes clear. For the brightest PG models, a detection at the 3σ level would be expected in just 2 minutes compared to the

3 hours required in broadband J. Taking a more likely model (with a bright period of 10^8 years), a 3σ detection in a narrowband filter would be expected in 3.3 hrs. Assuming that 7 hours per night can be spent integrating on field (the remainder of the night being spent on overheads such as moving the telescope and making standard star observations) then this flux level could be reached in each of the four filters in three fields in a total of 6 nights. Again, these predictions are for a compact (1" diameter) PG; an extended object would require a greater integration time.

3.3 Observations and Reduction

IRCAM Observations were made in February 1991 and March 1992, over a total of eight allocated nights. Previous observing runs in May 1989 and February 1990 suffered from bad weather and no data was obtained from these two runs. We imaged in three fields (each of 1.4□') in the four narrowband J filters.

3.3.1 Field Selection

The three fields are of blank pieces of sky, chosen according to the following criteria:

1. The fields are all at high galactic latitude ($b > 30°$), to minimize Galactic extinction and reddening.

2. The fields are equatorial (Dec $\sim 0°$), and hence accessible from both northern and southern hemispheres for followup observations.

3. We required that additional broadband data be available, so that the colours of any candidates can be examined. We selected our fields from areas observed by Glazebrook (1991) as part of his large-area 2μm survey. This provides us with B, V, R, I, and K images of the selected fields.

4. The fields are uncrowded to a depth of R=24 or so, to minimize obstruction by foreground objects, but have at least one reference star for astrometry.

5. There are no bright sources close to the fields. This is to minimize the phenomenon of ghosting. Any misaligned parallel optical surfaces inside the IRCAM cryostat can give rise to in-focus ghosts of bright sources. By the time of our 1992 run the

Table 3.1: Positions of the Reference Objects.

Field	RA_{1950}	DEC_{1950}
PG_1	09:18:05.4	-00:19:24.8
PG_2	13:41:58.5	00:08:05.5
PG_3	09:18:08.1	-00:20:19.3

ghosting problem was resolved in broadband J, H and K by tilting the filters and by installing a meniscus entrance window. Unfortunately it was not possible to tilt our narrowband filters since the resultant wavelength shift would be incompatible with the 1991 run. Therefore, spatially displaced internal reflections at the few per cent level were expected in our narrowband images.

The positions of the reference objects in each of our fields are given in Table 3.1.

3.3.2 Flat Fielding

IRCAM uses a 58 × 62 pixel array. Each pixel of the array responds differently to incoming photons. There are significant variations in detector gain on all scales, ranging from a few % variation on pixel-pixel scales to variations of 5-10% across the chip. The variations are sufficiently large to mask objects in the unprocessed image and to make accurate photometry impossible. It is therefore important that the variations are calibrated out. This can be done by dividing the images by an exposure of a uniformly illuminated background, known as a flat field. Flat fielding is particularly crucial in the infrared because of the high sky background at these wavelengths. For observations to be background limited the systematic error of the observations must be less than the sky noise. The high infrared sky flux means a low fractional sky error ($df/f = \sqrt{n_{\rm photons}}/\ n_{\rm photons}$ from Poisson statistics), and so the accuracy in the flat field must be high in order for the observations to be background limited.

The detector response also varies with wavelength, and so the flat field is wavelength dependent. This means that the source of illumination for the flat field should be as close as possible to the spectral energy distribution of the object to be observed. A PG search is dominated by emission from the night sky, and therefore the ideal flat

field would be constructed from an illumination on the array of a piece of featureless night sky. Such a piece of sky is of course difficult to come by: most fields within any reasonable integration time will reveal the presence of stars and galaxies. There is a technique however that allows an accurate flat field to be created without spending time searching for featureless pieces of night sky. One of the criteria used in the selection of the fields for the PG search was that they be uncrowded. If, rather than integrating at one set position for each field, the telescope is offset to slightly different positions and integrations made in each position, then by median filtering a stack of offset frames any sources are effectually (though not totally, see Section 3.3.6) removed and an image of featureless sky is created. The technique is known as 'on field flat fielding' — the flat field is constructed without spending valuable time integrating on adjacent sky. By means of on field flat fielding techniques, highly accurate flat fields can be created.

Frames were taken in a sequence of nine positions each offset by 5 pixels (6") from the central field position. The offset was chosen to be larger than the extent of any of the on field objects. On a typical night of the order of thirty such sequences of nine frames were made, a laborious task if undertaken manually. Fortunately the IRCAM control software makes it possible for offsets to be made automatically, with much increased efficiency. Offsets can be made either by using the telescope encoders or by using the crosshead whilst autoguiding. Autoguiding gives the better accuracy and was used wherever possible.

The nine frames in each sequence were combined to form the flat field for that sequence. Figure 3.5 illustrates the IRCAM coverage of each mosaic position. The most sensitive area is the central region of 0.96□'. This central region is covered by all nine of the mosaic positions, and hence it is here that the search reaches its greatest depth. In comparison the corners are covered by only one mosaic in each sequence and will be a factor of 3 less sensitive in flux.

The flat field is known to vary substantially on timescales of the order of an hour (Casali, M., Aspin, A., 1991, IRCAM Users Guide), probably because due to fluctuations in OH^- emission the colour of the sky is varying significantly, effecting the flat field through its wavelength sensitivity. Flat fields were therefore created every 15 minutes or so. The flat field was found to vary typically by a few percent over the course of a night.

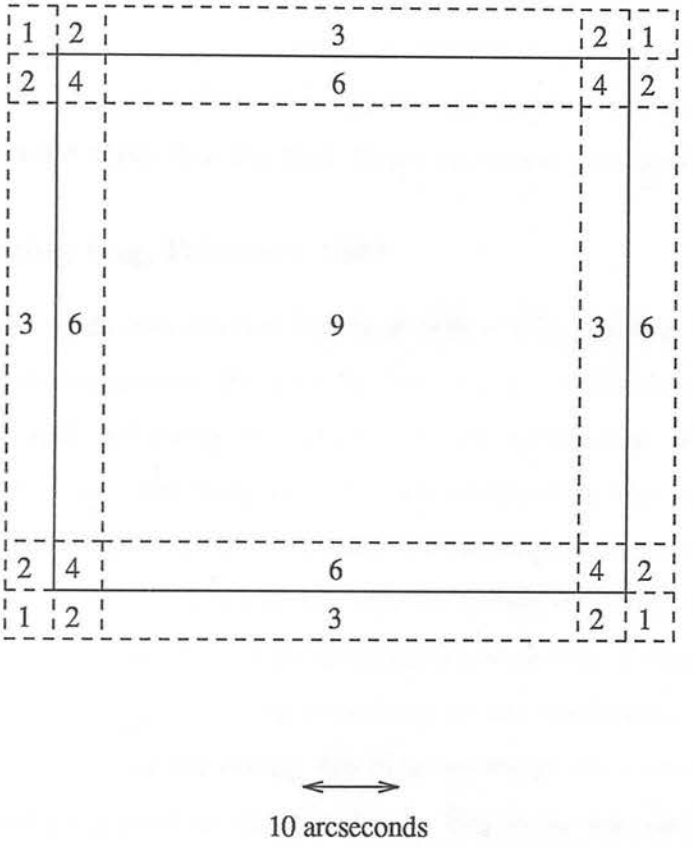

Figure 3.5: The IRCAM coverage of each mosaic position for each field. The numbers indicate how often each region is covered by one of the nine mosaic positions.

3.3.3 Dark Frames

Even if all light is prevented from falling on the array the detector will measure a non zero signal. This is the dark current of the system and it must be subtracted from the observations. Dark frames were made by taking exposures with the incoming light blocked by blank filters in the filter wheel. Because the dark current does not increase linearly with time, the dark exposures were of the same length as the object frame exposures, and because the dark current may drift slightly throughout the night the dark frame subtracted from each object frame was that taken nearest in time to the observation itself. Only a few darks per night were taken in the reduction of the 1991 data, many more were taken in the 1992 run because of the fear of instability in the dark current caused by the glitching of the array. In addition to matching exposure times, in almost all cases the dark was of the same number of coadds as the object frame. If the number of coadds did differ then the dark frame was scaled accordingly.

3.3.4 Observing Log, February 1991

Observations were made over the four nights of 14th – 17th February 1991. Two fields, PG_1 and PG_2 were observed. On the first three nights, conditions were photometric, with humidity $< 10\%$ and seeing of about 1". On the fourth night there was high and intermediate level cloud. The little data that was obtained on this night was found to have a low signal-to-noise ratio (S/N) and was not included in the final reduction of the data. The wind was high throughout the run, on occasion causing the autoguider to suffer 'windbounce': the sampling of the autoguider is such that in high wind conditions oscillations are produced due to over-corrections in the positioning of the telescope, with the effect of increasing the seeing. On these occasions the autoguider was turned off, and the telescope guided by the crosshead. The focus was checked regularly, in addition IRCAM uses an automatic focussing system which refocuses whenever a new filter is selected. The focus through the narrowband filters is slightly different from that through the standard broadband filters, and so a filter offset was determined and entered into the system software. Integration times ($\sim$ 200 seconds) were such that individual integrations were background limited but well clear of the strong non-linearity that occurs near array saturation. A much smaller non-linearity exists at low counts, it is

standard procedure to remove this at the telescope. The number of coadds was as low as possible to allow frequent flat fields, with the proviso of sufficient S/N on the reference objects — 1 coadd was found to be adequate. Darks were taken every few hours. Total integration times in each field were of $2 - 4.5$ hrs in each of U1, U2, and U4, these are recorded in Table 3.2. A0 standards were chosen from the UKIRT list of commonly used standards.

3.3.5 Observing Log, March 1992

On the second run, over the nights of 2nd-5th March 1992, good data was obtained on all four nights. The weather was in general clear, with humidity ranging from $5 - 10\%$ and wind speeds of less than 20 mph. On the second and third nights a little dust was present in the atmosphere. For part of the third night there was also some high level cirrus. Seeing was good, $1'' - 1.5''$.

It was hoped on this run that we would be able to make use of the new multiple non-destructive read (MNDR) mode, which can reduce the readnoise of IRCAM by a factor of four (see Section 3.2.1). In MNDR mode the integrations become background limited in approximately half the integration time of the NDR mode, and individual coadds can therefore be shorter than in the simple NDR mode. We obtained a small number ($< 5\%$) of MNDR mode observations, integrating for 20 seconds with 4-6 coadds depending on the field. The reduced integration time in each coadd means that a greater number of them are needed to get sufficient S/N on the reference objects. However, problems were encountered with the software of the MNDR mode — the system repeatedly crashed, each crash wasting valuable observing time. Because of the massive increase in overheads it was decided to return to the simple NDR mode.

Another problem encountered on this run was the occasional glitching of the array. The cause of this glitching was uncertain: hardware faults, software faults or an unknown terrestrial source of electromagnetic radiation were all possibilities. The effect of the glitch was serious. After each glitch the array was left unstable for over half an hour, during which time no useful data could be obtained. It was feared that the stability of the dark current would be affected by the glitching, and so dark frames were therefore taken as frequently as possible, typically every half hour. The dark current throughout the night of 5th March was typical of the four nights, and is plotted in Figure 3.6. The

Table 3.2: Integration times in each field (February 1991).

Field	Filter	Total Integration Time (hrs:mins)
PG_1	U1	4:30
	U2	4:00
	U4	3:30
PG_2	U1	2:00
	U2	2:00
	U4	2:26

Table 3.3: Integration times in each field (March 1992).

Field	Filter	Total Integration Time (hrs:mins)
PG_1	U1	0:48
PG_2	U1	2:22
	U2	0:50
	U3	2:50
PG_3	U1	3:38
	U2	3:30
	U3	2:42

dark count was estimated by the median of a 20×20 pixel box placed on the dark frame. With the exception of the darks around observations 120, 200 and 270 (marked by open circles), the dark appears to be extremely stable. The anomalous darks were taken just before or just after a glitch was recorded. They were not used in subsequent data reduction. With the anomalous points excluded, the mean dark count over the whole of the night for 1 second, 1 coadd was -0.40 counts with a standard deviation of 0.05 counts. This variation in the dark is substantially less than the pixel-pixel fluctuations in the 20×20 pixel box on individual frames. The deviation from the median enclosing 68% of the values is $\sigma_{pp} \approx 0.8$ counts. From this it is clear that, provided that the glitched data are excluded, the fears of an unstable dark were unfounded.

Approximately two hours per night were lost to glitching. Despite this a substantial amount of useful data were obtained and Table 3.3 gives the total integration times. Integrations were made with filters U1, U2, and U3: U4 had degraded since the last run and had to be discarded.

3.3.6 Data Reduction

Each frame was examined prior to data reduction to check that each was of the type expected from the observing log (i.e. standard star observation, field observation or dark), and that none suffered from spurious signals such as those seen during glitching. Because of the large effect of the flat field it is not possible to pick out objects on the raw, unprocessed frames and so this initial examination was made by subtracting from the frame a frame of similar type but with a positional offset. This removes the dark and to a first approximation accounts for the flat field.

The data were reduced in the standard way: dark frames were subtracted, each frame was then flat fielded, bad pixels were flagged and subsequently ignored. The frames were then registered to remove the positional frame-to-frame offsets and mosaiced to form the final image for each each field in each filter. The reductions were made using the FIGARO (Fast Interactive Graphics and Reduction Operations) system created by K.S. Shortridge. Greater detail of the reduction procedure is given below.

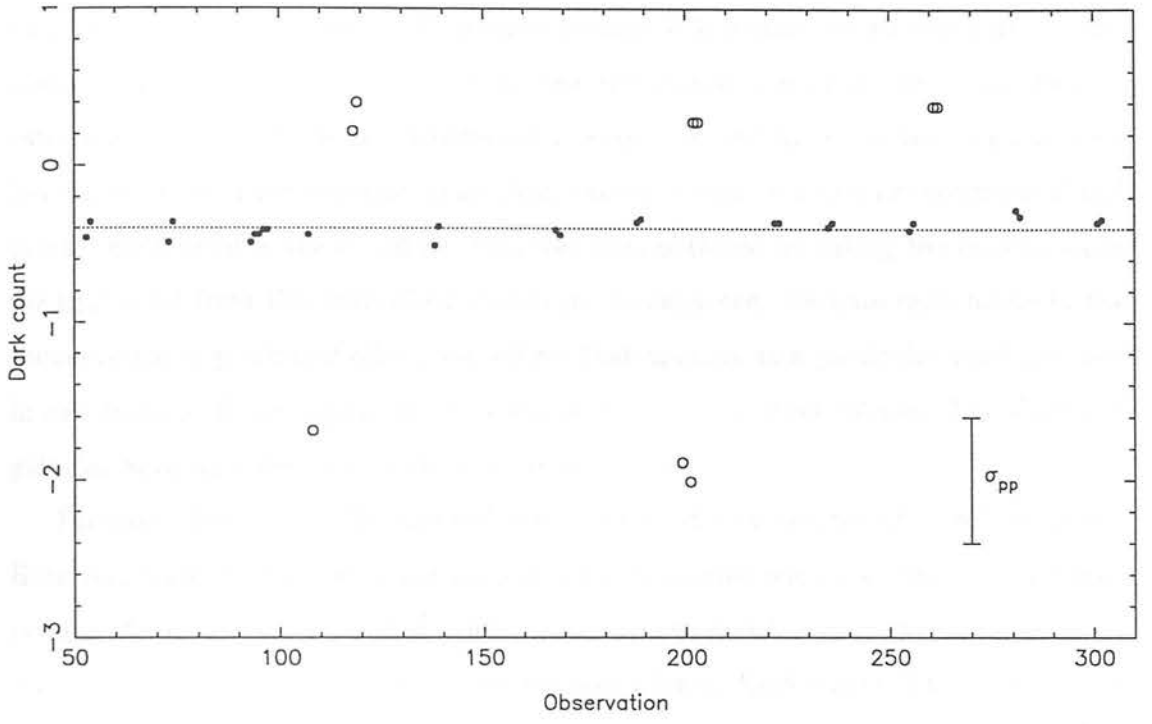

Figure 3.6: Variation in dark count throughout the night of March 5th. σ_{pp} indicates the size of the pixel-pixel fluctuations in a 20 × 20 pixel box on each dark frame. The dark exposures were for 4 coadds, 20 seconds; the points plotted here have been scaled to 1 coadd, 1 second. The open circles indicate darks taken near glitches.

Flat Fields

The aim in obtaining a flat field is to remove the stars and galaxies from the sequence to leave an empty sky frame. The flat fields were created by an iterative process, and with a new flat field for each sequence of nine frames.

First the appropriate dark was subtracted from each frame, which was then normalised by dividing by its sky value, determined from a 20 × 20 pixel box on the array. The box was chosen to avoid field objects and for consistency was at the same position on all of the frames. The sky values were estimated by the median, and the noise by the deviation from the median enclosing 68% of the values. The median was used rather than the more obvious choice of the mean because it is a more robust estimator — the mean is suited to cases where the underlying distribution is normal, but is not the best estimator in cases where the distribution is highly skewed by a few very high or very low values, caused for example by on-field sources, cosmic ray hits or intermittent bad pixels. Each pixel in the initial flat field was then obtained by taking the median value for that pixel from the normalised frames in the sequence. Because each frame in the sequence has a positional offset, any object that appears at a particular pixel position in one frame will not appear at the same position in any other frames. The stars and galaxies have, to a first approximation, been removed.

For most observations this first estimate of the flat field would be sufficiently accurate. However, because of the ghosting phenomena encountered with the narrowband filters, several of the images of on field reference stars were found to be extended over more than the 5 pixels of the positional offset between frames. Each object that was extended over more than the positional offset appeared at the same pixel position in more than one frame in each sequence, and because each sequence contains only nine images the median of the stacked frames was therefore skewed to artificially high values. The effect of this on the flat fielded images was to create dark halos around the objects. If this had been noticed at the telescope then a greater frame-frame offset could have been used, however it was not possible to see the extent of the images from the real time data analysis. The effect only became apparent from off line data reduction.

To correct for the dark halos, the flat fielding procedure was iterated to obtain an unskewed flat field. The key was to somehow flag the objects so that their high

pixels were ignored in the calculation of the median. Because it was not possible to identify the high pixels from the raw frames, the reduced images obtained from the initial estimate of the flat field were used. All pixels of $\geq 3.5\sigma$ were identified and their positions noted. The value of 3.5σ was chosen by trial and error: a higher cut off and the extremities of the object pixels were not identified, a lower value and sky noise dominated. The median filtering routine was then adapted so that when, for the second time, the normalised frames were filtered, those pixels that had been noted as high were ignored. This iterative procedure gave pixel-pixel residuals in individual images of ~ 3 parts in 10^3. This is consistent with the combination of shot noise and read noise of $\sim$ 2.9 parts in 10^3, indicating that the residual errors in the flat field are well below this level. The residuals in the final mosaiced images ranged from 3 parts in 10^5 (in the deepest field) to 3 parts in 10^4.

Bad Pixels

The IRCAM array has about 20 bad pixels, these have either a very high dark current or a very low quantum efficiency. Bad pixels can affect the photometry of the images, and if several bad pixels are grouped together they could mimic the detection of a real object.

The bad pixels were identified by examination of both the dark frames and the object frames. The dark frames were used to find the pixels with high dark current, the object frames to identify those with low quantum efficiency. Although the majority of pixels identified as bad remained bad for all of the nights, there were a few that were identified as bad on some nights whilst performing adequately on others. It was therefore necessary to create a different bad pixel map for each observing night. Figure 3.7 shows the bad pixel map for the night of 2nd March 1992. Twenty one pixels were found to be bad, with a concentration of bad pixels towards the edges of the array: the central $30 \times 30\square''$ is clear.

Bad pixels were dealt with in two ways:

1. By flagging. Each pixel has associated with it a 'quality value', the quality of a pixel being either 0 or 1. By setting the quality of all bad pixels to 1 and the quality of good pixels to 0, it was possible to flag the bad pixels. This was useful

because many of the FIGARO routines have the facility for dealing with flagged values.

2. By interpolation. The value each was replaced by a surrounding 3×3 pixel box (excluding any additional bad pixels).

By flagging the bad pixels it was possible to exclude them from the median filtering routine used to obtain the final mosaiced images. If the bad pixels had been included in the median then since each sequence contains only nine different positions, the bad pixels could skew the median to either high or low values. By excluding the bad pixels from the median the skewing is avoided. Interpolation was used as well as flagging because certain packages (such as that used to obtain the photometry) do not yet have the facility for using the information stored in the quality array, and it was feared that leaving the pixels at their bad values might have an effect on the flat fields and hence on the final images. It was subsequently found that interpolation was not crucial to the analysis — it had little or no effect on the final mosaiced images.

Extinction

The Earth's atmosphere absorbs light from any extraterrestrial source, the transmitted light is proportional to e^{-a} where a is the column density of air along the line of sight, or airmass. For a plane parallel atmosphere $a \propto \sec z$, where z is the zenith distance of the object being observed. Of course the Earth's atmosphere is not plane parallel but for zenith angles of less than 60° the effect of the plane parallel approximation on the airmass is negligible, in the third decimal place or less. The observed magnitude of an object can be expressed by the relation

$$m_\lambda(z) = m_\lambda(z = 0) + k_\lambda \sec z \,, \tag{3.9}$$

where $m_\lambda(z)$ is the magnitude at wavelength λ and zenith distance z. Once the extinction coefficient k_λ is known, the correction for atmospheric extinction can be made. For an observatory at latitude ϕ, and an object with right ascension α and declination δ, z is given by

$$\cos z = \sin\phi \sin\delta + \cos\phi \cos\delta (LST - \alpha) \,, \tag{3.10}$$

where LST is the local sidereal time of the observations. The dependence on the LST is due to the Earth's rotation and means that if a given object is observed throughout the

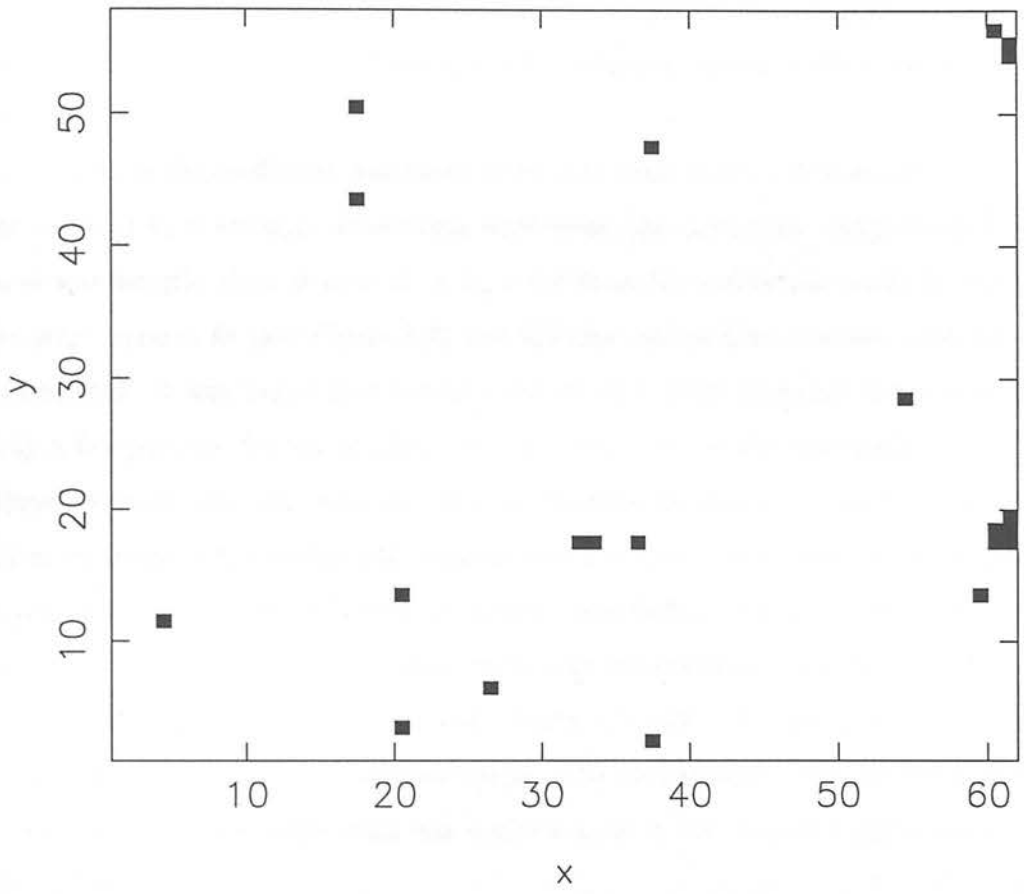

Figure 3.7: The bad pixel map for IRCAM on 2nd March 1992. The bad pixels are those shaded in black.

night its value of sec z will change. It is therefore trivial to determine the value of k_λ, as it will simply be the slope of a plot of observed brightness against sec z. In this way the magnitude of the star m_λ in the absence of the atmosphere can be found.

The usual approach (see Kitchin 1984 for a description) to determining k_λ is to observe a standard star at several different z. For the PG search it was decided to use the on field reference stars since many observations of the stars were made throughout the night. In addition to providing more points on the m-sec z graph this has the advantage of eliminating any differential extinction due to the separation on the sky of the standard and the fields, but it does assume that the reference objects remain stable throughout. In most cases two references objects were used for each field, the extinction coefficient determined from each reference object could be compared, giving a check on variability of the reference stars.

On all nights the coefficient was found to be very close to zero. This is not surprising as the value of k_λ is strongly wavelength dependent, the extinction being much less at infrared wavelengths than at optical. A $k_\lambda = 0.0$ fit to the points was made in addition to the least squares fit (see Figure 3.8) and the rms scatter from the two different fits was compared. It was found that fitting a flat m-sec z slope increased the rms scatter by only a few percent, for the brighter reference stars (which will have higher S/N) the fractional increase was less than 1%. It was therefore decided to adopt $k_\lambda = 0.0$ over the airmass range of the mosaic observations (sec $z = 1.06 - 2.08$), and as the standard stars are contained within this range in airmass (see Section 3.4) they were also taken to have an extinction coefficient of zero. Note that the standard value for extinction at J is 0.113 ± 0.01 mag/airmass (Casali, M., Aspin, C., 1991, IRCAM Users Guide), i.e. just 0.1 mag over the observed airmass range. The narrowband filters lie between the sky lines and so should suffer even less extinction, it is not therefore unreasonable to find $k_\lambda \sim 0.0$.

Mosaicing

Once the frames were flat fielded they could then be registered and combined to form the final mosaiced images for each field and each filter. No extinction correction was necessary because $k_\lambda = 0.0$. The steps taken were as follows:

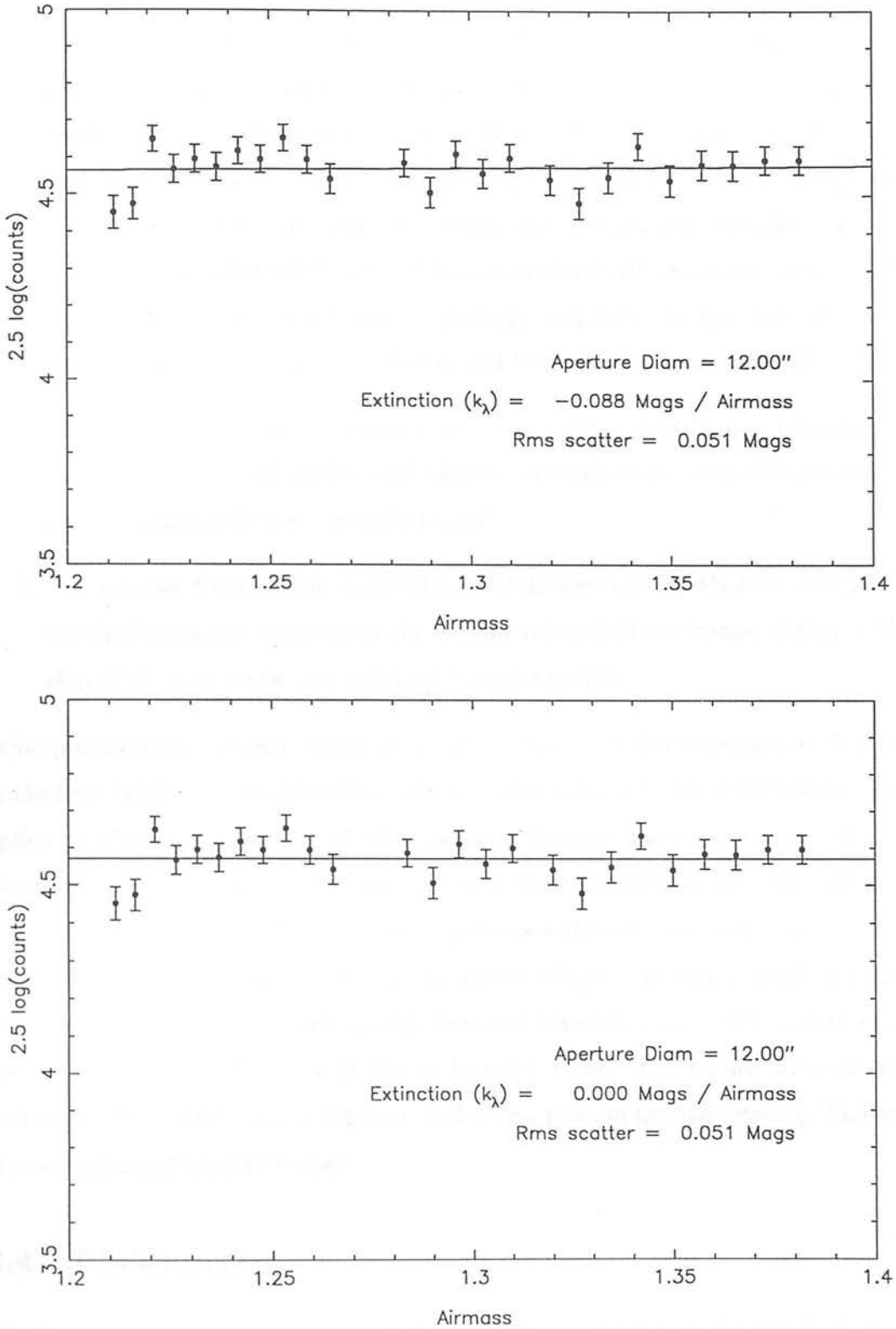

Figure 3.8: Extinction in the U1 filter on 2nd March 1992. The fits are the best least squares fit (top) and the fit with a forced gradient $k_\lambda = 0.0$ (bottom).

1. The relative offsets of each of the frames were established to the nearest pixel. Using offsets taken from the observing log of the telescope an approximate position for the on field reference stars was calculated. Accurate positions of the reference stars were then obtained from a centroiding box of aperture $A = (2 \times \text{radius}) + 1$, positioned on the estimated coordinates. Results from apertures of radius 2, 3, and 5 pixels were compared, any frame showing a discrepancy between the apertures was viewed by eye. This comparison minimised the likelihood of distortions of the centroid by intermittent bad pixels or by cosmic ray hits in a much more efficient manner than would be achieved by checking each frame by eye: typically only 5 out of a total of more than 100 frames had to be checked from each night of data.

2. The frames were normalised and then superset into larger frames, correcting for the offsets so that all images were aligned. Quality arrays were also superset, so that the bad pixels were correctly flagged.

3. The superset frames of the same filter and field were median filtered: each pixel in the final mosaiced image being the median value of all the frames of that field in that filter. Bad pixels were excluded from the median.

What proved to be a valuable check at this point was to examine the origin of each pixel in the final images. A first attempt at the median was made by using the normalisation option provided by the median filtering package. However, the check revealed that the majority of the pixels obtained in this way were found to originate from just one frame — the frame with the median sky. This was because the normalisation was by division rather than by subtraction, so that those frames with higher sky were divided by a larger number and hence had less flux in objects in the scaled frames — the median object pixels came from the frame with the median sky value. The frames were therefore normalised by subtracting the sky from each frame prior to median filtering. This gave pixels originating from all frames.

3.4 Photometry

The IRCAM output is in counts/coadd/second. For any object on the mosaiced images of the fields PG_1, PG_2, PG_3, this can be converted to a measure f of flux by means

of calibration obtained from observations of standard stars. For a given object, the flux in one of the narrowband filters is

$$f_{\rm U} = \frac{f_{\rm U}({\rm S})}{C_{\rm U}({\rm S})} \times C_{\rm U} \, , \tag{3.11}$$

where $f_{\rm U}({\rm S})$ is the flux of the standard in the narrowband filter, $C_{\rm U}({\rm S})$ the counts on the standard, and $C_{\rm U}$ the counts on the object in the narrowband filter U. $f_{\rm U}({\rm S})$ can be determined from the known J magnitude of the standard star by scaling the J flux to the width of the narrowband filter,

$$f_{\rm U}({\rm S}) = f_{\rm J}({\rm S}) \times \frac{C_{\rm U}({\rm S})}{C_{\rm J}({\rm S})} \, . \tag{3.12}$$

$f_{\rm J}({\rm S})$ the flux density of the standard star in filter J is given by

$$\log f_{\rm J}({\rm S}) = \log f_{\rm J}(0) - 0.4 m_{\rm J} \, . \tag{3.13}$$

$f_{\rm J}(0)$ is the flux of a zeroth magnitude star and $m_{\rm J}$ is the documented J magnitude. In the J passband, $f_{\rm J}(0) = 1.77 \times 10^{-23}$ Wm^{-2}Hz^{-1} $\times \Delta\nu_{\rm J}$. For the standard J waveband, $\Delta\nu_{\rm J} = 9.6 \times 10^{13}$. Hence the flux of any object imaged through a narrowband filter U can be determined.

Note that it is possible to convert flux in the narrowband filters to the J magnitude scale by making assumptions as to the spectral energy distribution of the object in question. A pure emission line object, emitting only in the narrowband filter, would have $f_{\rm J} = f_{\rm U}$, whereas a continuum object would have $f_J = f_{\rm U} \frac{\Delta\nu_{\rm J}}{\Delta\nu_{\rm U}}$, assuming a flat continuum.

3.4.1 Observation and Reduction of Standard Stars

The standard stars used were taken from the UKIRT list of bright standards, and were of J magnitudes J=7.196 mag (HD22686), J=7.155 mag (HD136754), J=7.595 mag (HD84800) and J=6.55 mag (HD40335). At least two standards were observed for each night, one at the start of observations and one at the end of the night, covering a range in airmass of $1.05 - 1.75$.

The IRCAM array saturates very quickly on the bright standard stars and so exposures were short, typically 145 msecs, 20 coadds in the broadband filters and 1 second, 20 coadds in the narrowband filters. Each standard was observed twice through each of

the filters J, H, K, U1, U2, U3 and U4, with the two observations offset by $\sim 20''$. This allows each offset observation to be used as a sky frame for the other, whilst providing two independent measurements of the flux of the object. Reduction of the standard frames was similar to that of the field frames but with the flat fielding achieved simply by dividing the standard frame by the normalised sky observation.

The location of the standard stars on the reduced images was found by the same centroiding method as that used to find the positions of the on field reference stars; a first estimate was made from the telescope observing log, from this the centroid of the standard was determined to within 1 pixel.

3.4.2 The Photometric Approach

Following Glazebrook (1991), an aperture of fixed size was used throughout. Ideally some form of fixed metric aperture would have been used, containing for example all the flux emitted from within 5 kpc of the center of the on field galaxies. However, as neither redshift information nor information on the size of any of the on field objects could be assumed a priori (i.e. whether they were Galactic stars or galaxies in their own right), it was not possible to determine such a fixed aperture. Another possibility would have been to sum up all pixels above some intensity threshold. Such a photometric scheme however has systematic problems; it underestimates the total flux of faint objects since for a fainter object fewer pixels will lie above the threshold. Another effect is that the flux obtained by such a method will include sky photons above but not below the adopted sky level (i.e. will include positive but not negative sky noise). A third approach would have been to measure the total flux for ever increasing apertures and then to try to extrapolate to an infinite aperture to estimate the total flux emitted by the object. Each resolved object would have a different shape and orientation and hence different flux-aperture dependencies, the extrapolated flux would therefore have to be determined for each in turn.

All three of these schemes are unsatisfactory and, in particular, would be hard for another investigator to reproduce. The simplest and most consistent photometric approach is to use a fixed size aperture, one fixed in terms of its radius in pixels. If the aperture is too small, the flux of the object will be underestimated. If the aperture is too big, sky noise and contamination from other objects intrudes.

Our approach was to obtain curves of growth (COGs) of flux versus increasing aperture for several of the reference stars and for the standard stars. A schematic of such a COG is shown in Figure 3.9. Over region A, increasing the size of the aperture brings in an increasing amount of flux; the limiting isophote of the object has not been reached. The flux variations over region C reflect the rms noise of the sky. The upward slope, greatly exaggerated, indicates either the presence of nearby contaminating objects or the use of a sky level that is too low. The ideal aperture is one in region B.

We obtained COGs for each standard and for each reference star in both broad and narrow passbands, and concluded that the best aperture diameter is one of 10 pixels (12"). The narrowband images of the (bright) standard stars show a significant positive gradient, as much as 16% of the total flux of the standard, in region C. This gradient was not evident in the broadband images, and its most likely explanation is that flux is being ghosted to larger radii from the object centre as a result of reflections from within the narrowband filters themselves. The curves of growth for the narrowband fluxes were of similar shape and therefore the choice of aperture should not greatly effect the narrowband colours. Note that the J COGs level out at apertures of more than 10", and so the narrowband-broadband colours will be affected to some extent by the choice of aperture.

As absolute photometry is not crucial to the PG search, and since increasing the size of the aperture risks introducing contaminating objects, it was decided that the 10 pixel diameter is the optimum choice of aperture. In practice however, it was not possible to use a 10 pixel aperture for photometry of the on field objects, since the separation between several of the field objects was less than 12". The on field aperture had to be made smaller, down to a diameter of 6", and the flux scaled to account for the difference in aperture (a correction of 0.08 mag). Any bad pixels were ignored, and no pixels were found to be saturated.

The observations of the standard stars gave a count-to-flux calibration for each standard on each night. There was no evidence that the calibration varied from standard to standard on a given night (i.e. the effect of different airmasses was negligible) nor that for a given standard the calibration varied substantially between nights. The individual estimates of the count-flux ratio were therefore combined to give an estimate of the

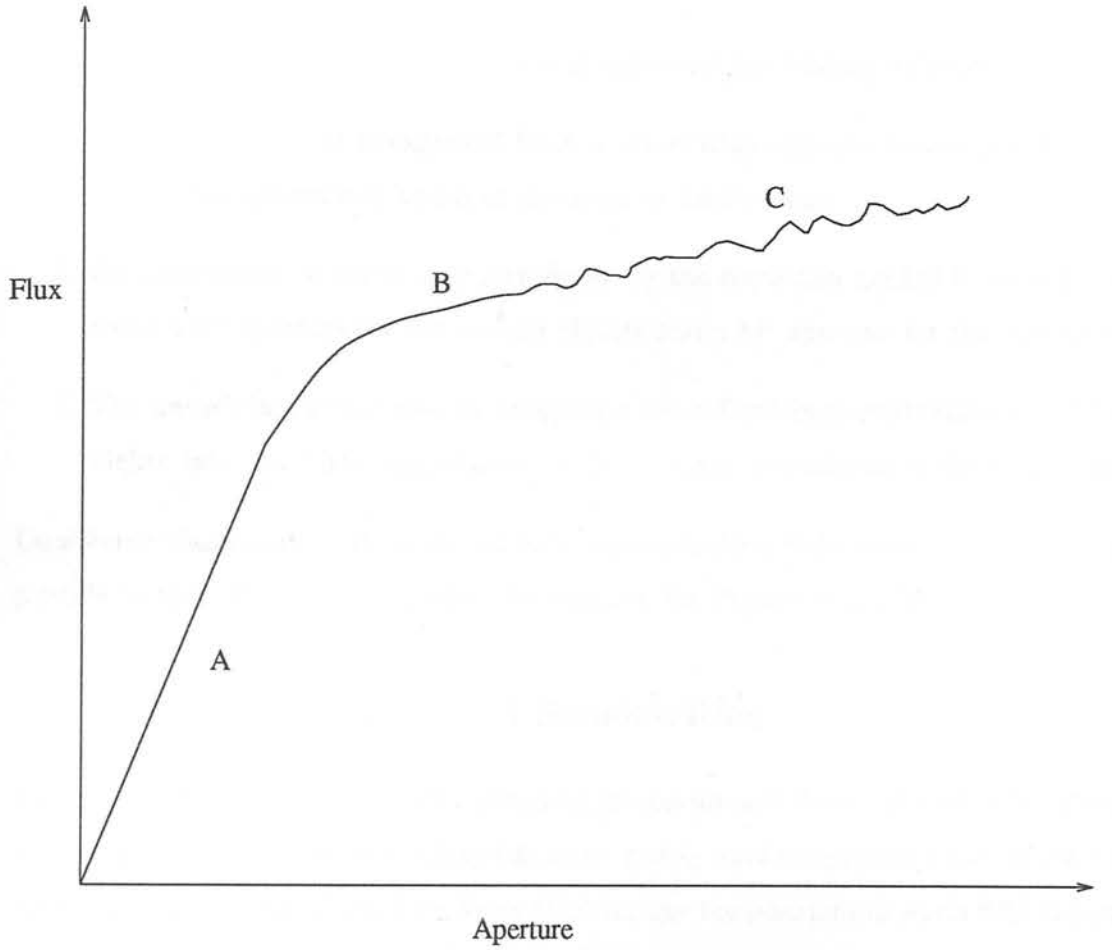

Figure 3.9: A typical curve of growth (not to scale).

calibration ratio κ where

$$\kappa = \frac{f_U(S)}{C_U(S)} . \tag{3.14}$$

The data from all the nights gave $\kappa = 5.6 \times 10^{-18}\mathrm{Wm}^{-2}$/counts/sec with a standard deviation of $0.3 \times 10^{-18}\mathrm{Wm}^{-2}$/counts/sec. From the estimate of κ, fluxes in the narrowband filters could be calculated from the measure of their counts. κ is often given in magnitude terms when it is described as the zero point m_{zero}. In this case $m_{\mathrm{zero}} = 21.25$ with a standard deviation of 0.06 mag.

It is possible to estimate the uncertainty in the flux calibration. This uncertainty has several components.

1. Observational systematics such as read noise and flat fielding residuals.

2. Sky shot noise. For background limited observations this dominates over the observational systematics and is of the order of ± 0.001 mag.

3. An uncertainty of ± 0.01 mag introduced by the correction needed to account for using a 6 " aperture for the on field objects and a 12" aperture for the standards.

4. The uncertainty introduced by adopting a mean flux/count calibration for all the nights data. At ± 0.06 magnitudes this is the major contributor to the uncertainty

Combining these contributions we estimate our calibration to be accurate to 6%, comparable to that of other PG searches (for example De Propris et al., 1993).

3.5 Reduced Images and Sensitivities

Figures 3.10 to 3.15 display the final mosaiced images for each filter and each field. These images include data from both observing runs, giving total integration times of $2.5 - 5$ hours in each field (see Table 3.4). From these images the positions of all on field objects could be established, and then from their photometric colours any candidate primeval galaxies selected for subsequent spectroscopic investigation.

3.5.1 Object Detection and Sensitivity

To locate the position of objects from the mosaiced images we applied a criterion of 3σ over 3 adjacent pixels, requiring a total flux of at least $3\sqrt{3}sd$, where sd is the pixel-pixel

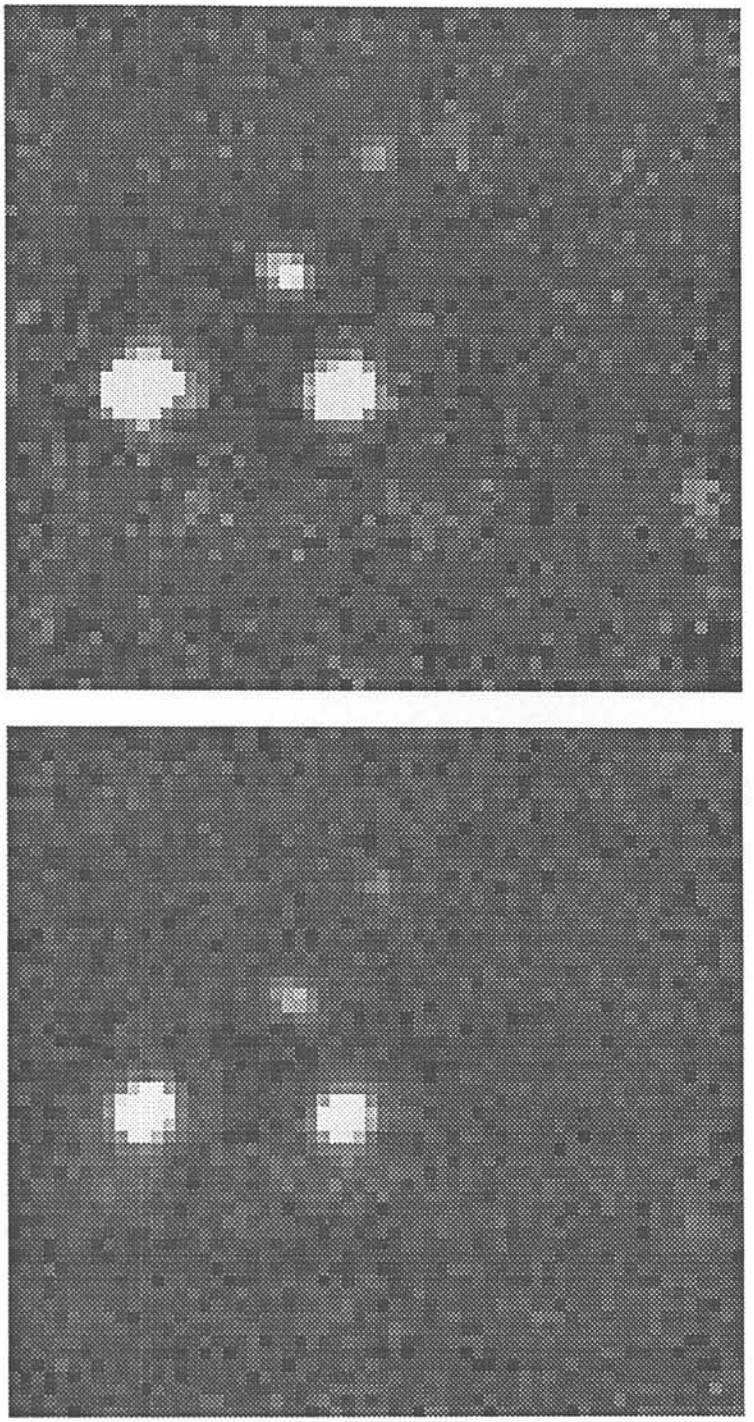

Figure 3.10: Mosaiced images of field PG_1 in U1 (top) and U2 (bottom). Black corresponds to -5 sigma, white to +50 sigma, where sigma is the pixel-pixel fluctuation.

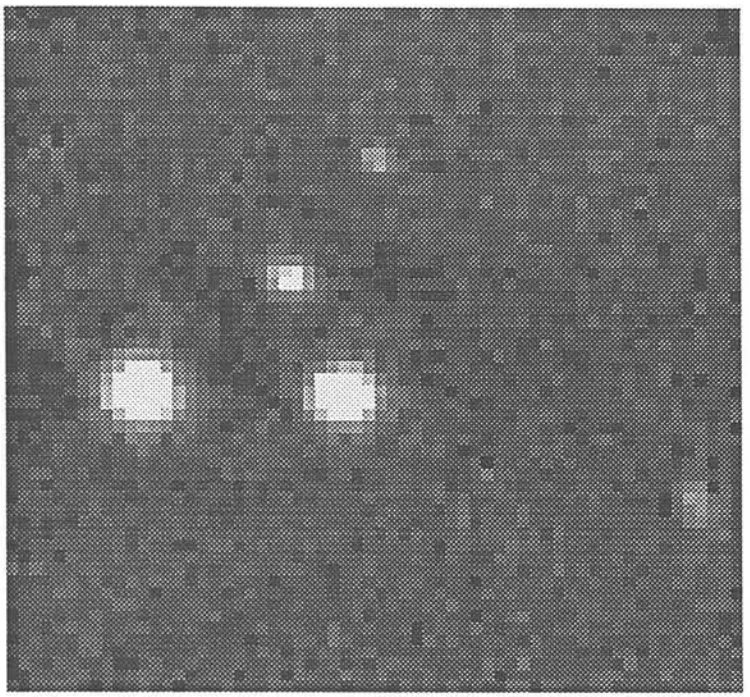

Figure 3.11: Mosaiced images of field PG_1 in U4. Black corresponds to -5 sigma, white to +50 sigma, where sigma is the pixel-pixel fluctuation.

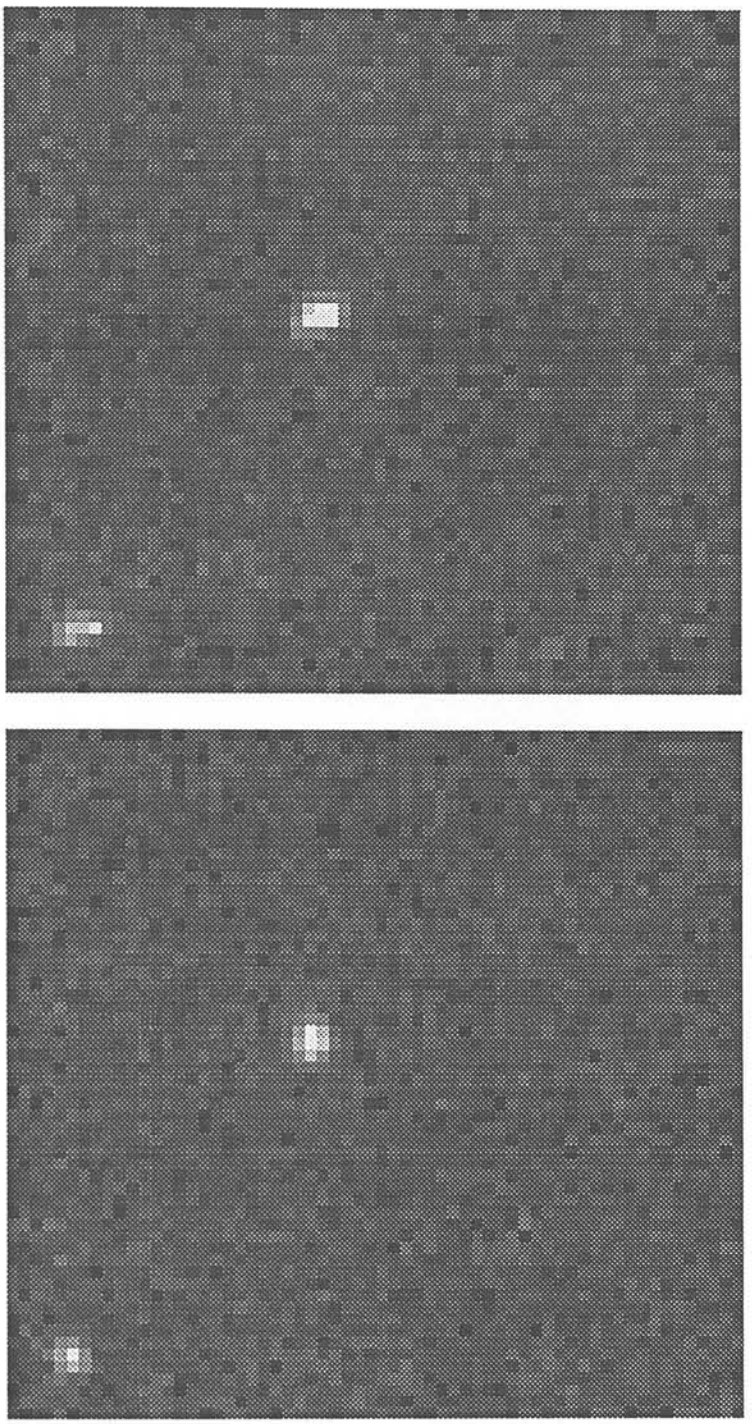

Figure 3.12: Mosaiced images of field PG_2 in U1 (top) and U2 (bottom). Black corresponds to -5 sigma, white to +50 sigma, where sigma is the pixel-pixel fluctuation.

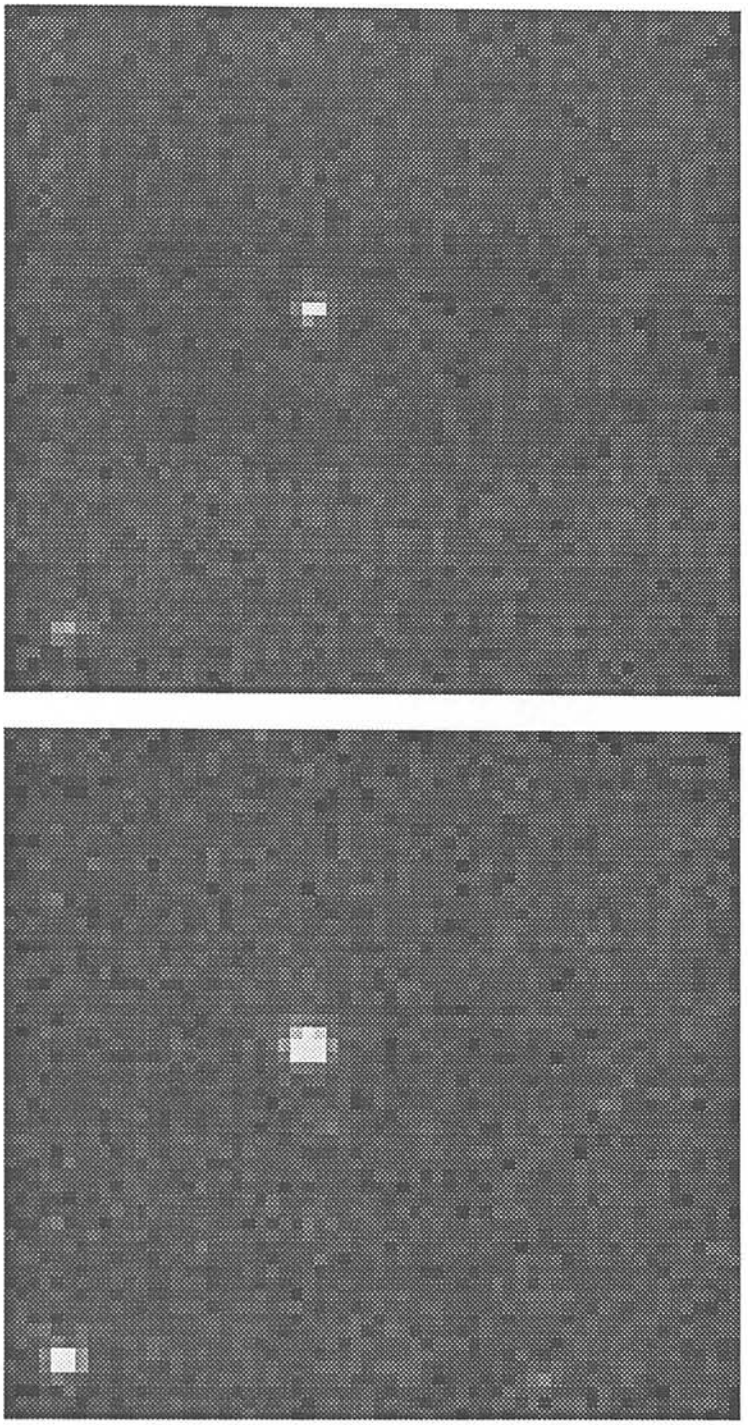

Figure 3.13: Mosaiced images of field PG_2 in U3 (top) and U4 (bottom). Black corresponds to -5 sigma, white to +50 sigma, where sigma is the pixel-pixel fluctuation.

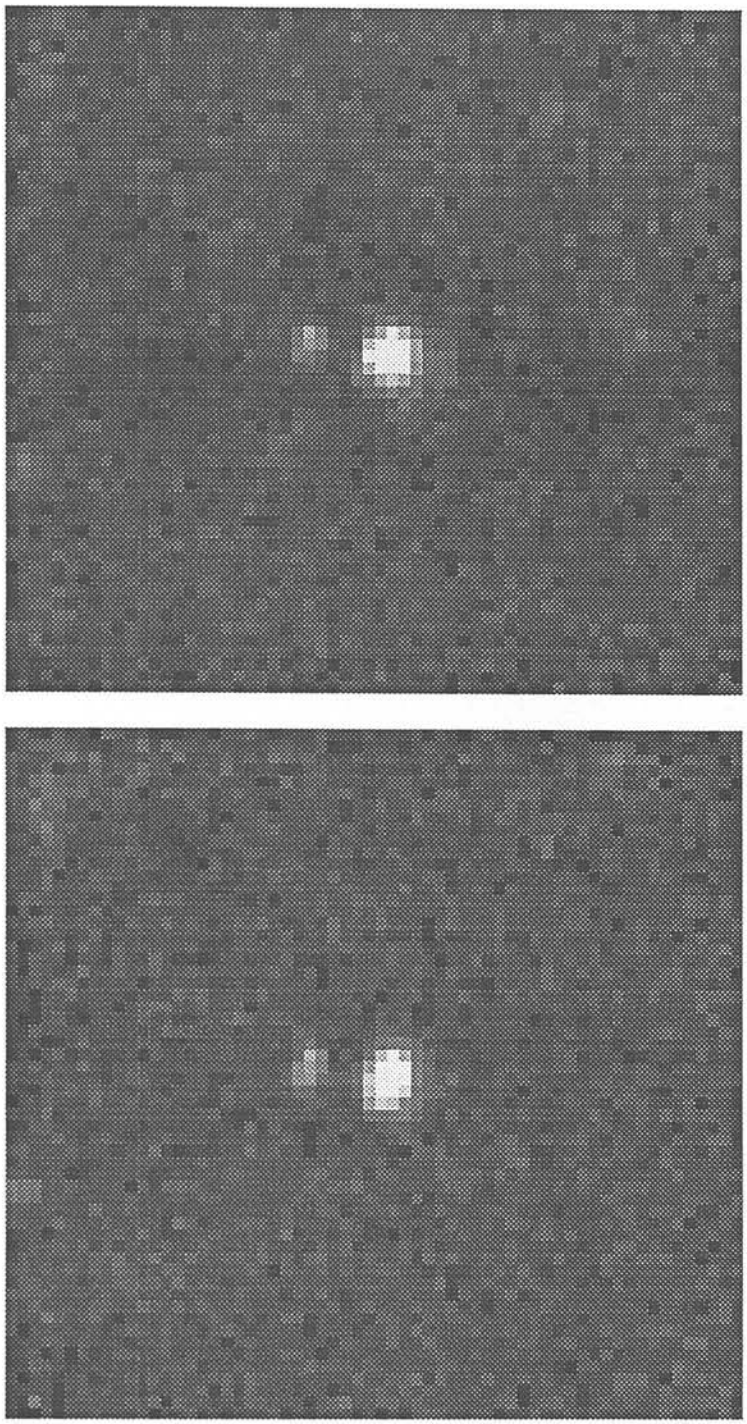

Figure 3.14: Mosaiced images of field PG_3 in U1 (top) and U2(bottom). Black corresponds to -5 sigma, white to +50 sigma, where sigma is the pixel-pixel fluctuation.

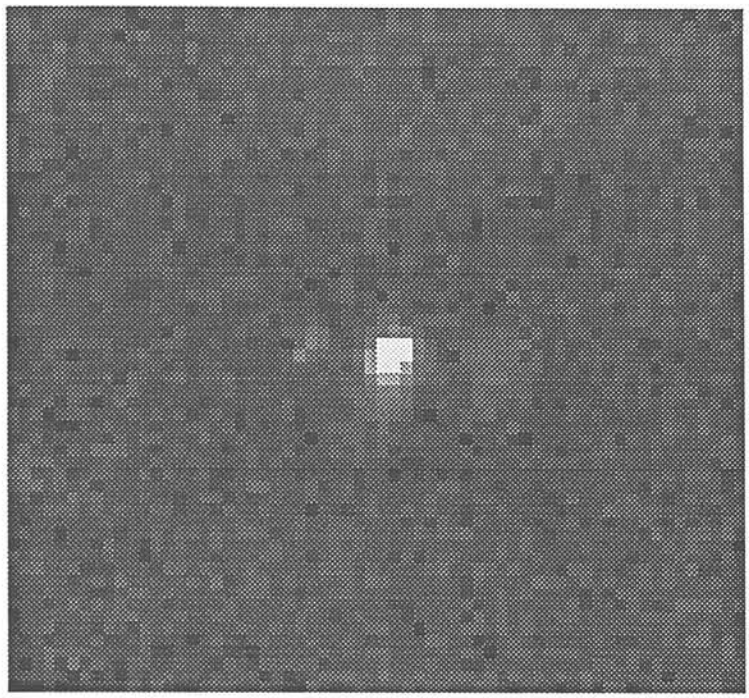

Figure 3.15: Mosaiced images of field PG_3 in U3. Black corresponds to -5 sigma, white to +50 sigma, where sigma is the pixel-pixel fluctuation.

Table 3.4: Total integration times in each field.

Field	Filter	Total Integration Time (hrs:mins)
PG_1	U1	5:18
	U2	4:00
	U4	3:30
PG_2	U1	4:22
	U2	2:50
	U3	2:50
	U4	2:26
PG_3	U1	3:38
	U2	3:30
	U3	2:42

sky variation determined as the deviation from the median enclosing 68% of the pixel values in a 20 × 20 pixel box. This criterion gave 6 objects in field PG_1, 3 objects in PG_2, and 5 in PG_3. The position of the objects and their flux in each filter are given in Table 3.5.

The limiting sensitivity of the search, i.e. the brightest object that would escape detection, can be estimated by the flux that would satisfy the detection criterion, i.e. $3\sqrt{3}sd$. These limits are given in Table 3.6 and are appropriate for the inner 1.0□' area of the mosaiced frames which is covered by all offset positions. An area of 2.0□' is covered to a higher flux limit.

Is the search as sensitive as expected? An investigation into the increase in sensitivity with integration time can be made by plotting the limiting flux as a function of the number of images (i.e. integration time) included in the mosaic. This is done in Figure 3.16. The y axis gives the sensitivity of the image as measured by the pixel-pixel standard deviation in the 20 × 20 pixel statistics box, this is plotted against the total integration time of all frames used in the mosaic. For a consistent comparison only data made in the NDR mode has been included. The integration times range from

Table 3.5: Position and Flux of objects detected in the IRCAM search.

Object	RA_{1950}	DEC_{1950}	Flux $10^{-18}Wm^{-2}$			
			U1	U2	U3	U4
PG_1_1	09:18:05.4	-00:19:24.8	269	188	-	337
PG_1_2	09:18:03.9	-00:19:25.4	155	111	-	219
PG_1_3	09:18:04.3	-00:19:14.1	9.40	8.57	-	19.9
PG_1_4	09:18:03.7	-00:19:02.9	2.21	2.28	-	5.26
PG_1_5	09:18:03.1	-00:19:01.3	1.15	≤ 0.18	-	≤ 0.20
PG_1_6	09:18:01.4	-00:19:34.8	3.19	2.04	-	6.47
PG_2_1	13:41:50.2	00:07:35.5	16.7	14.5	17.4	22.8
PG_2_2	13:41:58.5	00:08:05.5	32.8	29.1	56.7	78.8
PG_2_3	13:41:56.9	00:07:33.6	1.7	≤ 0.32	≤ 0.92	0.67
PG_3_1	09:18:10.7	-00:20:30.5	5.05	7.77	10.6	-
PG_3_2	09:18:08.6	-00:20:18.3	2.31	1.03	-	-
PG_3_3	09:18:08.1	-00:20:19.3	204	212	244	-
PG_3_4	09:18:06.9	-00:19:56.7	2.37	1.93	14	-
PG_3_5	09:18:06.3	-00:20:18.3	4.00	≤ 0.41	≤ 1.7	-

Table 3.6: Flux limits: 3σ in 3 pixels.

Field	Filter	z	Limiting Flux 10^{-19} Wm^{-2}
PG_1	U1	7.2	0.9
	U2	7.8	1.8
	U3	8.7	-
	U4	9.3	2.0
PG_2	U1	7.2	2.9
	U2	7.8	3.2
	U3	8.7	9.2
	U4	9.3	3.0
PG_3	U1	7.2	3.6
	U2	7.8	4.1
	U3	8.7	10.7
	U4	9.3	-

single observations to one night's data, one run's data, and the final mosaics of both runs. For background limited observations, the relationship between integration time and sensitivity is described by Poisson statistics, i.e.

$$S \propto \frac{1}{\sqrt{t}} \tag{3.15}$$

where S is the image sensitivity and t the total integration time. Although there is a fair amount of scatter in the plot, Figure 3.16 shows that the general trend is well fitted by the Poisson prediction. Note that the data points are taken from images of all three of the fields, which will in itself introduce scatter.

3.5.2 Candidate Objects

Candidate PGs were selected from the objects detected in each field by appealing to the predictions of the spectral energy distribution of primeval galaxies. The selection procedure was simply this: a PG candidate is any object that is present in one narrowband image of a field but not in the other narrowband images.

Such a simple selection procedure is possible because of the large equivalent width predicted for the Lyα emission line: while the search is sensitive enough to detect the Lyα line, the continuum is too weak to be detected. Figure 3.17 shows the rest frame 3 pixel 3 σ luminosity limits for each field in each filter (see Chapter 5). Also marked on the figure is the range of Lyα luminosity expected for the PG population. As an upper limit I have taken the brightest PG predictions (see Chapter 2). As the lower limit on Lyα luminosity I have taken the high end of the SFR (0-20 $M_\odot$) seen in normal disk galaxies, converted to Lyα flux using the semiempirical conversion of SFR to Hα luminosity of Kennicutt (1983), see Chapter 5. It is evident that if the Lyα line is as luminous as predicted by the brighter PG models then a significant detection would be possible. In contrast it can be seen that the flux expected in the narrowband filters from the UV continuum of a PG lies well below the sensitivity of the search. The continuum prediction plotted in Figure 3.17 comes from Meier (1976), who by combining the hydrodynamical models of Larson (1974) with stellar population synthesis finds the spectrum longward of the Lyman break to be fairly flat with a luminosity of $\sim 10^{23} \mathrm{WHz}^{-1}$, with little model dependence. Although the search is sensitive enough to detect the brighter predictions for the Lyα emission line, there is no chance of a detection of the PG continuum. This

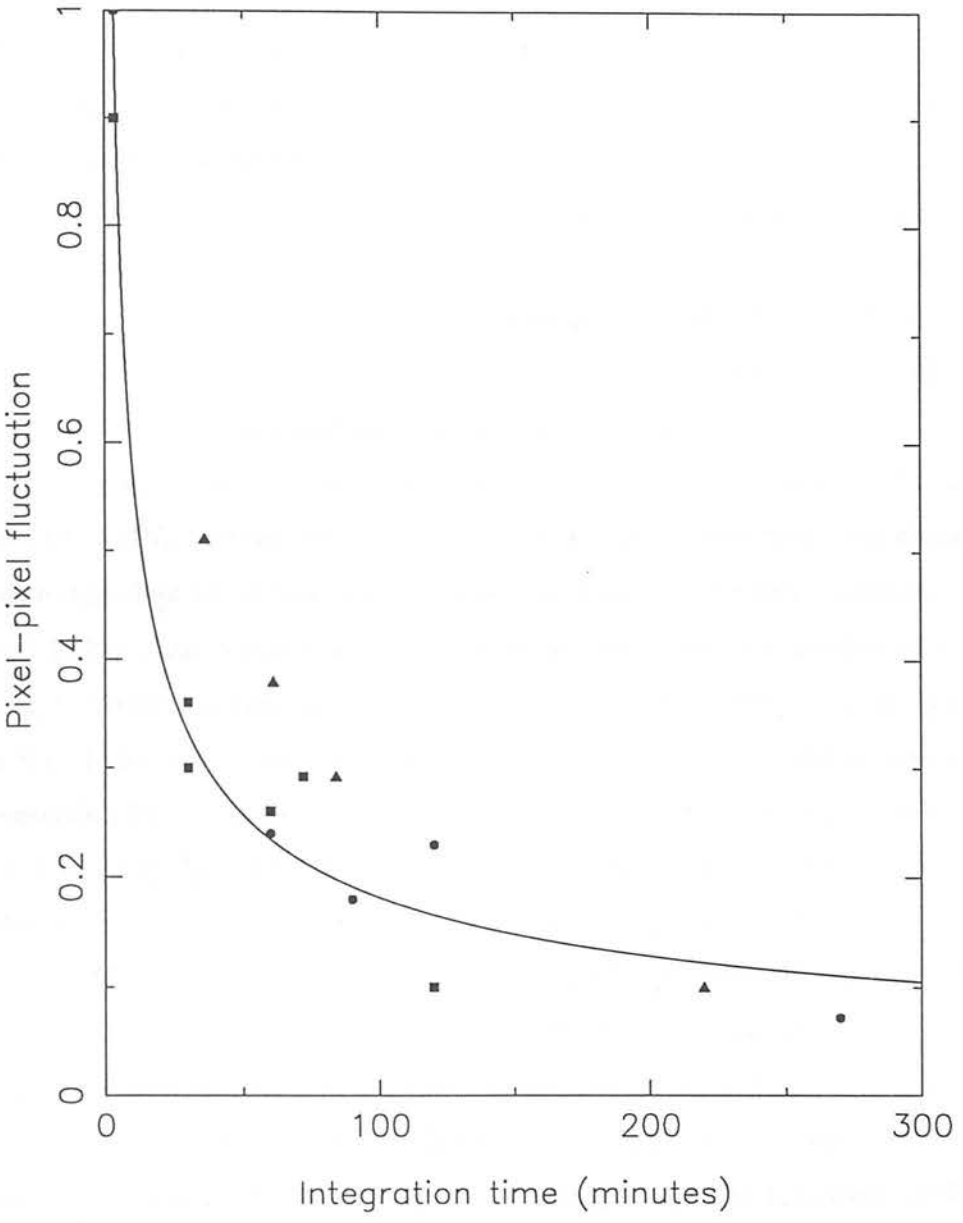

Figure 3.16: The relationship between sensitivity and total integration time of mosaiced images (NDR mode data). Circles represent data from field PG_1, squares from PG_2, and triangles from PG_3. The curve shows the sensitivity expected from Poisson statistics, with normalisation to a single integration.

gives us the characteristic PG signature: a detection in one and only one of the four narrowband filters.

Although other emission lines may be present in the spectral energy distribution of PGs, these lines would lie at much longer wavelengths. For example if the Lyα line falls in filter U1, then the oxygen line [OII] 3727$\AA$ will fall at 3.05μm, which is well outside the J passband. Other features commonly seen in emission line galaxies, such as the Balmer lines, lie at even longer wavelengths.

An additional check on any candidates was made by examining the broadband B, V and R images of the same fields (Glazebrook 1991). These images have a limiting magnitude of 21.3, 24.1 and 23.8 mags respectively (3σ, 4□"). Since a PG at $z \geq 7$ will have its Lyman break redshifted longwards of the R band, any PGs at such redshifts will not be detectable in broadband images shortward of R.

Applying these colour criterion gave two candidates, both in filter U1 (1.01μm), one in field PG_1 (PG_1_5) the other in PG_3 (PG_3_5). The colours of the remaining objects indicate that they are normal stars or early type galaxies. The first candidate, hereafter termed PG_1C, was found from reduction of the 1991 data, at a position of 09:18:03.1 (RA_{1950}), -00:19:01.3 (Dec_{1950}). It has a flux of 3.2×10^{-18} Wm^{-2} in the narrowband filter U1. This is equivalent to a J magnitude of 21.8 for a pure emission line object and the detection has a significance of 16σ. If the line is indeed Lyα then its luminosity at $z = 7.2$ is 1.4×10^{38}W . It has a significant extent, with a diameter of 4 pixels (5") which at a redshift of 7.2 corresponds to a proper diameter of 23kpc ($\Omega = 1$, H_0=50 $kms^{-1}Mpc^{-1}$). Reduction of the 1992 data revealed the second candidate, hereafter termed PG_3C. This is a 14σ detection, with a flux of 4.0×10^{-18} Wm^{-2} in the narrowband U1 filter, or a J magnitude (assuming that it is a pure emission line object) of J= 21.5. This object is more compact than PG_1C, with a diameter of 2 pixels (2.5"or 12kpc at $z = 7.2$). Its position is 09:18:06.3 (RA_{1950}), -00:20:18.3 (Dec_{1950}). The Lyα luminosity of PG_3C at a redshift of 1.8×10^{38}W (Ω=1, H_0 = 50 $kms^{-1}Mpc^{-1}$).

Both of the objects have diameters of the order expected for PGs: Partridge and Peebles (1967) predict a diameter of 30kpc or less, Meier's models have 75% of the star formation in a PG occurring in a diameter of 10-22kpc. The detections lie midrange in the Lyα line predictions for PGs of 10^{35}-10^{38} W. It is however possible that the detections are spurious images caused by 'ghosting' in the narrowband filters. It was therefore

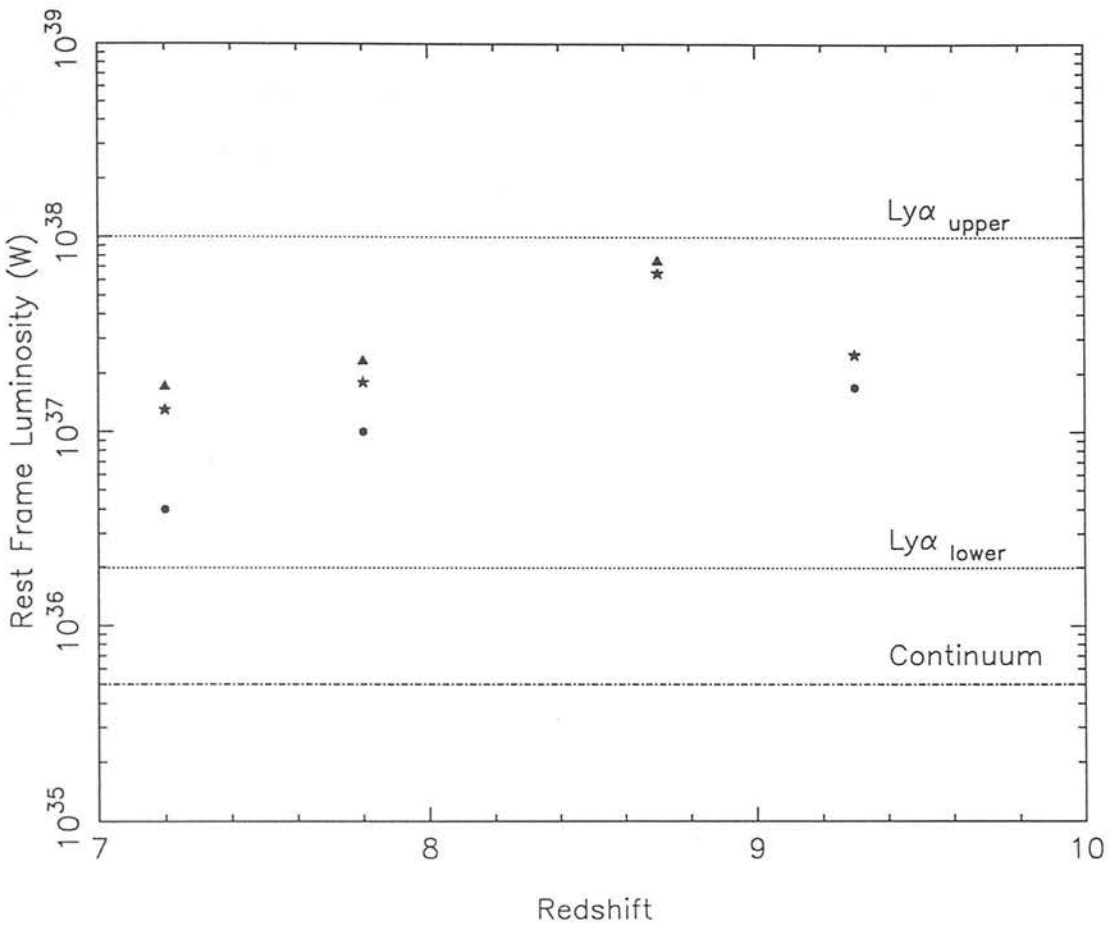

Figure 3.17: Sensitivity of the PG search as expressed by the rest frame flux limit in each filter. Circles represent PG_1, stars PG_2 and triangles PG_3. Limits are 3σ over 3 pixels. The dotted lines represent the range expected for unobscured Lyα emission, the upper limit from the bright PG predictions, the lower limit from the high end of SFR of normal disk galaxies, assuming no obscuration by dust. The dot-dash line indicates the UV continuum flux predicted by Meier. $\Omega = 1$, $H_0 = 50$ kms^{-1}Mpc^{-1}.

necessary to confirm the reality of these objects at 1μm before further investigation into their nature was made at other wavelengths.

3.6 Summary

This chapter describes the first high redshift search for Lyα emission from primeval galaxies. The search covers the emission of Lyα at four discrete redshift bands over a range of $7.2 \leq z \leq 9.3$. Two objects are found having the characteristics of primeval galaxies. Because of the expected 'ghosting' in the narrowband filters, it was necessary to confirm the reality of these objects at 1μm before further investigation into their nature could be made at other wavelengths. The investigation is described in Chapter 4.

Chapter 4

Investigation of the Candidates

The IRCAM search described in Chapter 3 revealed two objects, PG_1C and PG_3C, that show the characteristics expected for primeval galaxies; colours indicative of emission line objects, with sizes and luminosities in the ranges predicted by galaxy formation models. This chapter describes the subsequent investigation of these objects with the cooled long slit spectrometer CGS4. The aim of the investigation was to confirm the 1.01μm IRCAM detection with an independent instrument, and to obtain infrared spectra allowing further identification of the objects to be made.

4.1 A Description of CGS4

CGS4 is a 1-5μm grating spectrometer installed on UKIRT (Mountain et al. 1990). It uses a 2 dimensional InSb array of 58 x 62 pixels, cooled by liquid nitrogen and by closed cycle coolers. The usable slit is 80" long, with a width of one pixel. There is a choice of three gratings: 75 lines/mm, 150 lines/mm and a 31 lines/mm echelle. For these observations we used the 75 lines/mm grating in the second order, which gives a resolution of $\lambda/d\lambda = 383$ and a spatial scale of 3.1"/pixel.

Sensitivities are documented down to 1.25μm, where the sensitivity for a 3σ, 30 minute fully sampled spectrum of a point source, with sky subtraction made by nodding up and down the slit, is 3.2×10^{-19} Wm^{-2} (for unresolved lines). It is known that the quantum efficiency of the array falls off at short wavelengths, which means that the sensitivity at the 1.01μm of the IRCAM detections will be worse than the value at 1.25μm, by a factor of as much as 2 – 3 (P.J. Puxley, personal communication). In addition there is a drop of approximately 40% in the CGS4 filter transmission between 1.25μm and 1.01μm, which will further reduce the sensitivity of the instrument at the short wavelength end. Below 0.95μm the blocking filter cuts in, defining the short wavelength limit of the grating.

4.2 CGS4 Observations of the PG Candidates

Both CGS4 spectra were obtained by the UKIRT service programme. PG_1C was observed in January 1992, and PG_3C in January 1993. In view of the fact that the objects themselves are too faint to check the pointing of the detector, we used the following procedure to insure against a false negative detection. The slit orientation was chosen so that, when the candidate was in the correct pixel, a reference object was positioned further down the slit (see Figure 4.1). We peaked up on a nearby bright star, with the bright star placed at the pixel chosen for the candidate. We then moved the slit to place the candidate in that chosen pixel. The position and orientation of the slit were correct if the reference object was detected in the expected pixel.

Observations consisted of object-sky pairs formed by nodding the telescope 15" along the slit, and each observation was fully sampled by moving the detector a small number of steps and taking an integration at each position. For example, observations made

with 4/2 sampling were composed of 4 individual integrations, 2 made at one detector position, 2 at a second position offset by 1/2 a pixel along the slit. Flat fielding was achieved by using the 1073K blackbody contained in the CGS4 calibration unit, wavelength calibration by using a krypton arc lamp, and flux calibration was from observations of a Mauna Kea primary standard, star BS3188. Because the absorption of light from both the standard star and from the object will depend on the path length through the atmosphere (see Section 4.3.3), the standard star was chosen to have an airmass as close as possible to that of objects PG_1C and PG_3C.

Integration times for the PG candidates were estimated from the fluxes detected in the filter U1. Because the CGS4 resolution exceeds that of the narrowband filters, the integration time required for a significant detection depends on the width of the emission line, $\Delta_{\rm line}$. A very narrow line would be detected sooner than a broad line since the same amount of flux would be spread over fewer pixels in the spectral direction. The integration time $t_{3\sigma}$ required for a 3σ detection is given by

$$t_{3\sigma} = \left(\frac{S}{F}\right)^2 \times 30\text{minutes}\,, \tag{4.1}$$

where S is the sensitivity of the instrument (taken to be a factor of 3 worse than the sensitivity at 1.25μm, i.e. $S = 9.6 \times 10^{-19}$ Wm^{-2}) and F is the expected flux in a resolution element. The longest integration time required for a 3σ detection of the candidates, for a line just resolved by the IRCAM filter U1, would be

$$F = F_{\rm U1} \times \frac{\Delta\lambda_{\rm R}}{\Delta\lambda_{\rm U1}}\,, \tag{4.2}$$

where $F_{\rm U1}$ is the flux in the U1 filter, $\Delta\lambda_{\rm U1}$ is the bandwidth of filter U1 and $\Delta\lambda_{\rm R}$ is the width of the CGS4 resolution element. Substituting the U1 fluxes of PG_1C (3.2×10^{-18} Wm^{-2}) and PG_3C (4.0×10^{-18} Wm^{-2}) into Equation 4.2 gives integration times of 2.6 hours and 1.7 hours respectively. These are the maximum times predicted for a 3σ detection of the objects. If the emission lines are in fact unresolved by U1 then the integration times will be less, down to the limiting case where the line is unresolved by CGS4, at which point $F = F_{\rm U1}$ and $t_{3\sigma} = 2.7$ minutes (PG_1C), $t_{3\sigma} = 1.7$ minutes (PG_3C).

4.3 Data Reduction

The data for both objects were reduced using the CGS4 data reduction package CGS4DR, described in Starlink User Note 27.1 (Daly P.N., & Beard S.M., 1992). CGS4DR is a sophisticated semiautomatic data reduction package capable of both on and off line analysis. The PG_1C data were reduced off line, the PG_3C data were reduced on line by the service team. Described below is the reduction procedure used in analysing PG_1C. The framework for the analysis of PG_3C was similar.

4.3.1 From Raw Frames to Reduced Groups

Using CGS4DR, raw data frames or *integrations* taken at a single detector position were reduced by applying a bad pixel mask, subtracting a bias, linearising, subtracting a dark and then flat fielding to give *reduced integrations*. The bad pixel mask was FPA61_75. Since no measurable non-linearity has been found with the CGS4 array to within 98% of full well capacity, the linearising facility was not used in our reduction. The flat field was obtained from the black body in the calibration unit, reduced in an identical manner to the integrations but with the last step replaced by a normalisation algorithm. The choice of bias, dark, flat and other calibration frames such as the arc and standard star observations was made automatically by the software. In general, the frame used was that nearest in time that matches the instrument configuration at the time of the observation.

Using the descriptions (stored as *observations*) of the instrument configuration for each integration, the reduced integrations were then interleaved to give oversampled spectra. These *reduced observations* were wavelength calibrated using a scale estimated from the grating wavelength and dispersion. From each reduced object observation a reduced sky observation was then subtracted, and all object-sky pairs relating to each astronomical object coadded into *reduced groups*. Individual sky subtracted frames were checked before adding into the group, to avoid the inclusion of any glitched data. Because the sources were expected to extend only over one or two pixels, it was possible to make enhanced sky subtraction by fitting a 1st order polynomial to two regions of sky on either side of the objects of interest. A higher order polynomial would have been justified if a large number of sky rows had been available, however the positioning of a reference object

in the slit left only a few rows of sky surrounding the objects. The coadding routine disregards any error information in the individual observations (which, since only four integrations are combined to form each observation, will be poorly determined). Errors were therefore propagated from the standard error in the signal from observation to observation.

4.3.2 Extracting the Spectra and Wavelength Calibration

The reduced groups are 2 dimensional images with the spatial direction along one axis and wavelength along the other. From these images the 1-D spectra of the objects were extracted by adding the signal from the appropriate object row with that from the two adjacent rows. Although increasing the number of rows from one to three increases the sky noise in the spectra, it ensures that all the light from the object has been extracted — some of the light may have spilled from the object row into adjacent rows (the pixel size is 3", the size of the candidates 5" or less). Although an alternative extraction method is possible which combines rows using weights based on the spatial profile of the image, it is not suited to the low signal to noise data of our data where the effect of profile fitting is in fact to increase the noise.

Object-sky pairs had been formed by nodding the telescope along a third of the slit's length, and so each sky frame contains an offset spectrum of the object. Negative object spectra were extracted from each group, multiplied by -1, and then added to the positive object spectra effectually doubling the on-object integration time.

CGS4 spectra are oversampled by combining several integrations at different detector positions, and so it is possible for a change in seeing conditions during the scan to result in a periodic ripple on the spectra. Any such seeing ripples were removed by dividing the spectra by a normalised ripple spectrum, generated by folding the data over a region of the spectra that can be assumed flat.

Reduced spectra of the objects PG_1C, PG_3C, the standard star BS3188 and the krypton arc lamp were produced following the framework described above. At this point in the data reduction all the spectra had only an estimated wavelength scale. A truly calibrated scale was established from the arc spectrum, which was extracted from the same rows on the image as the object rows. The same rows were used as a safeguard in case the wavelength calibration varies across the array, for which there is no evidence.

The arc lines were identified, fit by a polynomial (a third order polynomial was found to provide the best fit) and an accurate wavelength array established. The object spectra were then calibrated by adopting the wavelength axis array of the arc file. Since the wavelength fit was non linear the data had to be rebinned to maintain a linear scale.

4.3.3 Flux Calibration

The final step of the reduction was to use the standard star spectra to correct for any atmospheric absorption effects and to calibrate the spectral flux. All spectra of extraterrestrial objects will be altered by the effects of the Earth's atmosphere. In the infrared, the presence of water vapour and CO_2 gas makes the atmospheric transmission highly wavelength dependent, significantly changing the shape and features of any spectra. The observed spectra will also depend on the wavelength response of the detector.

The way forward is to compare the source with the spectrum of an object that has a well established spectral shape, i.e. that of the standard star. The standard star is of early type and is therefore known to have a very flat spectral energy distribution which approximates very well to a black body source. It is then possible to recreate the true spectrum $S_{\text{source}}(\lambda)$ of a source from its observed spectrum $S_{\text{obs}}(\lambda)$ and from the observed spectrum of the standard star $S_{\text{standard}}(\lambda)$.

The observed flux density of an object is given by

$$S_{\text{obs}}(\lambda) = S_{\text{source}}(\lambda)T(\lambda)R(\lambda)\,, \tag{4.3}$$

where $T(\lambda)$ is the atmospheric transmission at a given wavelength. $R(\lambda)$ describes the instrumental response at that wavelength and includes the absolute flux calibration term. Because the standard star has a spectral shape very close to that of a black body

$$S_{\text{standard}}(\lambda) \approx B(\lambda)T(\lambda)R(\lambda)\,. \tag{4.4}$$

where $B(\lambda)$ is the black body flux density at the effective temperature of the standard star. $T(\lambda)$ and $R(\lambda)$ will be the same for both object and standard, and therefore

$$S_{\text{source}}(\lambda) \approx \frac{S_{\text{obs}}(\lambda)}{S_{\text{standard}}(\lambda)} \times B(\lambda) \tag{4.5}$$

Calibrated spectra with the effects of atmospheric absorption removed were obtained by dividing the spectra by the spectrum of the standard star, then multiplying by the

blackbody flux of the standard at each wavelength. The blackbody flux was calculated from knowledge of the spectral type of the star (i.e. its effective temperature) and of its magnitude in the J passband. The temperature of the star defines its blackbody shape, the J magnitude the absolute flux level.

4.4 PG_1C: Particulars of Observations and Data Reduction

Observations of PG_1C were made in service time on the nights of the 8th and 14th January 1992. Seeing on the 8th was poor (3" or worse), but was good on the 14th ($\sim$ 1"). The data were oversampled with 4 integrations over 2 pixels, and exposures were of 15 seconds. 44 observations were obtained on the 8th (22 in each nod position) and 92 observations on the 14th, giving 68 minutes each of object and sky. After adding the spectra from both the positive and negative beams this gave a total of 136 minutes. The position of the slit on the field PG_1 is indicated in Figure 4.1. The slit orientation was 24.9° West of North.

During the data reduction, pronounced stripes along the spectral direction were found in the object-sky reduced groups. These stripes were a consequence of fluctuations in the dark current causing DC shifts in the sky level from integration to integration. The fluctuation between two consecutive 20 second darks was typically from 3-4 e^-/second to 15-20 e^-/second. It is believed that these shifts were associated with the contamination of the array, and were smaller versions of the glitches observed in the IRCAM data (described in Chapter 3). Using the mean of the signal in the upper and lower unilluminated areas of the slit to establish the DC level for each integration, it was possible to minimise the effect of the fluctuations by adding or subtracting the appropriate DC shift to each integration before they were combined (Ramsay S.K., personal communication). When used on a dark, this method reduced the read noise by a factor of two.

4.5 PG_3C: Particulars of Observations and Data Reduction

PG_3C was observed by the service team on the night of the 19th January 1993. Seeing was good, and exposures were of 20 seconds using 4/2 sampling. 46 observations were made, which after combining the spectra from both nod positions gave a total of 62 minutes of integration on the object. The slit orientation was 87.8° West of North, placing two reference objects along the length of the slit (see Figure 4.1). The data were reduced by the UKIRT service team.

4.6 The Reduced Spectra and the Nature of the PG Candidates

The reduced spectrum of PG_3C is reproduced in Figure 4.2. No emission line was detected in the passband of U1, indeed the spectrum is consistent with a flux of zero across the entire wavelength coverage of the array. Similarly the spectrum of PG_1C shows no emission lines nor any continuum flux. In principle, there are several possible explanations for this inability to detect the candidate PGs. Perhaps the object integration times were too short, or the astrometry incorrect, or perhaps the candidates are not real but are instead spurious ghost images.

Firstly, consider the length of the integrations. In determining the desired integration times (Section 4.2) we assumed the sensitivity at 1.01μm to be a factor of 3 worse than the established value at 1.25μm. It is possible that the combination of the fall off in quantum efficiency and the drop in the filter transmission reduces the sensitivity more strongly than this. Even over the wavelength range spanned in Figure 4.2, the increase in noise at short wavelengths is obvious.

To investigate this possibility an empirical determination of the sensitivity was made from the flux calibrated spectra of the candidates. Since no emission lines were detected, the standard deviation of the spectra over the wavelength covered by the narrowband filter U1 gives a good determination of the sensitivity. A sensitivity of 7.5×10^{-16} $\mathrm{Wm^{-2}\mu m^{-1}}$($3\sigma$, 30 minutes at 1.01$\mu$m) was found, i.e. 1.9×10^{-18} $\mathrm{Wm^{-2}}$ for unresolved lines. This a factor of 6 times worse than the 1.25μm value, or twice as bad as that

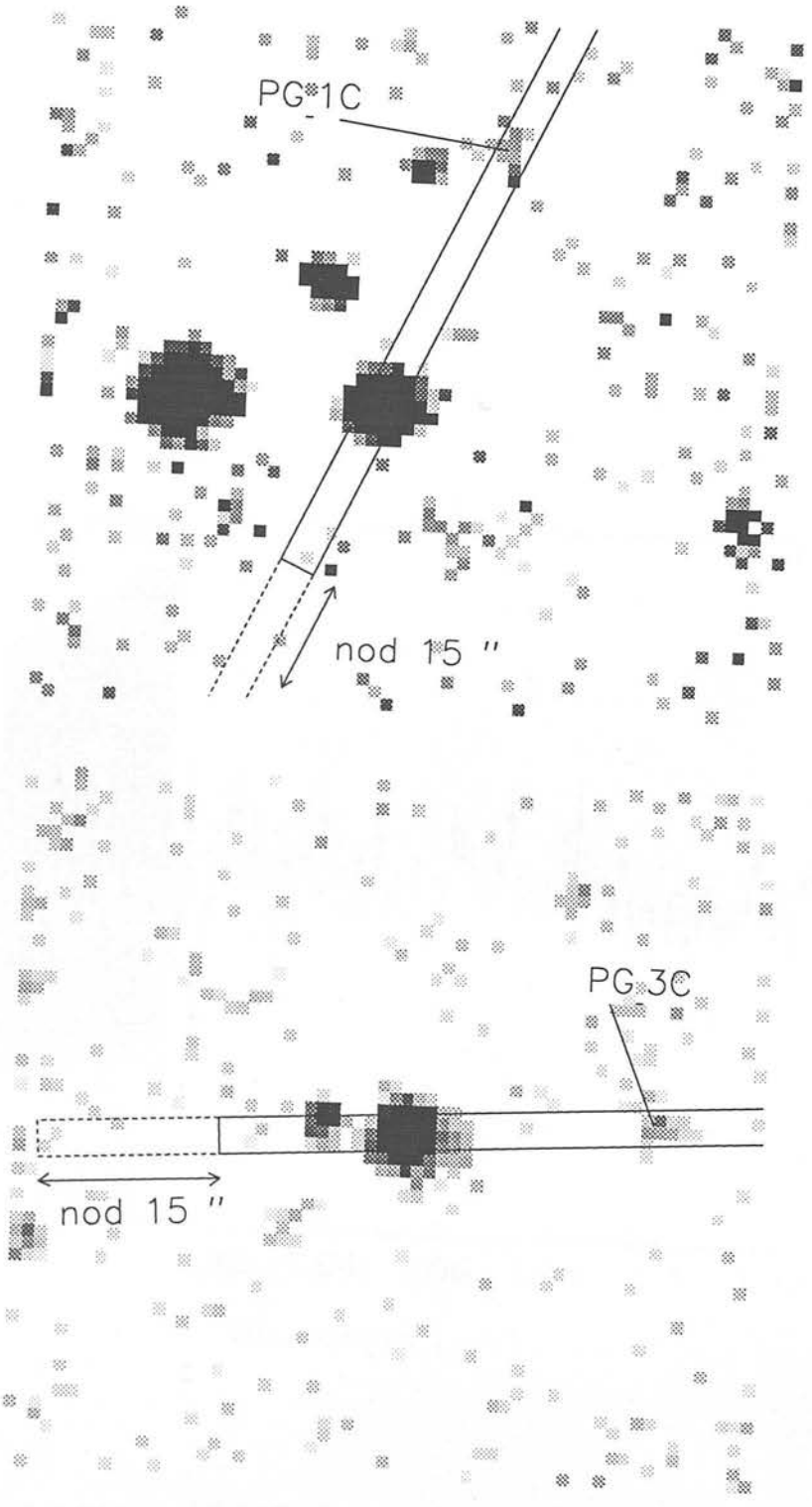

Figure 4.1: The position of the CGS4 slit for PG_1C (top) and PG_3C (bottom).

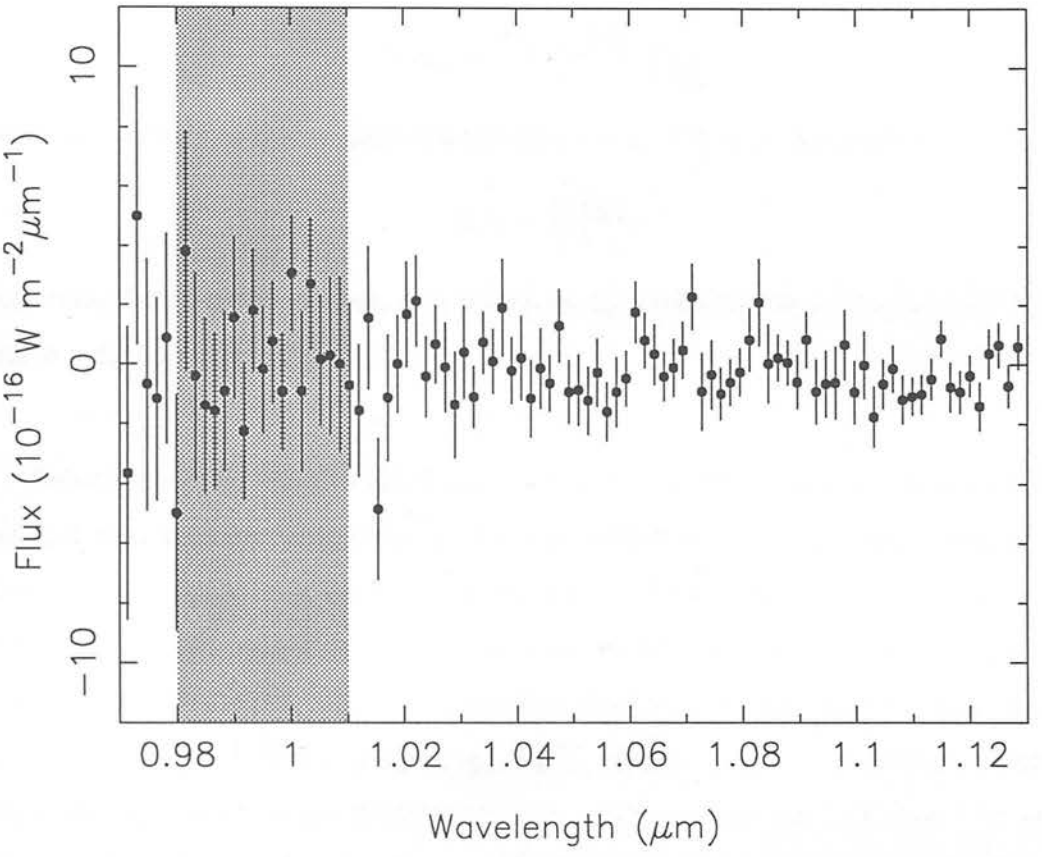

Figure 4.2: CGS4 spectrum of PG_3C. The shaded area represents the wavelength coverage of the narrowband filter U1 extended to cover the passband shift at 77K of up to 2%.

assumed for the calculations of integration times. The significance of any CGS4 detection would therefore be reduced by a factor of 2; if the IRCAM flux is distributed over a broad line width this makes it possible for the candidates to be undetected in the CGS4 integration times.

Using the revised value of sensitivity and the integration times in each field, the broadest line that could be detected at the 3σ level was calculated. Any line narrower than this limiting width would be detectable at greater significance, and the limiting width can be compared to the line width expected for a PG. For an integration time t, observed sensitivity S, and flux in the narrowband filter of $F_{\rm U1}$, Equations 4.1 and 4.2 give the maximum width $\Delta\lambda_{\rm line}$ for a 3σ detection of a line resolved by CGS4 as

$$\Delta\lambda_{\rm line} = \frac{F_{\rm U1} \times \Delta\lambda_{\rm R}}{S}\sqrt{\frac{t}{30}} \,. \tag{4.6}$$

This corresponds to a maximum emitted line width of $\Delta\lambda_{\rm e}$ in the restframe, where

$$\Delta\lambda_{\rm e} = \frac{\Delta\lambda_{\rm line}}{1+z} \,. \tag{4.7}$$

Assuming Doppler broadening, $\Delta\lambda_{\rm e}$ translates to a velocity dispersion $v_{\rm D}$ (half the line width velocity) at $z = 7.2$ of

$$v_{\rm D} = \frac{c\Delta\lambda_{\rm e}}{2\lambda_{\rm Ly}} \,. \tag{4.8}$$

Substituting the narrowband fluxes of PG_1C and PG_3C into equations 4.6 to 4.8 we find that velocity dispersions of less than 1400 kms^{-1} or 1200 kms^{-1} respectively would have resulted in a detection of significance 3σ or greater. Line widths greater than these are witnessed only in the most active galaxies, such as Type I Seyferts or QSOs. For comparison, velocity dispersions observed in high redshift radio galaxies are 400-1000 kms^{-1} (Eales & Rawlings 1993). A bona fide PG would have a velocity dispersion typical of normal galaxies which is much less than this, 300 kms^{-1} or so (see Chapter 2). The Lyα line for such an object would be just unresolved by CGS4 and would be easily detected, PG_1C at the 11σ level and PG_3C at 9σ.

Another possibility for the non detections is that the orientation or position of the slit was incorrect. In both fields however the reference object was detected at the expected pixel position and at the expected magnitude. This check confirms that there was no error in the astrometry of the observations. As both the astrometry is correct and the integration times adequate we are forced to conclude that the two candidates are either

active galaxies and therefore atypical of the general galaxy population or else are spurious ghost images. Either way, neither of the candidates match the definition of a primeval galaxy.

It was possible to make an empirical investigation into the failure to detect the object PG_1C by comparing the 1991 and 1992 IRCAM observations of the field. Between the two observing runs the narrowband filters had been removed from IRCAM and when replaced for the second run the filters had been rotated relative to their 1991 positions. If the candidate was a ghost then it is likely that this change in the optical arrangement of the instrument would cause a shift in the position of the ghost image, i.e. the candidate would be absent from its 1991 position. It was found that whereas a 16σ detection of the object was evident in the final mosaic of the 1991 data, there was no signal in the mosaic composed from just the 1992 data, despite achieving a depth which should have resulted in a 4σ detection. This suggests that PG_1C is indeed a ghost image. Although it was not possible to repeat this test for PG_3C, we strongly suspect that it is also a spurious ghost.

By the time of our 1992 run ghosting problems were resolved in broadband J, H, K by tilting the filters. It was not possible for us to tilt the narrowband filters in our IRCAM search since in tilting the filters the passbands would shift and the data from the two observing runs would therefore cover incompatible wavelengths. A new search could however make use of this technique, with the narrowbands chosen such that their passbands after cooling and tilting lay between the strongest OH^- lines.

4.7 Summary

The CGS4 integration times were easily adequate to detect a PG, being sufficiently long to detect any object with all but the most extreme line broadening seen in active galaxies. Neither of the 1.01 μm IRCAM candidates were however confirmed by the CGS4 spectroscopy. Subsequent investigation with IRCAM suggests that both the candidates are in fact a manifestation of the ghosting phenomenon. This means therefore that over an IRCAM search area of $3.0\Box'$ of sky no PG been detected down to a flux of $\approx 10^{-18}$ Wm^{-2}.

The limits that can be placed from the IRCAM search on the number density and

luminosity of PGs and the implications of this result on theories of galaxy formation are discussed in Chapter 5.

Chapter 5

Limits on Galaxy Formation at High Redshift

The IRCAM high redshift search revealed two objects showing characteristics expected for primeval galaxies. As described in Chapter 4, subsequent infrared spectroscopy failed to confirm either of the objects, suggesting that the objects are an artifact of the imaging system. Although the failure to detect a PG is disappointing, the limits on the number density and luminosity of any PG population placed by the depth and areal coverage of the search provide valuable information about any primeval galaxy population. In this chapter, the constraints on Lyα emission from a high redshift population ($7 \leq z \leq 10$) are considered. The effect that the presence of dust in young galaxies might have upon the results are discussed. By considering Hα emission from $0.5 \leq z \leq 0.9$ it is also possible to constrain star formation at intermediate redshifts. The constraints that can be placed on models of galaxy formation and evolution, and in particular on galaxy merger scenarios, are investigated.

5.1 Limits of the IRCAM Search

5.1.1 Limits in the Observed Frame

Plotted in Figure 5.1 are the limits that can be placed on the surface number density of primeval galaxies from the IRCAM search, as a function of observed flux in the filter. The limits exclude the area to the upper left of the plotted points: PGs with fainter observed fluxes or with lower number densities on the sky are not ruled out. Also indicated are the limits of the previous PG searches as described in Chapter 2. It can be seen that our search is reaching limits in the observed frame that are comparable to previous modern searches, even though our filters are at much longer wavelengths and hence are probing to much higher redshifts. Our restriction on areal coverage is principally due to the small field of view of IRCAM.

5.1.2 Limits in the Rest Frame

The limits in the observed frame can be used to constrain the comoving volume densities, rest frame luminosities and star formation rates of high redshift galaxies in the following manner.

Luminosity

The rest frame luminosity L is related to the observed flux l by

$$L = 4\pi d_L^2 l \,, \tag{5.1}$$

where $d_{\rm L}$ is the luminosity distance given in a Friedmann universe by

$$d_{\rm L} = \frac{c}{H_0 q_0^2}[z q_0 + (q_0 - 1)(-1 + \sqrt{2q_0 z + 1})] \,. \tag{5.2}$$

Conversion to Star Formation Rate

Hα emission is known to be a sensitive and direct tracer of star formation (Kennicutt et al., 1987). The star formation rate of an object can be estimated from its Hα luminosity using the conversion determined by Kennicutt (1983). It is also possible to convert Hα luminosity to Lyα luminosity, and hence to estimate the star formation rate needed to power the Lyα emission. This conversion assumes that the ultraviolet attenuation by

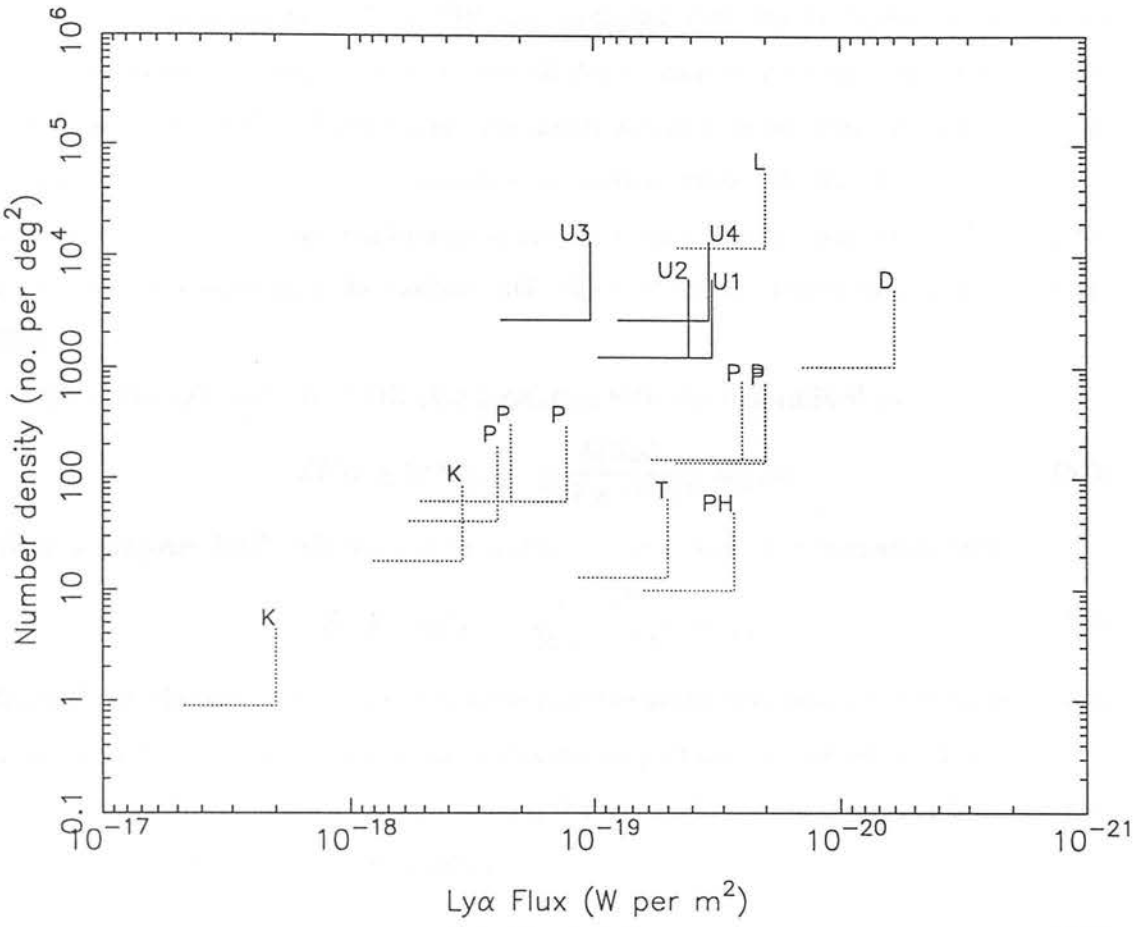

Figure 5.1: Limits on the surface number density of primeval galaxies as a function of observed flux in the filter. Limits are as follows. K: Koo & Kron (1980), PH: Pritchet & Hartwick (1990), L: Lowenthal et al. (1990), T: Thompson et al. (1993), D: Djorgovski & Thompson (1992), P: De Propris et al. (1993), U1-U4: our search. Flux limits are 1σ, and are for 1 " diameters. Density limits for our search are for 1 object in the central area covered by all mosaic positions, the coverage of all fields observed in each filter are combined. Flux limits for the IRCAM search are for the highest value for all the fields in that filter.

dust is negligible, and that the objects are optically thick to all Lyman lines — the latter is known as case-B recombination. PGs are expected to contain large amounts of HI gas and so for such objects case-B is a good approximation.

Kennicutt obtained Hα emission line fluxes from a large sample of elliptical and spiral field galaxies. The Hα luminosities were converted to Lyman continuum photon fluxes using the simple case-B recombination conversion determined by Brocklehurst (1971). Photoionisation models were then used to estimate the corresponding OB star formation rate and by assuming an IMF the OB star formation rate was extrapolated to give the total star formation rate, integrated over all stellar masses. Although the extrapolation is very sensitive to the adopted IMF, Kennicutt was able to constrain the IMF slope by combining the Hα photometry (sensitive to massive stars, 10-100 $M_\odot$) with U, B, V and R properties (the red continuum is mainly from low mass stars 0.7-3 $M_\odot$). Model galaxies were constructed for various IMF, the best fit was found to be for a Salpeter IMF.

The conversion of Hα to OB star formation rate was determined as

$$SFR(\geq 10\,M_\odot) = \frac{L(H\alpha)}{7.02 \times 10^{34} W}\,M_\odot/yr\,. \tag{5.3}$$

With a Salpeter IMF, this was extrapolated to give a total star formation rate

$$SFR(\text{total}) = \frac{L(H\alpha)}{1.12 \times 10^{34} W}\,M_\odot/yr\,. \tag{5.4}$$

If anything, this estimate of the SFR is too low; the above assumes case-B recombination, a small fraction of the Ly continuum radiation may in fact escape from the galaxy.

Again assuming case-B recombination, the Hα to Lyα conversion is given by (McCarthy et al. 1990, Brocklehurst 1971)

$$Ly\alpha/H\alpha = 8.74\,. \tag{5.5}$$

This gives approximately $\sim 10^{35}$ W in Lyα for each $M_\odot$/yr of star formation. Note that an IMF weighted towards the high mass end would be more efficient in generating Lyα photons.

Number Density

As well as considering flux sensitivity we must consider the volume covered by the search, i.e. the limits on the number density of objects. The comoving volume subtending 1

steradian is

$$dV = D^2 dr \,, \tag{5.6}$$

where D is the effective distance, which is given for a Friedmann cosmology by (Longair 1981)

$$D = \frac{c}{H_0 q_0^2} \frac{1}{(1+z)} [z q_0 + (q_0 - 1)(-1 + \sqrt{2q_0 z + 1})] \,. \tag{5.7}$$

Now from Einstein's field equations

$$\frac{dr}{dz} = \frac{c}{H_0} \frac{1}{(1+z)(2q_0 z + 1)^{1/2}} \,, \tag{5.8}$$

and so the volume element at any redshift in a Friedmann Cosmology is

$$dV = \frac{c}{H_0} \frac{1}{(1+z)(2q_0 z + 1)^{1/2}} D^2 dz \,. \tag{5.9}$$

The expected number in the volume element is $dN = dV\eta$, where η is the comoving number density of galaxies (See Chapter 3). Down to the appropriate luminosity limit, no objects were found in the volume searched by IRCAM. The probability that no objects were found given an expected number λ_g can be determined. Assuming that there is no significant clustering of objects, the galaxy distribution is well approximated by the Poisson distribution. Using Poisson statistics the probability of finding g galaxies when a model predicts an expectation value λ_g is given by

$$f(g) = \frac{(\lambda_g)^g e^{-\lambda_g}}{g!} \,. \tag{5.10}$$

In the case that no galaxies are detected, the probability that that model is correct is

$$f(0) = e^{-\lambda_g} \,. \tag{5.11}$$

This is also the probability that the expectation value is any value greater than or equal to λ_g. Expectation values greater than or equal to λ_g can be excluded with a confidence level of $1 - f(0)$.

5.2 Lyα Constraints at $7 \leq z \leq 10$

Using the framework outlined above, we can now consider the constraints on line emission from any appropriate redshift. The first emission line to consider is the Lyα line, redshifted into our filters for $7 \leq z \leq 10$.

5.2.1 Luminosity Constraints

Luminosity limits were obtained for each field of the IRCAM search and are given in Table 5.1. The limits are for 3 σ over 3 pixels, i.e. the brightest object that would escape detection. The limits tighten for higher values of H_0 ($L \propto H_0^2$) and worsen for low values of q_0. For $q_0 = 0.1$, the IRCAM limits are approximately a factor of four brighter than for $q_0 = 0.5$. Photometric calibration is accurate to 6% (see Chapter 3); a much greater source of uncertainty in the luminosity limits will arise from a lack of knowledge of the extent of PGs. If the objects cover more than the 3 pixel (4.3□") detection criteria then the luminosity limits of Table 5.1 will be brighter, with the limit on the total brightness for an object extending over n pixels increasing in proportion to $\sqrt{n/3}$. Predictions for the extent of PGs at the redshifts sampled by the IRCAM filters range from 1" to 10" or so. The models of Meier (1976) have 3/4 light diameters of $\sim$ 0.8 to 5".

Let us compare our limits on Lyα luminosity with those obtained by previous searches. Figure 5.2 shows the redshift coverage of each search as a function of Lyα luminosity. To simplify comparisons between individual searches, the luminosity limits have been normalised to a 1 σ detection of a 1" object. It can be seen that our study extends the search for PGs to significantly higher redshifts than have previously been reached. Indicated on the right-hand axis of the figure is the star formation rate needed to power the Lyα luminosity, as described in Section 5.1.2.

As an estimate of the expected range of Lyα luminosity from a PG, an upper limit of the brightest PG predictions (10^{38} W, see Chapter 2) and a lower limit of the high end of SFR of normal disk galaxies (converted from 20 $M_\odot$/yr, Kennicutt (1983)) are indicated on Figure 5.2 by extended dot-dash lines. It can be seen that the IRCAM search is sensitive to a SFR of only a few times the value seen in local spirals. This sensitivity to star formation relies on PGs being unobscured by dust. The likelihood and effect of dust obscuration are discussed later in this chapter.

The power and uniqueness of the IRCAM search is that we are probing back to very early times in the age of the Universe: at a redshift of 7, an Einstein-de-Sitter Universe is only 4% of its present age. We have reached a flux sensitivity sufficient to detect an unobscured PG with Lyα luminosity of all but the faintest of predicted values.

Table 5.1: Limits on Lyα luminosities from the IRCAM search. Limits are for a 3σ 3 pixel detection. Limits quoted are for $H_0 = 50$ kms^{-1}Mpc^{-1} and scale as $1/h_{50}^2$ where $h_{50} = H_0/50$kms^{-1}Mpc^{-1}.

Field	Filter	z	Limiting Flux 10^{-19} Wm^{-2}	Luminosity Lyα $1/h_{50}^2 10^{37}$ W $q_0 = 0.5$	$q_0 = 0.1$
PG_1	U1	7.2	0.9	0.4	1.7
	U2	7.8	1.8	1.0	4.3
	U3	8.7	-	-	-
	U4	9.3	2.0	1.7	7.8
PG_2	U1	7.2	2.9	1.3	5.4
	U2	7.8	3.2	1.8	7.4
	U3	8.7	9.2	6.5	29.3
	U4	9.3	3.0	2.5	11.5
PG_3	U1	7.2	3.6	1.7	6.7
	U2	7.8	4.1	2.3	9.6
	U3	8.7	10.7	7.5	33.9
	U4	9.3	-	-	-

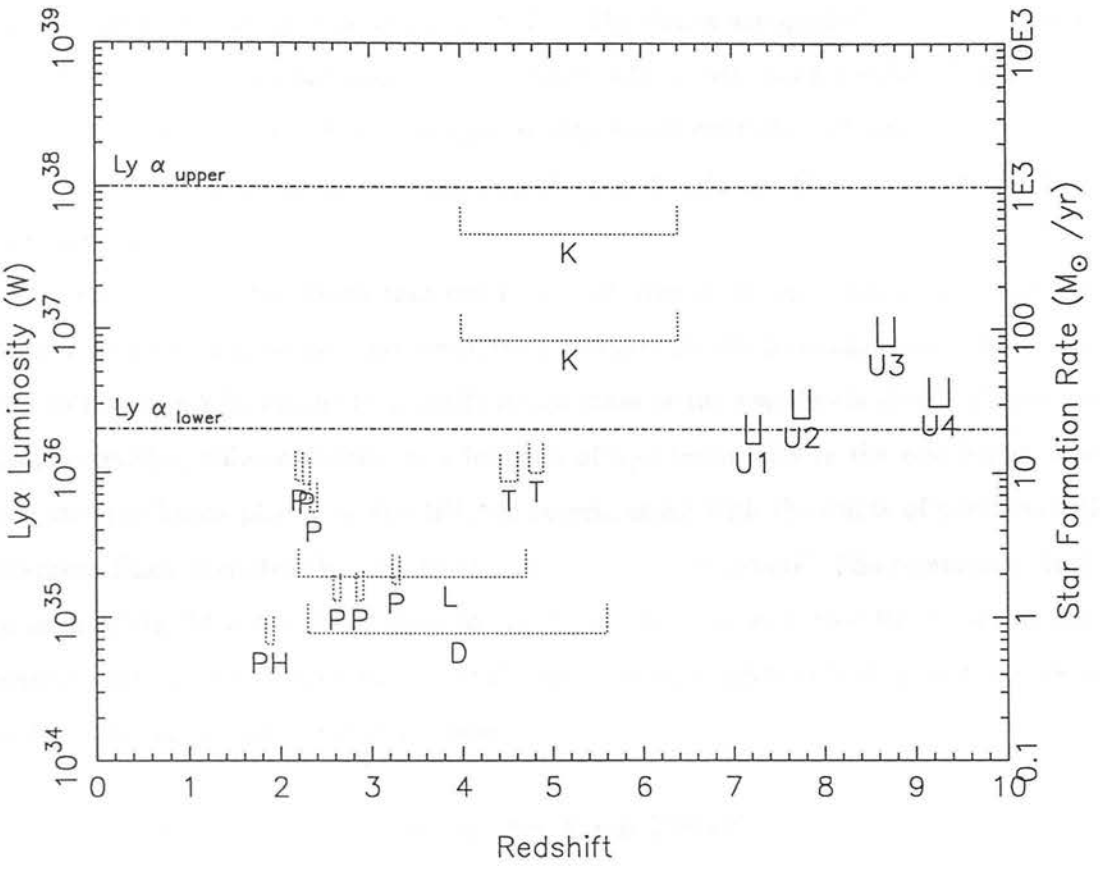

Figure 5.2: Redshift coverage of the IRCAM search and of previous primeval galaxy searches for Lyα emission. Abbreviations are as Figure 5.1. Luminosity limits are 1σ and for 1" diameters. The extended dot-dash lines represent the expected range for unobscured Lyα emission from a PG, see text for details.

5.2.2 Number Density Constraints

Constraints on the number density of emission line objects were calculated using the relations given in Section 5.1.2. Table 5.2 gives the constraints for various confidence levels for just one of the final mosaiced images, i.e. for one field over the range $z = z_U$ to $z_U + \Delta z$, and for the inner 1.0□' area of the mosaiced image which is covered by all offset positions (a total area of 2.0□' is covered by at least one frame in the mosaicing sequence of nine, but to a poorer flux limit). The limits are quoted for the U1 filter, though in fact the number density limits have only a very weak redshift dependence over the range $7.2 < z < 9.3$. Stronger density limits over the redshift range $z = z_U$ to $z_U + \Delta z$ can be obtained by combining the search volumes from each field for that particular filter.

Figure 5.3 shows the limits that can be placed from such combined data on the rest frame volume density of any Lyα emitters. The figure should be considered complementary to Figure 5.2 in which the redshift information of the searches is given. Figure 5.3 shows comoving volume density as a function of Lyα luminosity in the rest frame, and indicates the limits placed by the IRCAM search, along with the limits of previous PG searches. Each excludes the area to the upper left of the points. The luminosity limit for each of U1-U4 is the mean value for the fields observed with that filter, the volume density limits are for the central 1□' of the appropriate number of fields (i.e. three fields for U1, etc.) at the 68% confidence level.

5.2.3 No Evolution Predictions for Each Filter

It is important to obtain some quantitative feel for the number density constraints compared to the expected number density of PGs. Following the procedure of Baron & White (1987), we use the the observed local number density of galaxies to estimate the expected number of PGs. Assuming that there is no evolution in the number density of galaxies, this will be a good estimate. The number density of galaxies expected down to a luminosity $L_{\rm limit}$ is

$$\eta(L > L_{limit}) = \int_{L_{\rm limit}}^{\infty} \Phi(L) dL \,, \tag{5.12}$$

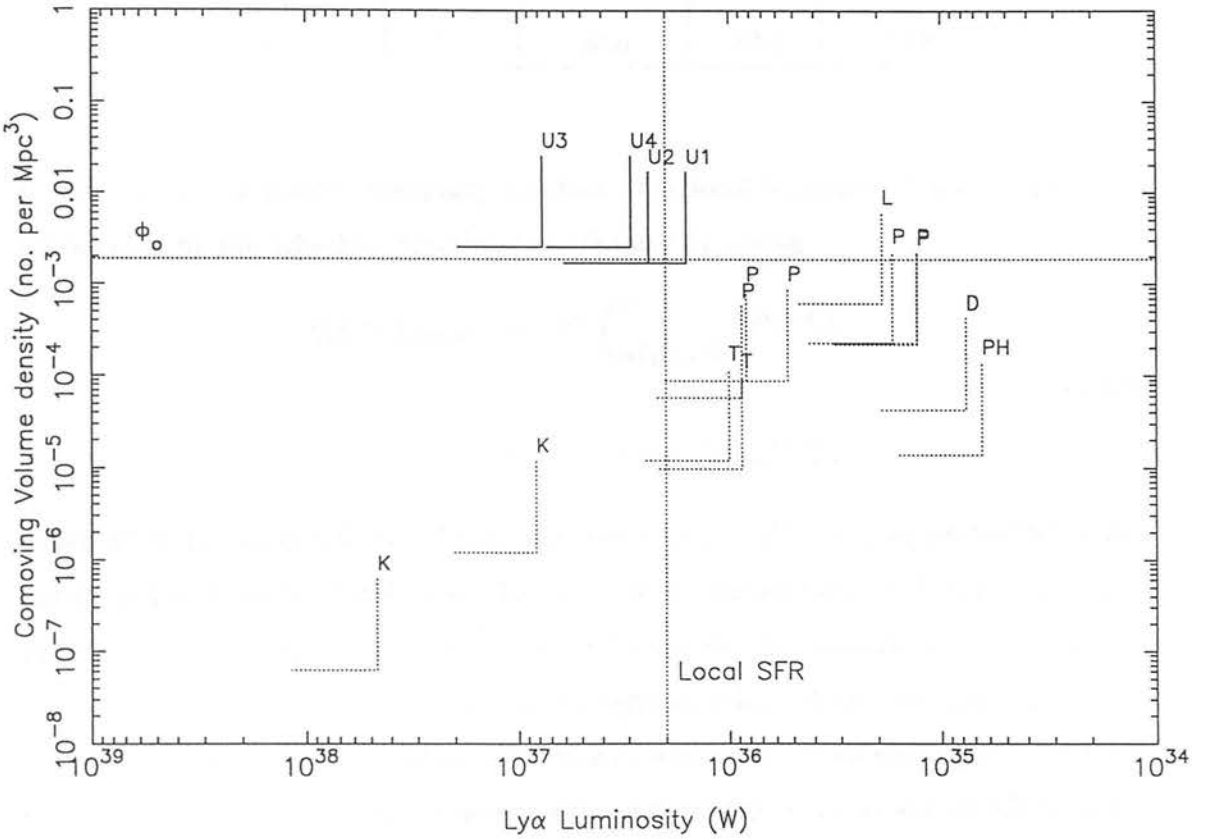

Figure 5.3: Limits on the comoving volume density of primeval galaxies as a function of Lyα luminosity. Abbreviations and limits are as Figure 5.2. The extended vertical dotted line indicates the high end of SFR of normal disk galaxies (Kennicutt 1983), the extended horizontal line the local number density of bright galaxies ($L_{\rm limit} \geq 0.3L^*$). $\Omega_0 = 1, H_0 = 50$ kms^{-1}Mpc^{-1}.

Table 5.2: Limits on volume density that can be placed from one field with filter U1.

Confidence level	Number Density (10^{-3} per Mpc^3)			
Cosmology	$H_0 = 50$kms^{-1}Mpc^{-1}		$H_0 = 75$kms^{-1}Mpc^{-1}	
	$q_0 = 0.1$	$q_0 = 0.5$	$q_0 = 0.1$	$q_0 = 0.5$
68%	0.8	5.8	2.6	19.7
80%	1.1	8.2	3.7	27.9
90%	1.6	11.7	5.3	39.8
95%	2.1	15.3	6.9	51.9
99%	3.2	23.5	10.6	79.8

where $\Phi(L)$ is the galaxy luminosity function. The local luminosity function Φ is well represented by the Schechter function (see Chapter 3), giving

$$\begin{aligned} \eta(L > L_{limit}) &= \Phi^* \int_{x=L_{limit}/L_*}^{\infty} x^\alpha e^{-x} dx \\ &= \Phi^* \Gamma(1+\alpha, L_{\rm limit}/L^*) \,, \end{aligned} \tag{5.13}$$

where Φ^* is the normalisation of the Schechter function, L^* is the characteristic luminosity, and α is the faint end slope. The incomplete gamma function $\Gamma(a, y)$ represents the fraction of Φ^* that is above the limiting luminosity. For positive a the Γ function can be calculated by means of either a series representation, which converges rapidly for $y < a+1$, or by means of a continued fraction development, which converges quickly for $y > a+1$ (Press et al. 1986). For non positive a the relation can be solved following an initial integration by parts.

Equation 5.13 gives the expected number density of objects for the simple case that the comoving number density of galaxies remains constant with redshift, at least out to the redshifts sampled by our filters. From this it is possible to gain an order of magnitude estimate of the number density of PGs by taking $\Gamma(1+\alpha, L_{\rm limit}/L^*) = 1.0$, i.e. $\eta(> L) = \Phi^*$. For the range of values estimated in the literature ($\alpha = -1.0$ to 1.25, Glazebrook 1991) the Γ function is unity for $L_{\rm limit}/L^* \approx 0.3$ — the dependence on the value of the faint end slope is weak. So the implicit assumption in this estimate is

that the characteristic luminosity of the search is approximately 3 times the detection limit. This is not an unreasonable assumption, as the expected Lyα for the brightest PG models is 10^{38}W, compared to our limits in the restframe of $\approx 10^{37}$W. For the case of no density evolution $\Phi^* = \Phi_0^*$, where $\Phi_0^* (= 1.9 \times 10^{-3} h_{50}^3$ Mpc$^{-3})$ is the local value. Taking $\Gamma = 1.0$ therefore gives us the order of magnitude estimate $\eta(> L) \sim \Phi_0^*$. The value of Φ_0^* is indicated in Figure 5.3. Although the Figure assumes $H_0 = 50$ kms^{-1}Mpc^{-1}, the strength of the number density constraint is independent of the value of H_0. The effect of a higher H_0 is to increase Φ_0 in proportion to H_0^3, but the volume density limits also increase in proportion to H_0^3. A lower Ω_0 tightens the volume density limits (see Table 5.2).

For a more precise estimate of the number density of PGs we must determine how far down the luminosity function our search is sensitive, i.e. the value of $L_{\rm limit}/L^*$. Taking $\alpha = -1.1$, the Schechter function was used to calculate the expected number of objects above the detection limit in each IRCAM frame for various values of L^*. Figures 5.4 and 5.5 show the expected numbers $N_{\rm T}$ at each sampled redshift, as a function of the characteristic luminosity of the galaxy population. It is clear that the effect of the adopted cosmology is considerable. At $L^*(\text{Ly}\alpha) = 1 \times 10^{38}$W the number predicted for an $H_0 = 50$ kms^{-1}Mpc^{-1}, $q_0 = 0.5$ universe and an $H_0 = 75$kms^{-1}Mpc^{-1}, $q_0 = 0.1$ universe differ typically by a factor of four.

The expected number of detections rises with increasing L^*. As the expected number rises, the fact that no PGs were detected becomes an increasingly unlikely event — the larger the value expected for $N_{\rm T}$, the higher the degree of confidence with which that value can be excluded. In quantitative terms, the confidence level C at which an expected number of PGs of N_T or more can be ruled out, given that none were detected, is

$$C = 1 - e^{-N_{\rm T}} \, . \tag{5.14}$$

$1 - C$ is the probability that the expected number is greater than or equal to $N_{\rm T}$. Figures 5.4 and 5.5 show the constraints on the number density that can be placed at 63%, 95% and 99% confidence levels. For example, the U1 data excludes at the 95% confidence level a population at $z = 7.3$ with $L^*(\text{Ly}\alpha) \geq 1 \times 10^{38}$W ($H_0 = 50$kms^{-1}Mpc^{-1}, $q_0 = 0.5$).

Of all the four filters, filter U1 has the highest predictions for the number of objects

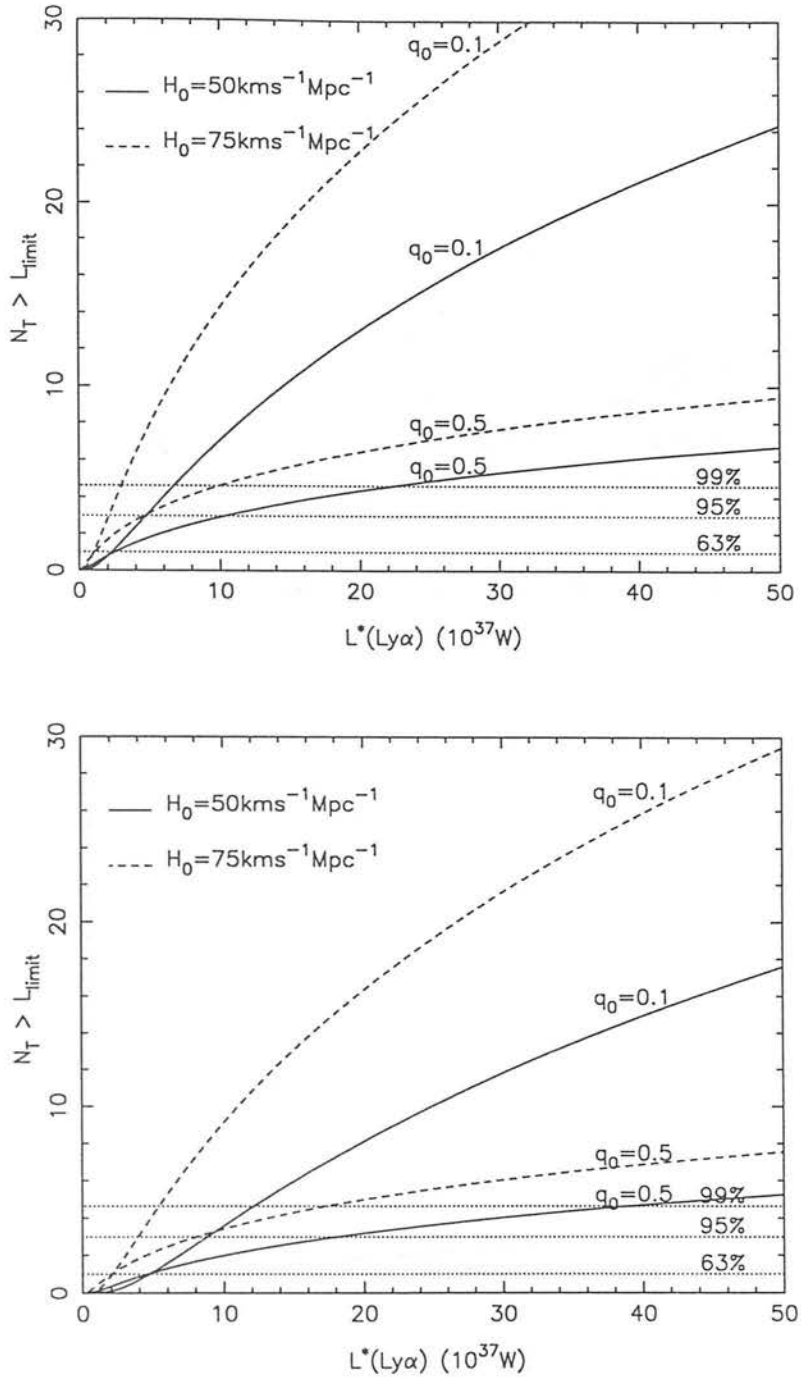

Figure 5.4: Number of objects N_T expected above detection limit in U1 (top) and U2 (bottom) as a function of characteristic Lyα luminosity of the galaxy population. The number is calculated from a Schechter function with $\alpha = -1.1$ and normalisation $\Phi^* = 1.9 \times 10^{-3} h_{50}^3 \mathrm{Mpc}^{-3}$ and for each filter is the sum of the number in each field. The horizontal dotted lines indicate the values of N_T above which numbers can be excluded at the indicated confidence level.

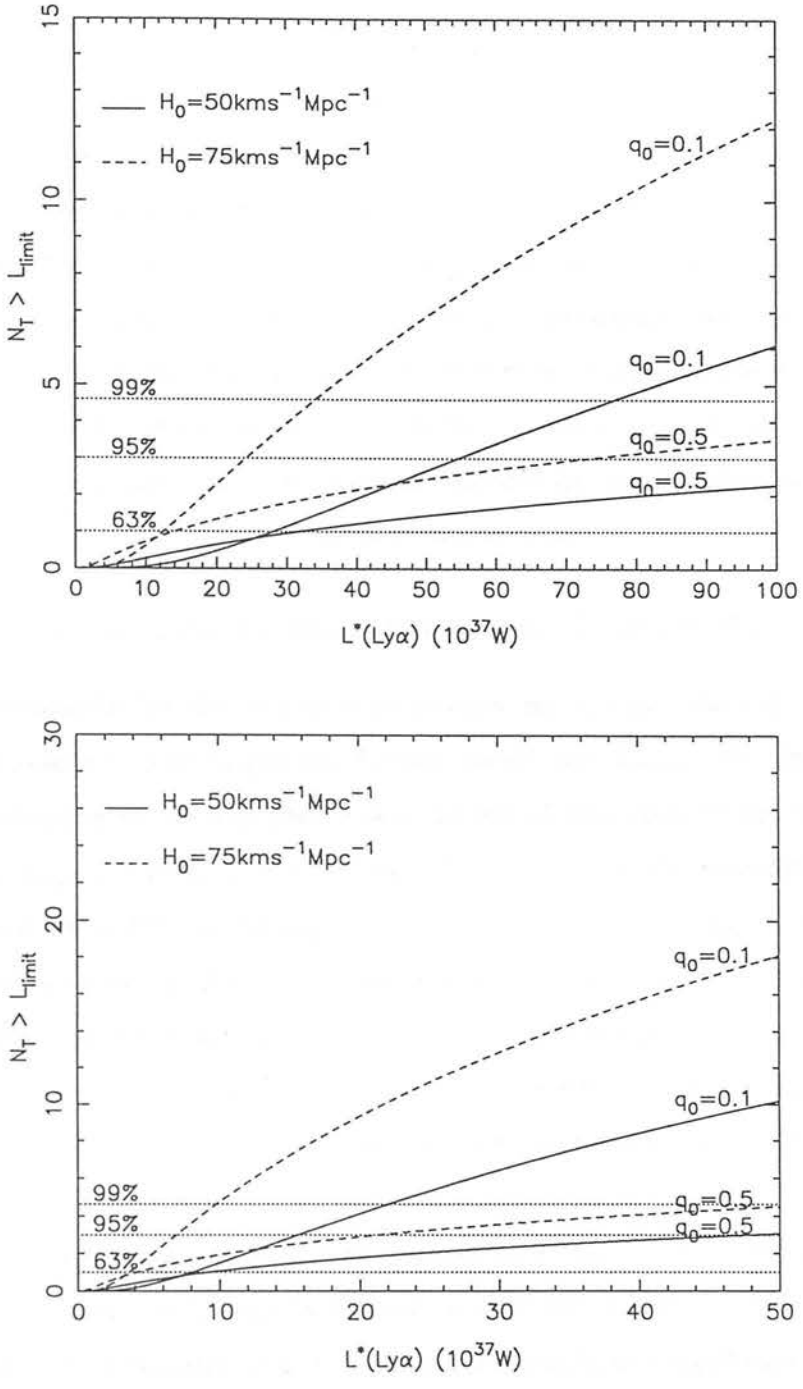

Figure 5.5: Number of objects N_T expected above detection limit in U3 (top) and U4 (bottom) as a function of characteristic Lyα luminosity of the galaxy population. The number is calculated from a Schechter function with $\alpha = -1.1$ and normalisation $\Phi^* = 1.9 \times 10^{-3} h_{50}^3 \mathrm{Mpc}^{-3}$ and for each filter is the sum of the number in each field. The horizontal dotted lines indicate the values of N_T above which numbers can be excluded at the indicated confidence level.

above the detection level. Even in this filter however, the failure to detect a PG constrains only the brightest of the PG models. The constraints may be further weakened if galaxies form over an extended timescale. So far in this analysis it has been assumed that the entire galaxy population is in its bright phase at the redshift of a particular filter. If galaxies form over an extended timescale, the number of objects in their luminous phase in any given filter will be reduced. However, if the epoch is extended then it will be sampled by more than one filter. The next section investigates the consequences of an extended epoch of galaxy formation, and finds that by combining the volumes sampled by each filter, in just the same way as the volumes sampled by each field were combined, it is possible to constrain the predictions for extended galaxy formation to a degree equal to or even stronger than the constraints obtained so far.

5.2.4 Constraints for an Extended Epoch of Galaxy Formation

Two key timescales for the formation of galaxies are $\Delta t_{\rm bright}$, the time over which an individual galaxy is in its bright star forming phase, and $\Delta t_{\rm epoch}$, the time between the start of formation of the first galaxy and the end of formation of the last galaxy. By definition, $\Delta t_{\rm epoch} \geq \Delta t_{\rm bright}$. Even though the timescale for the formation of individual galaxies may be as little as $\Delta t_{\rm bright} = 10^7$ years, most models of galaxy formation have the formation epoch lasting over a much more extended period, $\Delta t_{\rm epoch} \sim 10^8$ years (Partridge & Peebles 1966). If galaxies are forming throughout the epoch spanned by the four filters, then since each filter samples a discrete volume in redshift space it is possible to combine the volumes sampled by each filter, significantly strengthening our constraints.

This condition does not require an unreasonable $\Delta t_{\rm epoch}$, even though the redshift separation between the highest and lowest redshift filters is $\Delta z \sim 2.1$. The reason for this is that at high redshifts even a small Δt corresponds to a significant Δz. The time-redshift relationship for an Einstein-de-Sitter Universe is plotted in Figure 5.6. Each of the two pairs of vertical lines bounds a time interval of $2{\times}10^8$ years. The time-redshift relationship is such that although a small Δt at low redshifts corresponds to only a small Δz_{low}, at high redshifts the same Δt now corresponds to a much larger Δz_{high}. If $\Delta t_{\rm epoch} \geq 1.6 \times 10^8 h_{50}^{-1} \Omega^{-1/2}$ years, then in an Einstein-de-Sitter universe a luminous phase that has turned on by the redshift of the U4 filter ($z = 9.3$) will remain bright

at least until the redshift of the U1 filter ($z = 7.2$). In the discussion that follows it is assumed that the epoch of galaxy formation is extended over the four filters, i.e. $\Delta t_{\rm epoch} \geq 1.6 \times 10^8 h_{50}^{-1} \Omega^{-1/2}$ years.

Two extremes for the period $\Delta t_{\rm bright}$ of the bright phase in individual galaxies should be considered. In **Case 1**, the bright phase for each galaxy is also extended over the redshift spanned by the four filters, i.e. $\Delta t_{\rm bright} \geq 1.6 \times 10^8 h_{50}^{-1} \Omega^{-1/2}$ years, so that all of the galaxies at any sampled redshift will be in their luminous phase. The models of Meier (1976), in which $\Delta t_{\rm bright} \sim 3 \times 10^8$ years, can be described by Case 1. In **Case 2**, the bright phase is short, with only a fraction of the galaxies in their bright phase at any given redshift. This has the effect of reducing the expected number of PGs in the summed volume by a factor $\Delta t_{\rm U1-U4}/\Delta t_{\rm bright}$. The model of Partridge & Peebles (1966) is described by Case 2.

Testing Case 1

For each characteristic luminosity, the expected number of PGs above the detection limit in the combined volume from all redshifts was obtained by simply summing the numbers expected in each filter. The results are shown in the top diagram of Figure 5.7. Note that it has been assumed that the energy of the PGs is emitted uniformly throughout the epoch, i.e. that the characteristic Lyα luminosity remains constant.

It is clear from Figure 5.7 that in the case of a long $\Delta t_{\rm bright}$, it is possible to place much stronger constraints on the characteristic Lyα luminosity of a PG population than the limits placed by just one filter. Table 5.3 gives, for various cosmologies, the value of $L^*({\rm Ly}\alpha)$ above which luminosities are now excluded at the 95% confidence level by our failure to detect a PG.

For Case 1 models, the PG energy budget is emitted over a timescale equal to or greater than that covered between the lowest and highest filters. The minimum value for the characteristic energy emitted in Lyα is given by

$$E^*_{\rm min}({\rm Ly})\alpha = L^*({\rm Ly}\alpha) \times \Delta t_{\rm U1-U4}\,, \tag{5.15}$$

where $\Delta t_{\rm U1-U4}$ is the proper time between U1 and U4. The limits on this minimum characteristic energy are given in Table 5.3, and are of the order of $E^*_{\rm min}({\rm Ly}\alpha) \sim 10^{53}$ J. For comparison the energy budget estimated for a PG in Chapter 2 was $E_{\rm total} \approx 10^{54}$J

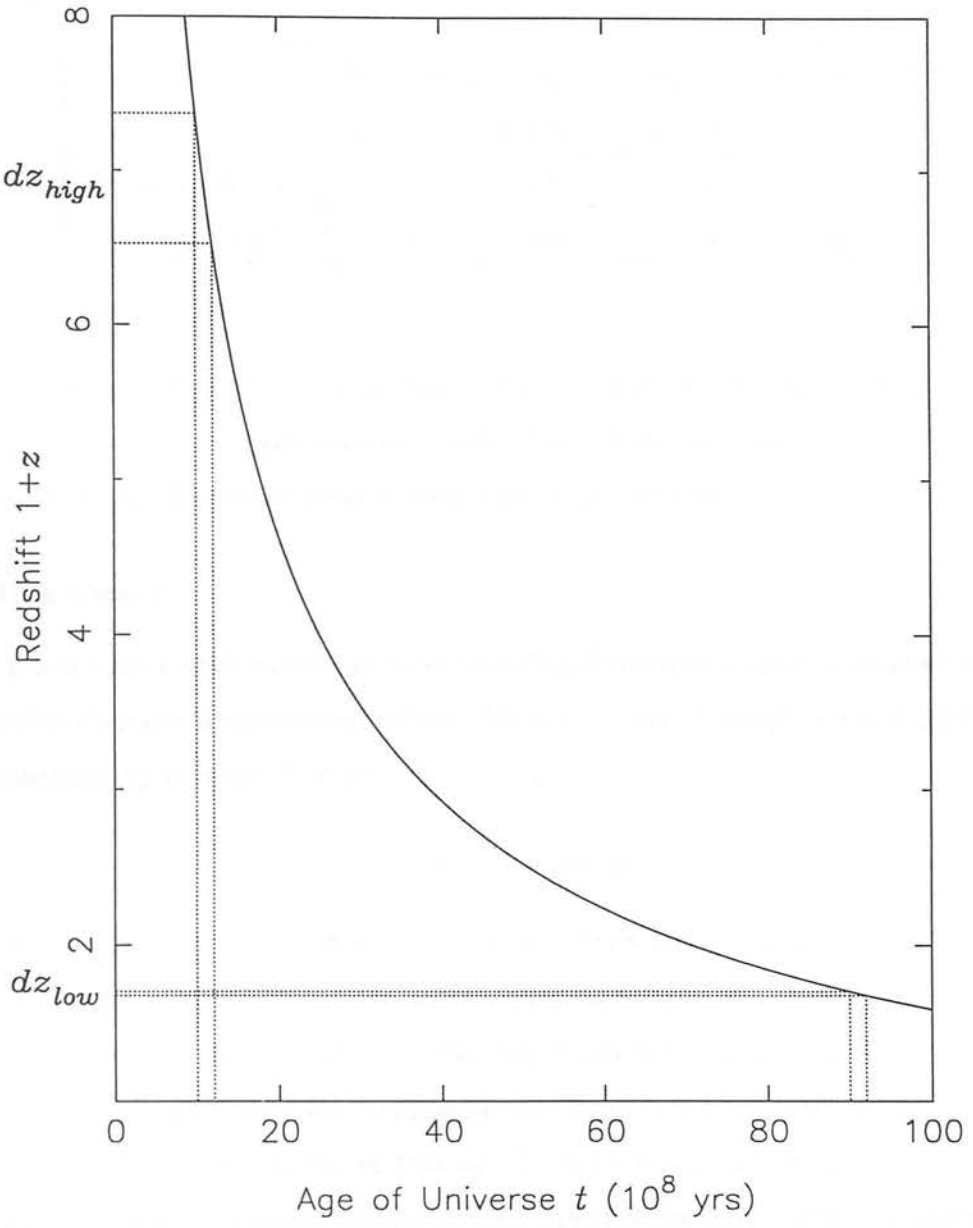

Figure 5.6: The $z - t$ relation for an Einstein-de-Sitter Universe: $(1 + z) \propto t^{-2/3}$. Each of the two pairs of vertical dotted lines bounds a time interval $\Delta t = 2 \times 10^8$ years.

Table 5.3: Limits on the characteristic Lyα luminosity of a PG galaxy population with luminosity function well described by the local Schechter function and with bright phase turning on by $z(U4)$ and remaining bright until $z(U1)$ (Case 1, see text).

	$H_0 = 50\text{kms}^{-1}\text{Mpc}^{-1}$		$H_0 = 75\text{kms}^{-1}\text{Mpc}^{-1}$	
	$q_0 = 0.1$	$q_0 = 0.5$	$q_0 = 0.1$	$q_0 = 0.5$
$L^*(\text{Ly}\alpha)$ 10^{37} W	3.8	4.2	1.6	1.9
$E^*_{\text{min}}(\text{Ly}\alpha)$ 10^{52} J	41.8	20.6	11.7	6.2

with a few percent of this being emitted in the Lyα line, i.e. $E^*(\text{Ly}\alpha) \sim 10^{53}$ J. Such an energy budget is consistent with our limits. For stricter constraints on the luminosity and energy of PGs, greater areal coverage would be required.

Testing Case 2

The predictions for the number of detectable PGs if the bright phase of galaxy formation is shorter than the time spanned between U4 and U1 was obtained by reducing the Case 1 predictions by a factor F where

$$F = \Delta t_{\text{U1-U4}} / \Delta t_{\text{bright}} \, . \tag{5.16}$$

For an estimate of Δt_{bright} we turn to the model of Partridge & Peebles (1966), this model predicts a high redshift of formation and so is particularly relevant to our IRCAM search. In their model, the duration of the initial bright period is $\Delta t_{\text{bright}} = 3 \times 10^7$ years. The characteristic luminosity of the PG is estimated as $L^* = 3 \times 10^{39}$ ergs, with 6-7% of the total luminosity being emitted in Lyα i.e. $L^*(\text{Ly}\alpha) = 2 \times 10^{38}$ W and, as assumed in this analysis, their comoving number density matches the local value. For their model we get

$$F = \frac{1.6 \times 10^8 h_{50}^{-1} \Omega^{-1/2}}{3 \times 10^7} = 5.3 h_{50}^{-1} \Omega^{-1/2} \, . \tag{5.17}$$

The total expected number of PGs for such a Case 2 model are given the bottom diagram in Figure 5.7.

The Partridge & Peebles model predicts a characteristic Lyα luminosity of $L^*(\text{Ly}\alpha) = 2 \times 10^{38}$ W, at the high end of the predictions for Lyα emission discussed in Chapter 2

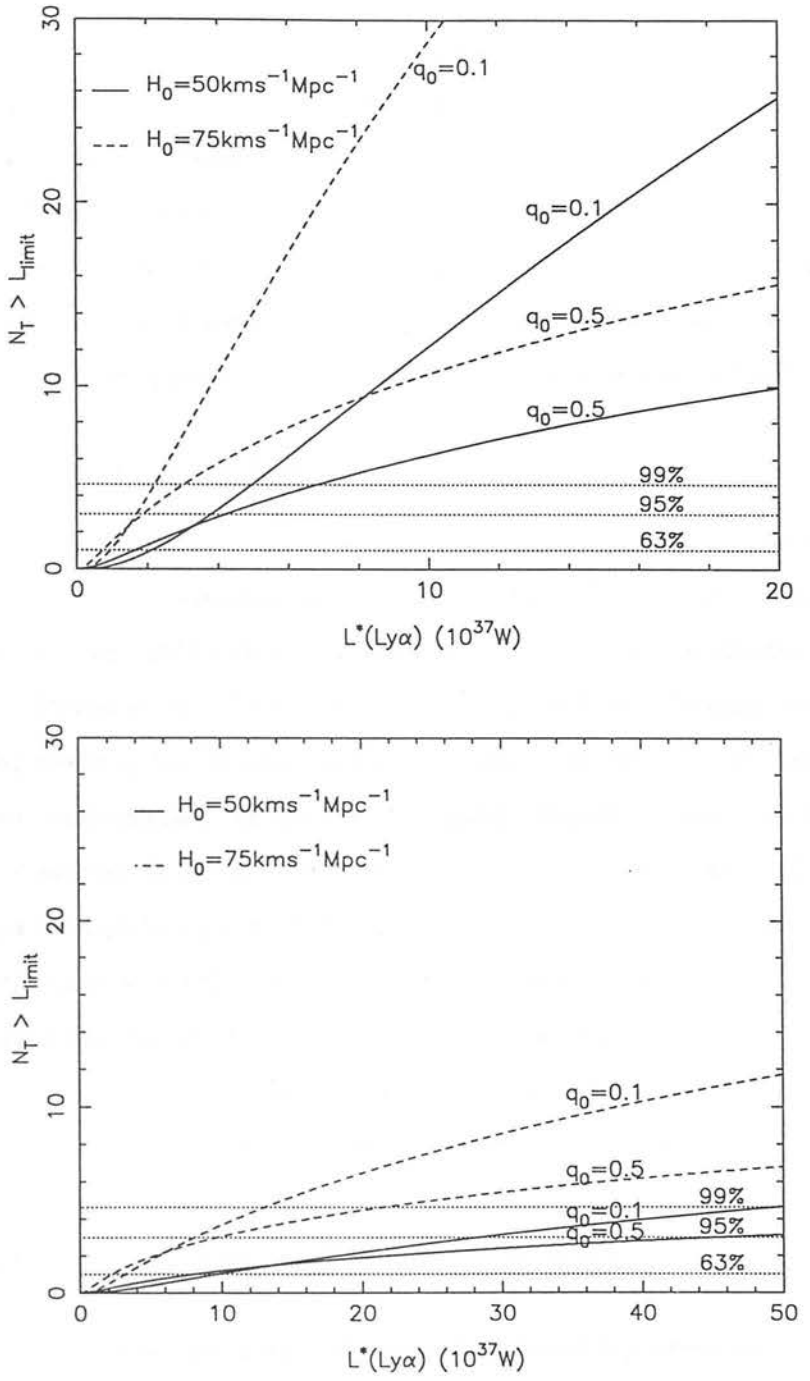

Figure 5.7: Number of objects N_T expected above detection limit in the combined volume sampled by all filters as a function of characteristic Lyα luminosity of the galaxy population, for Case 1 (top) and Case 2 (bottom), see text. The number is calculated from a Schechter function with $\alpha = -1.1$ and normalisation $\Phi^* = 1.9 \times 10^{-3} h_{50}^3 \mathrm{Mpc}^{-3}$ and is the sum of the number expected in each filter. The horizontal dotted lines indicate the values of N_T above which numbers can be excluded at the indicated confidence level.

since the energy is emitted over a comparatively short timescale. It can be seen from Figure 5.7 that for low H_0 such luminosities are easily consistent with our limits . Greater areal coverage would be required to tighten the constraints. For H_0=75kms^{-1}Mpc^{-1} however, luminosities greater than $L^*(\mathrm{Ly}\alpha) \sim 1 \times 10^{38}$ W can be excluded at the 95% confidence level for all values of q_0. The high H_0 constraints have several possible interpretations. It may be that the intrinsic Lyα luminosity is less than the Partridge & Peebles prediction, or perhaps the number density of PGs less than the no evolution prediction. Another possibility is that the Lyα is being attenuated by dust.

5.2.5 Attenuation by Dust

In all of these calculations it has been assumed that there is no attenuation of the Lyα emission by dust. Lyα emission is attenuated when the dust-to-gas ratio exceeds 1-10% of the value of the Milky Way (Charlot & Fall 1993). This possibility is discussed in Chapter 2. Provided the PGs are observed early in their star forming history, before the interstellar medium has become enriched by heavy elements ($\sim 10^7$ years), their Lyα line will be unattenuated. In the Case 1 scenario discussed above, the bright period is an order of magnitude greater than this value. It is therefore possible that there will be severe Lyα attenuation, particularly in the objects sampled by the lower redshift filters. If this is the case, searches covering a significantly greater area should be made with the hope of detecting the PG phase before dust obscuration reaches significant levels. In Case 2, the PG bright phase lasts only 3×10^7 years. Provided that there is no mixing of intergalactic material, then the effect of dust should be minimal.

5.3 Hα Constraints at $0.52 \leq z \leq 0.90$

In addition to constraining the population of high redshift primeval galaxies by the limits on Lyα emission, we can also consider the sensitivity of our search to other emission lines indicative of star formation. Emission lines observed routinely in active galaxies include Hα, [OII]3727 $\AA$, [OIII]5007 $\AA$, [CIV]1549 $\AA$, [CIII]1909 $\AA$ and [MgII]2799 $\AA$ (Glazebrook 1991). Given in Table 5.4 are the corresponding redshifts that place would place these lines in our narrowband filters.

Of particular interest is the investigation of the star formation rate at redshifts of

Table 5.4: Source redshift to place emission lines routinely observed in active galaxies in one of our narrowband filters. 1% cooling shift assumed.

Line	Emission Wavelength Å	Redshift Range
Hα	6563	0.52-0.90
OII	3727	1.68-2.35
OIII	5007	1.00-1.49
CIV	1549	5.46-7.05
CIII	1909	4.24-5.53
MGII	2799	2.57-3.45

$z \leq 1$. This interest stems from the interpretation of the excess of faint blue counts over the no-evolution prediction (see Chapter 2) in terms of a star bursting population at these redshifts. Of the emission lines mentioned in Table 5.4, the best indicator of the SFR is the Hα line, since this can be directly linked to the number of hot stars (Section 5.1.2). It is providential that at the wavelengths of our filters, the Hα samples redshifts of $0.52 \leq z \leq 0.90$, which are of particular interest in the interpretation of the faint blue count excess. Before examining the constraints that can be put on the low z star formation rate by the Hα limits, let us first recall the discussion of the faint counts given in Chapter 2, and consider the nature of the faint counts in more detail.

5.3.1 The Faint Blue Galaxies

The general explanation for the faint count excess is that at least some subset of galaxies were more luminous in the past. The simplest model is that of luminosity brightening in a strong initial burst of star formation at some redshift z_f, with no subsequent star formation at later times. This model can explain both the B excess and the observation that the K counts show far less excess over the non-evolving prediction (Lilly et al. 1991). Since the redshift distribution of the faint blue galaxies has been found closely to match the shape of the no-evolution prediction, a high redshift of formation ($z_f > 5$) is required so that recent evolution is mild, yielding redshift distributions little different

from the no-evolution case. It also requires a low q_o to provide sufficient volume at high z for the large numbers of galaxies in the faint counts (Colless et al. 1993).

Such a model is however only marginally consistent with recent measured redshift distributions. The deep redshift survey of Colless et al. (1993) finds the fraction of b_J galaxies at $z > 0.7$ to be less than 2% at the 90% confidence level, and less than 4% at the 99% level. Colless et al. also find that the bluest of the faint galaxies have redshifts $z < 1$. This is contrary to the mild evolution models which strongly predict that these blue galaxies should have redshifts of $z > 1$. Colless et al. conclude that models of mild luminosity evolution are ruled out.

What other explanations are there for the faint blue galaxies? There are presently two main schools of thought. One possibility is that the faint blue excess is due to dwarf ellipticals (dE's) undergoing their initial starburst at $z \sim 1$ (Babul & Rees 1992). Babul & Rees adopt a fiducial SFR of $4\,M_\odot/\mathrm{yr}$ at $z = 0.21$ and a number density of $n \geq 0.03 h_{50}$ Mpc^{-3} for faint blue objects distributed out to $z \approx 1.5$. One success of Babul and Rees's model is that it can explain the weak clustering observed in faint blue galaxies as compared to that expected from the clustering of local galaxies (Efstathiou et al. 1991) simply by making the evolution of the dwarfs be strongly influenced by the local IGM, with only those dEs in high pressure environments (i.e. in clusters), where the external medium can inhibit the mass outflow, being preserved to the present day. In the Babul & Rees model, those dE's in low pressure environments fade away to become virtually undetectable today, explaining both the high clustering and low space density of the present epoch dE's compared to the faint blue objects.

An alternative model is one in which the faint blue objects represent a gas rich merging population whose star formation rate decreases with cosmic time (Broadhurst et al. 1992). In this model the star formation rate evolves with look-back time t as

$$\Psi(t) = \Psi_0 \exp(bt/\beta t_0) \,, \tag{5.18}$$

where (see Peacock 1987)

$$\beta = 1 + (2q_0)^{0.6}/2 \,. \tag{5.19}$$

Ψ is the mean star formation rate per unit mass, and the parameter b defines the rate of evolution. Present day values are denoted with the subscript $_0$.

A merging model can satisfy both the B and K counts, since an evolving star formation rate affects the luminosity of a galaxy differently at short wavelengths than at long wavelengths. At moderate redshifts the B light from a galaxy is from the rest frame UV, where the dominant contribution is from hot O and B stars. Because these massive stars are short lived, their collective light is effectually an instantaneous measure of the star formation rate, and so counts in the B band are highly sensitive to an evolving star formation rate. At longer wavelengths on the other hand, the dominant contribution is from old, evolved stars, any on going star formation will therefore have little effect on the K band light. An evolving SFR can boost the faint B counts over the no-evolution model whilst leaving the K counts close to the no-evolution prediction.

A model based solely on an evolving SFR would predict that the faint B excess is from a luminous high redshift population. To match the observed redshift distribution, the Broadhurst model proposes that in addition to an evolving star formation rate, galaxies underwent substantial merging over recent look back times. This can reproduce both the number-magnitude relations and the observed redshift distributions of the faint counts. The model is parameterised in the following manner. The characteristic galaxy mass M^* decreases with increasing look back time t at the expense of an increase in number density Φ^*.

$$M^*(t) = f(t)^{-1} M_0^* \,, \tag{5.20}$$

similarly

$$\Phi^*(t) = f(\ t)\Phi_0^* \,, \tag{5.21}$$

where

$$f(t) = \exp(Qt/\beta t_0) \,, \tag{5.22}$$

and as before

$$\beta = 1 + (2q_0)^{0.6}/2 \,. \tag{5.23}$$

The parameter Q defines the merger rate. Since (Peacock 1987)

$$\frac{t}{t_0} = (1 - (1+z)^{-\beta}) \,, \tag{5.24}$$

these relations allow us to calculate the number density, characteristic mass and star formation rate as a function of redshift as predicted by the model.

The merger model predicts that at high redshift there are more galaxies per comoving unit volume. In the K band the luminosity per unit mass is constant and so if a galaxy is less massive it is less luminous. It is therefore possible (Broadhurst et al. 1992) to reproduce the near match between the K counts and the non-evolving prediction. In the B band on the other hand an increase in SFR per unit mass with redshift keeps the B luminosity of galaxies effectively constant. Combined with the increase in number density this results in the excess of counts over the no-evolution prediction.

A property of this model is the ability to constrain the values of b and Q fairly independently, b from the number counts and Q from the redshift data. Broadhurst et al. obtain a best fit of $Q = 4$ and $b = 4$. They suggest that the similarity in the rates of evolution in both the number density and SFR indicates that the increase in the star formation rate is associated in some way with the merging process.

Unlike the dwarf elliptical scenario there is no obvious way in the merger scenario to reproduce the observed weak clustering at faint magnitudes. Indeed, strong clustering on small scales would be expected, though the size of this effect would depend on the timescale of the merger and on whether the increase in SFR occurs prior to or during the merger. Another conundrum is the existence of the disk structure of spirals; why was this not disturbed in the merger process? Nonetheless, recent high resolution (seeing of $0.5'' - 0.72''$) CFHT imaging of the faint B sample (Ellis 1993) has revealed that several of the faint blue objects can be resolved into separate peaks: these turn out to have the strongest [OII] emission, indicative of star formation. Perhaps this is evidence of merging.

5.3.2 Rest Frame Limits

Let us now discuss the constraints on the star formation at $0.5 \leq z \leq 0.9$ that can be placed from the non detection of an emission line object in the IRCAM search. Limits on the line luminosities and comoving number densities of Hα emitters were calculated from the sensitivity limits given in Chapter 3, using the relations given in Section 5.1.2. Limits on the SFR of objects at the redshift of the filter were then established by means of the $H\alpha$ to SFR conversion also described in Section 5.1.2. These limits are given in Table 5.5.

Figure 5.8 shows the limits on the SFR at the redshifts that would place Hα emission in our filters. From the redshift distribution of the faint B counts it can be seen that

Table 5.5: Limits on Hα emitters at the redshifts appropriate to the narrowband filters. Sampled volume is for the central area covered by all mosaic positions for one field at the appropriate redshift. 1% cooling shift assumed. Luminosity limit is for 3σ over 3 pixels and has been converted to total star formation rate using: $SFR(\text{total}) = L(\text{H}\alpha)/1.12 \times 10^{34}$W (Kennicutt 1983), see earlier text.

Filter	z	Volume (h_{50}^{-3} Mpc^3)		Field	Hα ($h_{50}^{-2} \times 10^{33}$W)		SFR (h_{50}^{-2} M$_\odot$/yr)	
		$q_0 = 0.1$	$q_0 = 0.5$		$q_0 = 0.1$	$q_0 = 0.5$	$q_0 = 0.1$	$q_0 = 0.5$
U1	0.52	55.7	38.6	PG_1	15.1	12.3	1.4	1.1
				PG_2	59.4	48.4	5.3	4.4
				PG_3	48.2	39.2	4.3	3.5
U2	0.62	73.2	47.8	PG_1	46.8	36.8	4.2	3.3
				PG_2	104	82.1	9.4	7.4
				PG_3	80.4	63.2	7.2	5.7
U3	0.79	106.7	63.4	PG_2	48.6	36.0	4.4	3.2
				PG_3	419.8	310	37.8	27.9
U4	0.90	128.6	72.3	PG_1	127	90.4	11.4	8.1
				PG_2	188	134	16.9	12.1

we are probing a population with redshifts just higher than that dominating the faint B counts (whose median redshift $z = 0.21$). This is the first time that the star formation rate at these redshifts has been constrained.

As with the higher redshift Lyα limits, the failure to detect an emission line object in the volume sampled by the search can be used to place constraints on the number density, down to the detection limit, of emission line objects at various significance levels. These are given in Table 5.6 at the 63%, 90%, and 95% confidence levels. Two limits are given for each filter; that corresponding to the deepest frame (tightest SFR constraint) and that obtained from combining the volume coverage of all the fields in that filter with the limit on SFR derived from the shallowest frame in that filter (tightest number density constraint).

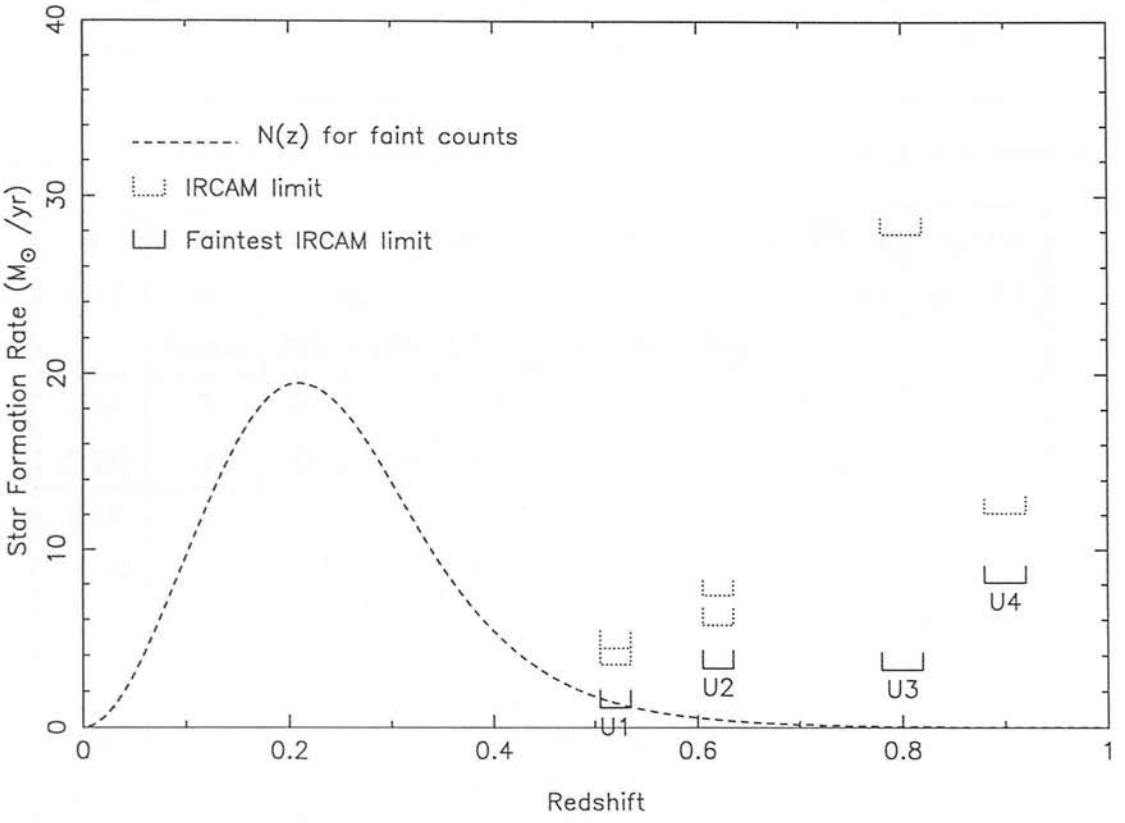

Figure 5.8: Limits on the star formation rate from Hα photometry. $H_0 = 50$ km s^{-1} Mpc^{-1}, $\Omega = 1$. SFR limits are for the brightest object that would fail to be detected i.e. for 3σ in three pixels. The faintest limit at each redshift is indicated by a solid line, additional volumes are covered to a higher flux limit, indicated for each field by a dotted line. Shown by a dotted line is the redshift distribution for the faint blue counts, limited at $b_J = 22.5$ (it is *not* an indicator of the SFR). The limits sample a population at redshifts just higher than that used to determine the parameters of the merger model.

Table 5.6: Limits on the number density of objects down to the given SFR. Sampled volume is for the central area covered by all mosaic positions for one field at the appropriate redshift. The strongest number density limit given is obtained by combining the volumes sampled by each field at that z, the strongest SFR limits are for the deepest field at that z. Confidence levels given are the probability that given zero objects detected in the given volume the number density is less than that given. 1% cooling shift assumed.

z	No	Number Density ($h_{50}^3 \times 10^{-3}$ Mpc^{-3})						SFR (h_{50}^{-2} M$_\odot$/yr)	
(dz)	of	$q_0 = 0.1$			$q_0 = 0.5$			$q_0 = 0.1$	$q_0 = 0.5$
	frames	63%	90%	95%	63%	90%	95%		
0.52	1	18.0	41.3	53.9	25.9	59.6	77.7	1.4	1.1
(0.03)	3	6.0	13.8	18.0	8.6	19.9	25.9	5.3	4.4
0.62	1	13.7	31.4	41.0	20.9	48.1	62.8	4.2	3.3
(0.03)	3	4.6	10.5	13.7	7.0	16.0	20.9	9.4	7.4
0.79	1	9.4	21.6	28.1	15.7	36.3	47.3	4.4	3.2
(0.04)	2	4.7	10.8	14.1	7.9	18.1	23.7	37.9	27.9
0.90	1	7.8	17.9	23.3	13.8	31.8	41.5	11.4	8.1
(0.04)	2	3.9	8.9	11.7	6.9	15.9	20.7	16.9	12.1

Table 5.7: Q=4.0 Broadhurst et al.model.

z	f		Φ_* $h_{50}^3 \times 10^{-3} Mpc^3$	
	$q_0 = 0.1$	$q_0 = 0.5$	$q_0 = 0.1$	$q_0 = 0.5$
0.52	3.74	3.47	7.01	6.50
0.62	4.34	3.95	8.14	7.40
0.79	5.37	4.73	10.1	8.86
0.90	6.02	5.20	11.3	9.75

5.3.3 Testing the Merger Model

Now let us apply the limits given in Table 5.6 to the merger model of Broadhurst et al. Although the model is based on data from redshifts slightly below those sampled by the narrowband filters, we can investigate whether an extension of the model to higher redshifts will fit the data at $0.5 \leq z \leq 0.9$. Using equations 5.21 – 5.24 and adopting the best fit to the redshift data ($Q = 4$), the predicted evolution f in the characteristic number density out to the redshifts sampled by the narrowband filters were calculated (see Table 5.7).

The resulting number densities are easily consistent with the constraints placed by the data at each redshift, $\Phi^* < 10 \times 10^{-3} h_{50}^3$ Mpc^{-3}. To tighten the number density constraints it is possible to combine the volumes sampled by each filter, since in this model the evolution of number density is smooth and the SFR (and hence Hα luminosity) per object remains approximately constant with look-back time. The predictions for the number of objects above the detection limit in each frame for this combined volume are shown in the top diagram of Figure 5.9. Characteristic star formation rates per object greater than or equal to $10\,M_\odot$/yr ($q_0 = 0.1$, $h_{50} = 1.0$), $12\,M_\odot$/yr ($q_0 = 0.5$, $h_{50} = 1.0$), $4.5\,M_\odot$/yr ($q_0 = 0.1$, $h_{50} = 1.5$) or $5.5\,M_\odot$/yr ($q_0 = 0.5$, $h_{50} = 1.5$) can be ruled out at the 95% confidence level. These are very powerful constraints, since the local SFR is typically $3 - 10\,M_\odot$/yr for normal spirals, rising to $20\,M_\odot$/yr in the more active spiral galaxies. For higher star formation rates to be accommodated, the number density normalisation Φ^* at the redshift of the $H\alpha$ line would need to be less than the

merging prediction. For example, the bottom diagram of Figure 5.9 shows the predicted number of Hα detections for the case of no density evolution. In this case, the 95% confidence limit on the SFR rises to $< 20\,M_\odot$/yr ($q_0 = 0.1$, $h_{50} = 1.5$) or $< 70\,M_\odot$/yr ($q_0 = 0.5$, $h_{50} = 1.0$). A SFR of several 10's of $M_\odot$/yr becomes compatible with the data.

If galaxy formation follows a merging scenario to $z = 0.9$, then the galaxies cannot be forming stars at a rate any greater than that observed locally. This is the first time that the star formation rate at these redshifts has been constrained.

5.4 Summary and Discussion

In this chapter it has been shown how the IRCAM search can be used to constrain, for the first time, the number density and Lyα luminosity of objects at redshifts of $7 \leq z \leq 9$, and the number density and Hα luminosity of objects at redshifts of $0.52 \leq z \leq 0.90$. Any model for the formation and evolution of galaxy formation must satisfy these new constraints.

By comparing the Lyα limits to predictions for the number of objects above the detection limit at each sampled redshift in the case of no density evolution, the limits in each filter can constrain a no-density-evolution model. For example, at the 95% confidence level the U1 data excludes a population with $L^* \geq 1 \times 10^{38}$W ($H_0 = 50$kms^{-1}Mpc^{-1}, $q_0 = 0.5$), or with $L^* \geq 2 \times 10^{37}$W ($H_0 = 75$kms^{-1}Mpc^{-1}, $q_0 = 0.1$).

By combining the volumes sampled at all the filter redshifts, a stronger test is provided for models in which galaxy formation extends over the time spanned by the four IRCAM filters ($\sim 10^8$ years). Two extremes for the bright phase $\Delta t_{\rm bright}$ of each galaxy are considered. In Case 1, $\Delta t_{\rm bright}$ spans the four filters. In Case 2, the bright period is much shorter. The specific case of the Partridge & Peebles (1966) model is considered, for which $\Delta t_{\rm bright} = 3 \times 10^7$ years.

The 95% confidence limits for Case 1 models constrain L^*(Lyα) to less than 1.6×10^{37}W -4.2×10^{37}W, depending on the cosmological model. These limits are consistent with the predictions for the Lyα luminosity from a PG. For stronger constraints to be made, greater areal coverage would be required. For the model of Partridge & Peebles (Case 2), the predicted PG luminosity is $L^*(\text{Ly}\alpha) = 2 \times 10^{38}$W. For high values of

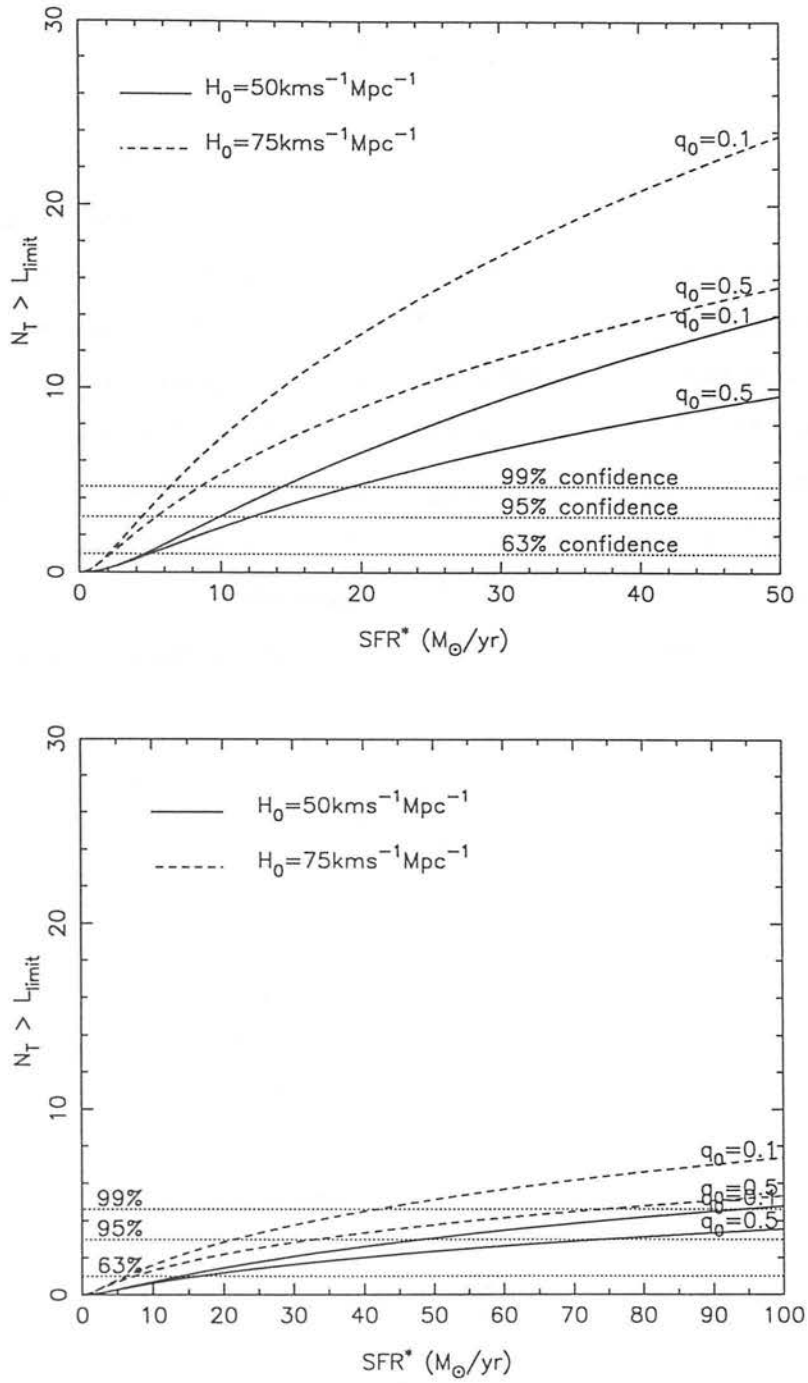

Figure 5.9: The total number of objects detectable in our fields via their Hα emission for characteristic star formation rate SFR^* as predicted by the favoured merger model, $Q = 4$ (top) and by the no-density-evolution model, Q=0 (bottom). SFR^* is assumed constant over the range in redshift sampled by the filters $0.5 \leq z \leq 0.9$. The horizontal lines indicate the values of N_T above which expected numbers can be excluded at the indicated confidence level. $\Phi_0^* = 1.9 \times 10^{-3} h_{50}^3 \mathrm{Mpc}^{-3}$, $\alpha = -1.1$.

H_0 this luminosity is inconsistent with the IRCAM limits; for $H_0 = 75\text{kms}^{-1}\text{Mpc}^{-1}$ luminosities greater than$\sim 1 \times 10^{38}$W are ruled out at the 95% confidence level. For low values of H_0 the predicted PG luminosity is consistent with the limits. The effects of dust would further weaken the constraints. For stronger constraints to be placed, greater areal coverage would need to be achieved.

The limits on Hα luminosity can be used to constrain the SFR at $0.52 \leq z \leq 0.9$. This can be used to constrain the merger model of Broadhurst et al. By combining the volumes of all filters the $Q = 4$ merger model (which gives the best fit to the faint galaxy redshift distribution) is found to be incompatible with a constant SFR of more than 4.5 -12.0 $\text{M}_\odot$/yr over $0.52 \leq z \leq 0.9$, depending on the cosmology. This is the first time that star formation has been constrained at these redshifts. The local SFR in normal spirals is typically 3-10 $\text{M}_\odot$/yr. If the merger model is followed to $z = 0.9$ then galaxies cannot be forming stars at any greater rate than that observed locally.

Chapter 6

Concluding Remarks and Future Prospects

The principal aim of the thesis was to discover a population of galaxies exhibiting the characteristics of a primeval galaxy population. All previous searches for such a population had failed, despite covering what should have easily been sufficient areal coverage and flux sensitivity. Previous searches have been constrained by the available technology to mainly optical wavelengths, covering redshifts $1.8 \leq z \leq 6$. Searches at these redshifts are supported by the predictions of CDM models, which predict the late formation of structure, at $z \sim 2$. However, there is substantial empirical evidence to suggest that at least the spheroid population formed earlier than this. For example, the high metallicities observed in quasars suggest significant ages even at redshifts of $z \sim 3$, indicating that at least some small-scale structure must have formed at high redshifts. Results from K selected studies of colour evolution of early type galaxies in clusters (Aragón-Salamanca et al. 1993) suggests that elliptical galaxy formation was coeval and at high redshift, $z > 2$, and most likely at $z > 5$.

The failure of the optical searches, combined with the empirical evidence for a high redshift of galaxy formation, led us therefore to search redshifts $z > 6$. The discovery of a PG population at such redshifts would have conspicuous consequences for CDM models.

Models of the spectral energy distribution of PGs predict very strong emission in Lyα, with the Lyα line having an equivalent width of $\sim 100\mathring{A}$. At $z > 6$ the Lyα line is shifted to infrared wavelengths. Our approach was to undertake deep IRCAM imaging

in the J window ($\sim 1.0 - 1.5\mu$m), using four narrowband filters of 2% FWHM. The filters covered Lyα emission from objects at $7.2 \leq z \leq 9.3$. We then made spectroscopic observations of any objects showing the characteristics of an emission line source.

No PGs were found to a sensitivity limit of $\approx 10^{-18}$ Wm^{-2} over an area of sky of 3.0□'. The programme therefore failed in its primary aim of detecting a PG population. However, the search does allow us to place the first limits on star formation at redshifts of $z > 6$. Any model of galaxy formation and evolution must satisfy these limits. For example, a model was tested in which it was assumed that there is no evolution in the comoving number density of galaxies out to $z = 9$, and that the luminosity function of objects at these redshifts can be represented by a Schechter function. Two cases were considered, one in which the bright phase of each galaxy spanned the four narrowband filters ($\sim 10^8$ years), and the Partridge & Peebles (1966) type case in which the bright period is much shorter ($\Delta t_{\rm bright} = 3 \times 10^7$ years). q_0 was assumed to lie in the range $0.1 \leq_0 \leq 0.5$. For the case of an extended bright phase lasting $\sim 10^8$ years, the limits are consistent with the appropriate predictions for Lyα luminosity ($1 \leq h_{50} \leq 1.5$). For the Partridge & Peebles case, the predicted luminosity for high H_0 is inconsistent with the IRCAM limits (h_{50}=1.5), but for low H_0 the prediction is consistent with the limits (h_{50}=1.5).

For those PG models that are excluded, various possibilities must be considered. The most obvious is that the intrinsic Lyα luminosity is less than that predicted, putting a detection below the sensitivity limit of our search. It is also conceivable that we are sampling the wrong redshift, and that galaxy formation occurs at even earlier times, $z > 9.2$. Later times, $2 \leq z \leq 6$, are ruled out by the optical searches.

There are however many other avenues to be explored. Perhaps PGs are dusty objects, with the dust severely attenuating the Lyα emission. It may be that objects at these high redshifts are strongly clustered and that the chosen fields happen to lie within in a void. This eventuality has been examined at low redshifts by searching for PGs around quasars (e.g. de Propris et al. 1993). At redshifts of $z \geq 5$ however, there are no known objects. Here the question of clustering can be addressed only by searching large areas of sky. Another possibility is that the bright phase of galaxy formation is very short ($< 10^7$ years), drastically reducing the number density of objects at any redshift.

CDM models, despite their shortcomings (see Chapter 2), still remain the benchmark

against which cosmological observations are tested. Let us therefore consider the implications of this, and previous, PG searches for CDM scenarios. In general, CDM models predict that a substantial fraction of the stars in bright galaxies formed at quite recent redshifts, $z < 5$, with galactic sized masses assembling recently, around $z \sim 2$. Baron & White (1987) made a detailed study of the appearance of PGs in a CDM scenario. Their model predicts that the bulk of star formation occurs over a much extended period, of order of the current age of the Universe, and lasting until $z \sim 1$. This star formation is not necessarily confined to the volume of the galaxy, but may be in individual subunits which subsequently merge. Baron & White type models predict a much lower Lyα luminosity in PGs than the Partridge & Peebles type model, which assumes the bulk of star formation to have occurred at high redshifts, i.e. over a comparatively short timescale. CDM models do not predict a large amount of star formation at the redshifts of our filters, any that there is is likely to be in subgalactic units of very low luminosity, well below the sensitivity of our IRCAM search.

As with our analysis, previous PG searches compare their limits to the expected number of PGs by assuming a Schechter shaped luminosity function and adopting a model of no number density evolution. Following the Baron & White predictions, these optical searches have assumed a much lower value for the characteristic luminosity ($L^*(Ly\alpha) \sim 1 \times 10^{36} h_{100}^{-2}$ W) than those tested by our PG search and predicted by models such as that of Partridge & Peebles ($L^*(Ly\alpha) \sim 1 \times 10^{38}$ W). These lower luminosities are excluded by the optical searches, but in general at only a marginal level. The presence of only a small amount of dust in young galaxies could explain the discrepancies. The amount of dust would have to be small enough so that the imprint left on the cosmic background radiation is below the current sensitivity to deviations on the CBR (see below).

If primeval galaxies are dusty, and the Lyα emission and UV continuum degraded to the rest frame far-infrared, then this would now be observable as an excess on the cosmic background radiation at sub-mm wavelengths. Djorgovski (1992) predicts the signature of a dusty PG population to lie at $\sim 0.1\%$ of the CMBR level. So far, measurements from the FIRAS instrument on COBE (Mather et al. 1990) have found the CMBR to have an excellent black body fit. The deviation from a blackbody is less than 1% of the peak intensity over the wavelength range 1cm to 0.5mm. Further analysis and additional

data are expected to improve the sensitivity to deviations from a black body spectrum by an order of magnitude. At this improved level we may hope to detect the background from dusty PGs. Another approach to finding dusty PGs would be to make searches at sub-mm wavelengths with ground based telescopes, for example using the bolometer array SCUBA ($350 - 450\mu$m and $750 - 850\mu$m) on the James Clark Maxwell Telescope.

Assuming no dust obscuration, if tighter constraints are to be placed on the characteristic luminosity of a high redshift PG population, it will be necessary to extend the infrared search to larger comoving volumes. Once a search area 3 times that of the IRCAM survey has been covered to a similar flux limit to the IRCAM survey, most dust free PG models would be severely constrained. For example, if no PGs were found, then Partridge & Peebles type models with $L^*(\mathrm{Ly})\alpha \geq 10^{38}$W would be ruled out at the 95% level ($h_{50} = 1$, $q_0 = 0.1 - 0.5$, for higher values of H_0 this constraint would be even tighter). As infrared arrays are becoming available covering larger and larger areas of sky, such searches will soon be possible (for example using the new 256×256 array on the William Herschel Telescope).

For CDM models to be rigorously tested, future PG searches must tighten the constraints on the characteristic luminosity at low redshift ($z \sim 2$) to allow for the possibility of a small percentage of absorption of Lyα by dust. This should be coupled with tighter constraints on the amount of dust obscuration from the shape of the CBR. For the infrared searches to reach the CDM predictions for star formation at high z, the sensitivity of these searches would have to be bettered by at least an order of magnitude.

Finally, an alternative, and exciting, technique yet to be explored in the quest for PGs is to exploit the gravitational lensing properties of rich clusters, which for unresolved objects results in an increase in the flux/pixel at the detector. The magnification provided by this gravitational telescope is a powerful tool for studying high redshift objects. Rather than relying on intrinsic, atypical properties of objects to make them visible, it then becomes possible to use the purely serendipitous quality that they lie on the extended line of sight between us and the cluster. Selection effects with this technique would therefore be minimal.

As well as being sensitive to Lyα emission at $z \sim 8$, this search is also sensitive to emission lines at lower redshifts, particularly $H\alpha$ emission at $0.5 \leq z \leq 0.9$. This line is recognised as a direct tracer of star formation (Kennicutt et al., 1987). Constraints

on the star formation rate at these redshifts are of great interest in the interpretation of the excess of faint blue objects seen in number counts (Tyson 1988, Lilly et al. 1991, Metcalfe et al. 1991, Jones et al., 1991). Originally conceived as a secondary avenue for investigation alongside the main Lyα search, the limits on Hα were found in fact to provide very powerful constraints on the SFR at $0.52 \leq z \leq 0.9$. These are the first constraints on star formation at these intermediate redshifts, and as with the Lyα limits, must be satisfied by any models of galaxy formation and evolution. For example, we considered the $Q = 4$ Broadhurst et al. (1992) merger model ($Q = 4$ gives the best fit to the faint galaxy redshift distribution). This model was found to be incompatible with a constant SFR of more than 4.5 -12.0 $M_\odot$/yr over $0.52 \leq z \leq 0.9$, depending on the cosmology. Compare this with the local SFR in normal spirals, which is typically 3-10 $M_\odot$/yr. If the merger model is followed to $z = 0.9$ then galaxies cannot be forming stars at any greater rate than that observed locally.

Do the Hα constraints have any implications for CDM models? Since CDM models predict the hierarchical growth of structure, they fit in well with merger models. Assuming that evolution in the number density of objects is described by the $Q = 4$ Broadhurst et al. merging model, the Hα limits constrain objects at $0.5 \leq z \leq 0.9$ to having star formation rates of less than $\sim 10\,M_\odot$/yr at the 95% confidence level ($h_{50} = 1$). Baron & White predict star formation rates of $20 - 120\,M_\odot$/yr ($h_{50} = 1$), but these are expected to drop off after $z \sim 1$. This is supported by our $H\alpha$ limits, which rule out such luminosities at $0.5 \leq z \leq 0.9$ at the 99% confidence level or better. Even if there is no merging, star formation rates of more than $70\,M_\odot$/yr at $0.5 \leq z \leq 0.9$ are excluded at the 95% level or better.

Appendix: Transmission Curves

This Appendix gives the transmission curves for the four narrow band filters U1, U2, U3, U4, and for the blocking filter WG 230. The curves are reproduced from scans provided the suppliers (see Chapter 2).

Transmission Curve for Filter U1

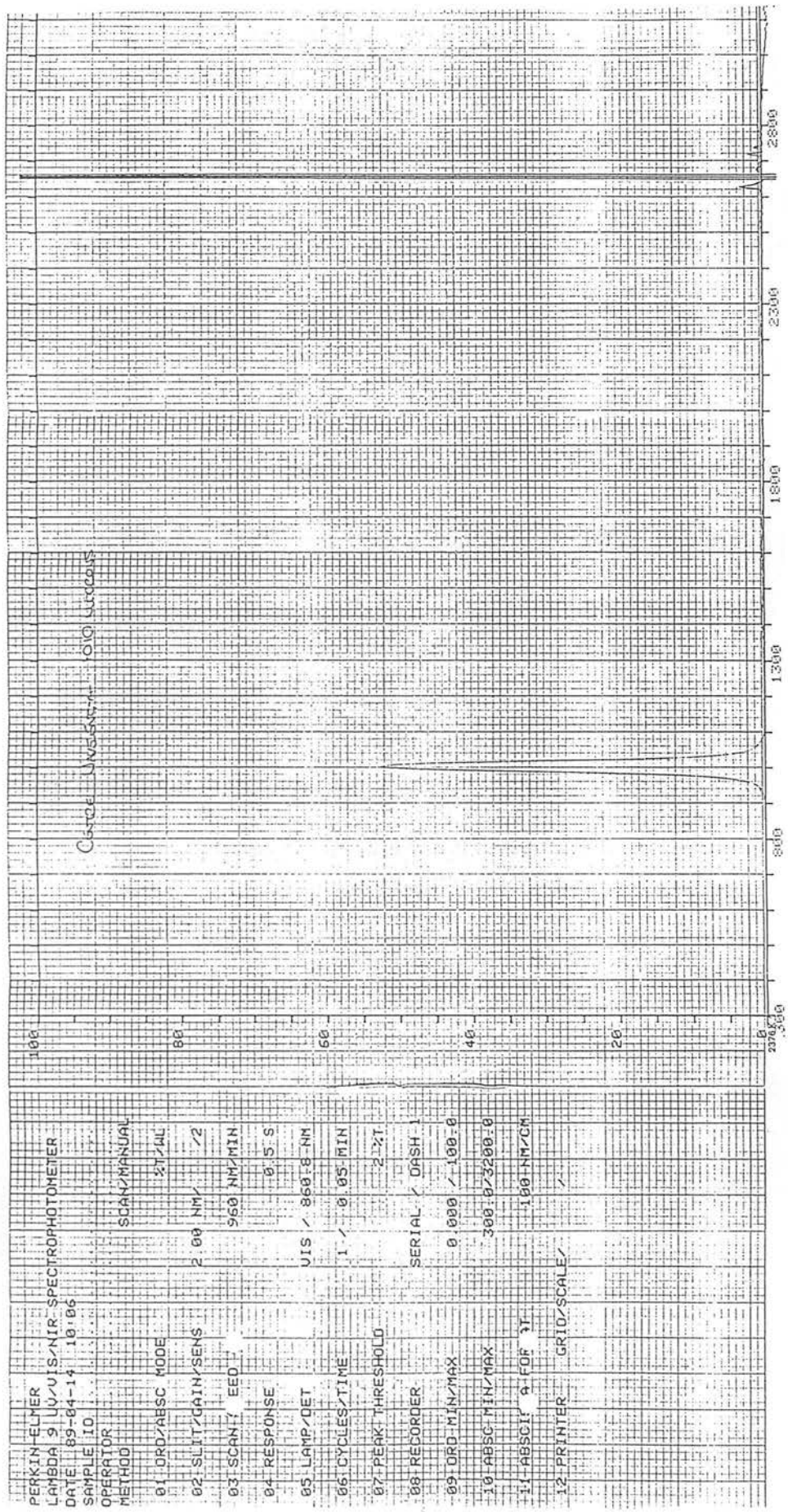

Transmission Curve for Filter U2

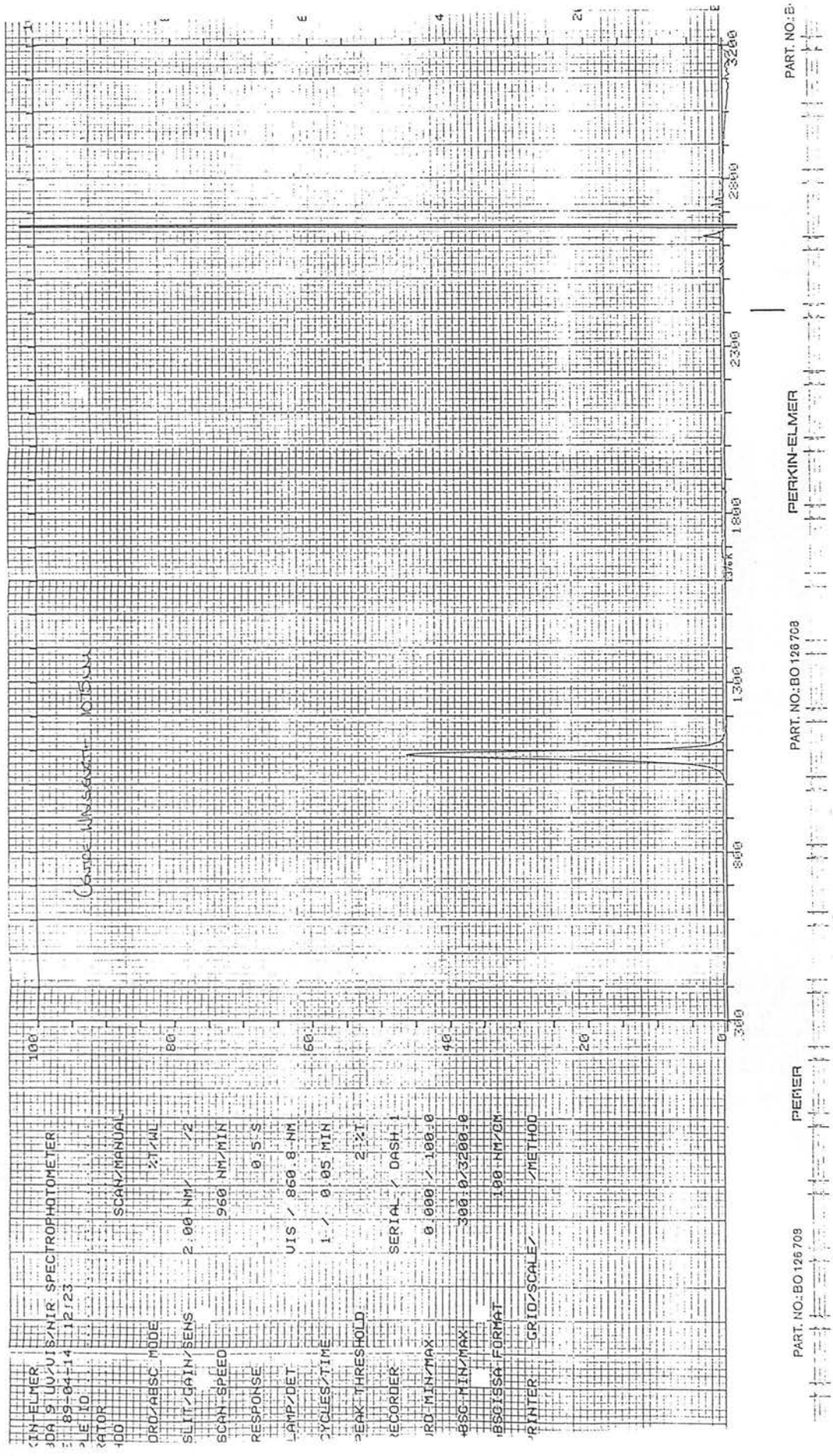

Transmission Curve for Filter U3

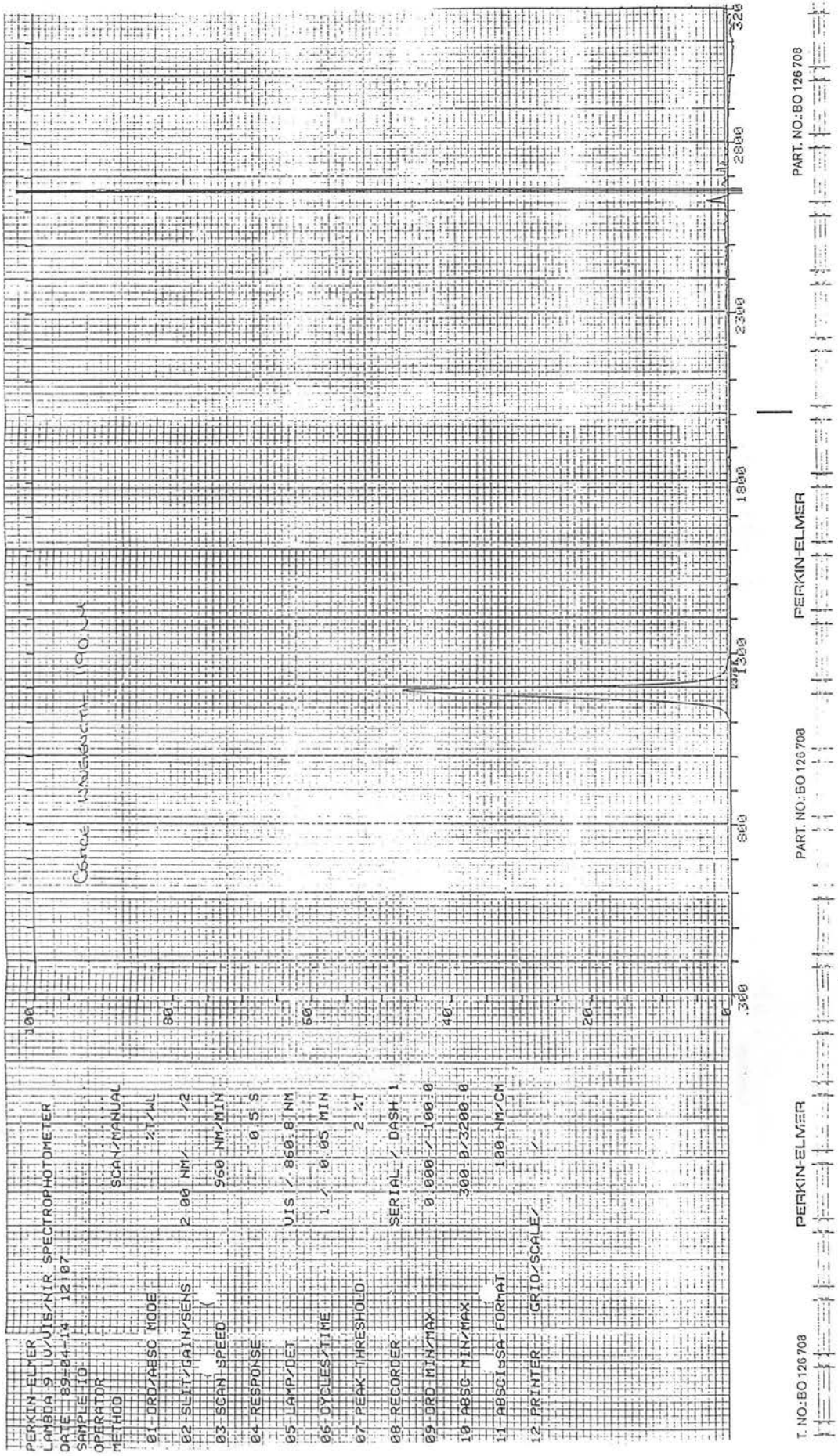

Transmission Curve for Filter U4

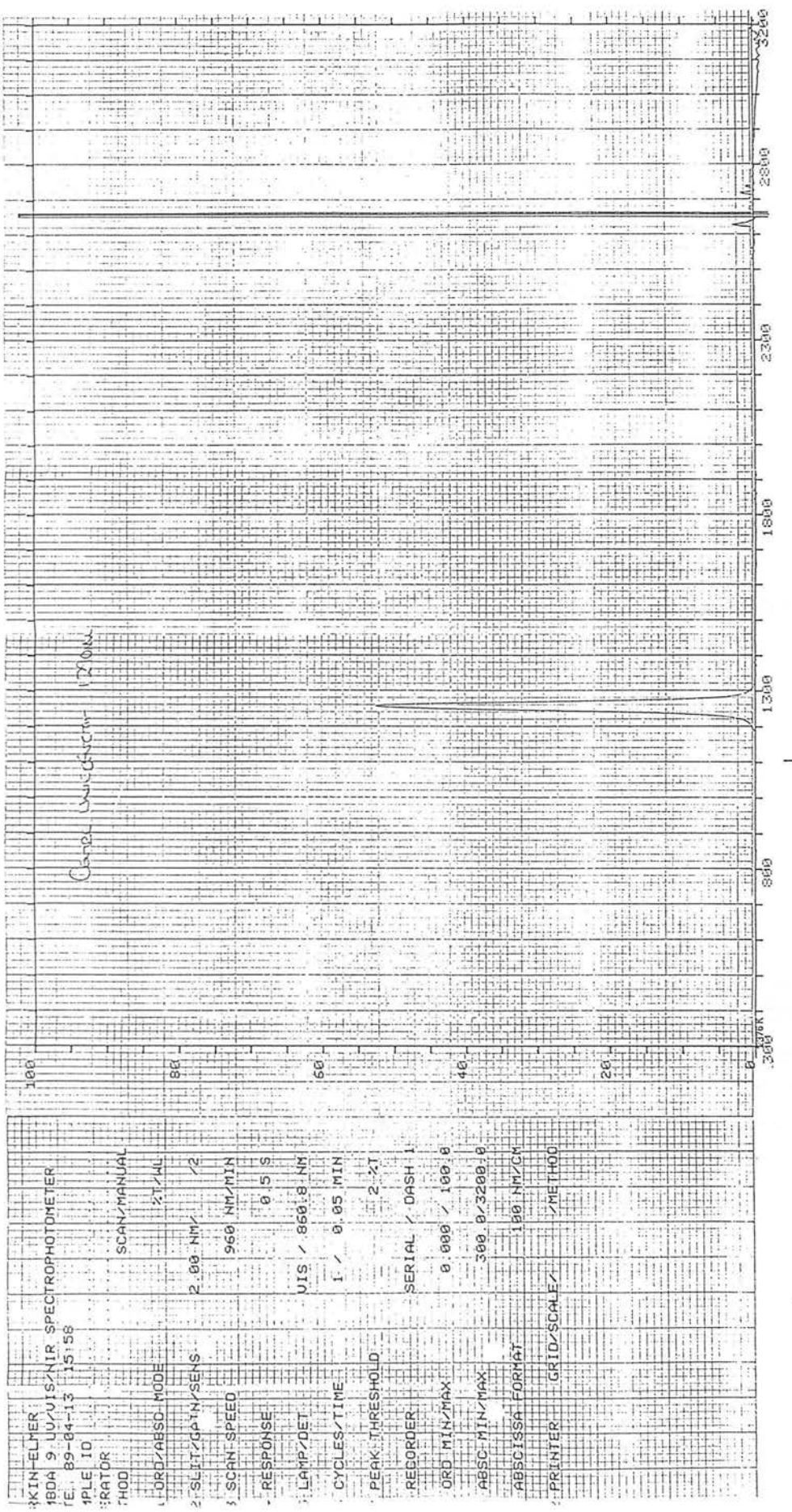

Transmission Curve for Blocking Filter WG 230

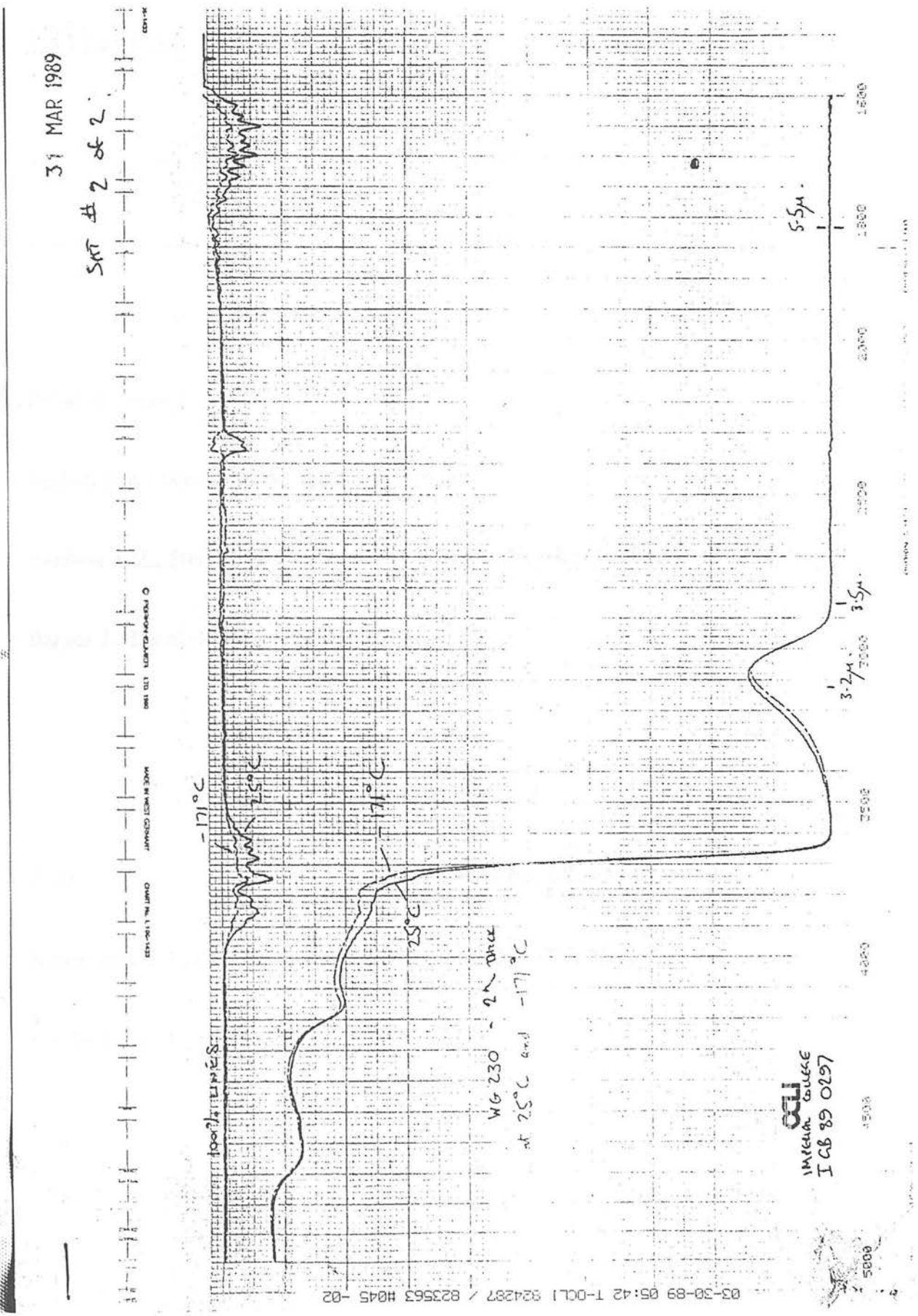

Bibliography

Alpher R.A., Bethe H.A., Gamow G., 1948, Phys Rev, 73, 803

Aragón-Salamanca A., 1991, PhD Thesis, University of Durham

Aragón-Salamanca A., Ellis R.S., Couch W.J., Carter D., 1993, MNRAS, 262, 764

Babul A., Rees M.J., 1992, MNRAS, 255, 346

Bachall N.A., Soneira R.M., 1983, ApJ, 270, 20

Bardeen J.M., Steinhardt P.J., Turner M.S., 1983, Phys Rev D, 28, 679

Barnes J., Efstathiou G., 1987, ApJ, 319, 575

Baron E., White S.D.M., 1987, ApJ, 322, 585

Blumenthal G.R., Faber S.M., Primack J.R., Rees M.J., 1984, Nat, 311, 517

Broadhurst T.J., Ellis R.S., Shanks T., 1988, MNRAS, 235, 827

Broadhurst T.J., Ellis R.S., Glazebrook K., 1992, Nat, 355, 55

Brocklehurst M., 1971, MNRAS, 153, 471

Butcher H., Oemler A., 1978, ApJ, 219, 18

Butcher H., Oemler A., 1984, ApJ, 285, 426

Caldwell N., Rose J.A., Sharples R.M., Ellis R.S., Bower R.G., 1993, AJ, 106, 473

Chapman C., Beard S., Mountain M., Pettie D., Pickup P., 1990, SPIE, 1235, 34

Charlot S., Fall S.M., 1993, ApJ, 415, 580

Chernin A.D., 1970, ZhETF, 11, L317

Colless M., Ellis R.S., Taylor K., Hook, R.N., 1990, MNRAS, 244, 408

Colless M., Ellis R.S., Broadhurst T.J., Taylor K., Peterson B.A., 1993, MNRAS, 261, 19

Collins C.A., Joseph R.D., 1988, MNRAS, 235, 209

Collins C.A., Nichol R.C., Lumsden S.L., 1992, MNRAS, 254, 295

Couch W.J., Sharples R.M., 1987, MNRAS, 229, 423

Cowie L.L., 1988, in Kaiser N., Lasenby A., eds, NATO ASI Series C, 240, The Post-Recombination Universe, Kluwer, Dordrecht, p1

Cowie L.L., 1991, in Shanks T., Banday A.J., Ellis R.S., Frenk C.S., Wolfendale A.W., eds, NATO ASI Series C, 348, Observational Tests of Cosmological Inflation, Kluwer, Dordrecht, p25

Davis M., Wilkinson D.T., 1974, ApJ, 192, 251

Demarque P., Deliyannis C.P., Sarajedini, A., 1991, Observational Tests of Cosmological

Inflation, Kluwer, Dordrecht, p111

De Propris R., Pritchet C.J., Hartwick F.D.A., Hickson P., 1993, AJ, 105, 1243

Djorgovski S., Strauss M.A., Spinrad H., Perley R., McCarthy P., 1987, AJ, 93, 1318

Djorgovski S., 1992, in de Carvalho R.R., ed, ASP Conf Series, Cosmology and Large Scale Structure in the Universe

Djorgovski S., Thompson D.J., 1992, in Barbury B., Renzini A., eds, Proc. IAU Symp. 149, The Stellar Populations of Galaxies, Kluwer, Dordrecht, p337

Doroshkevich A.G., 1970, Astrofizika, 6, 581

Dressler A., 1993, in Sato, K., ed, Proc Yamada Conf XXXVII, Evolution of the Universe and its Observational Quest, Universal Acad Press, in press

Eales S.A., Rawlings S., 1993, ApJ., 411, 67

Efstathiou G., Ellis R.S., Peterson B.A., 1988, MNRAS, 232, 431

Efstathiou G., Bernestein G., Katz N., Tyson J.A., Guhathakurta P., 1991, ApJ, 380, 147

Elbaz D., Arnaud M., Cassé M., Mirabel I.F., Prantzos N., Vangioni-Flam E., 1992, A&A, 265, L29

Ellis R.S., 1993 in Sato, K., ed, Proc Yamada Conf XXXVII, Evolution of the Universe and its Observational Quest, Universal Acad Press, in press

Frenk C.S., White S.D.M., Davis M., 1983, ApJ 271, 417

Glazebrook K.G., 1991, PhD Thesis, University of Edinburgh

Glazebrook K.G., Peacock J.A., Collins C.A., Miller L., 1993, MNRAS, in press

Guth A. H., 1981, Phys Rev D, 23, 347

Gunn J.E., Tinsley B.M., 1975, Nat, 257, 454

Hartwick F.D.A., Schade D., 1990, ARA&A, 28, 437

Hubble E., 1926, ApJ, 63, 236

Hubble E., 1929, Proc NAS, 15, 168

Jones, B.J.T., 1973, ApJ, 181, 269

Jones L.R., Fong R., Shanks T., Ellis R.S., Peterson B.A., 1991, MNRAS, 249, 481

Kaiser N., 1984, ApJ, 284, L9

Kennicutt R.C., 1983, ApJ, 272, 54

Kennicutt R.C., Keel W.C., van der Hulst J.M, Hummel E., Roettiger K.A., 1987, AJ, 93, 1011

Kitchin, C. R., 1984, Astrophysical Techniques, Adam Hilger, Bristol

Koo D.C., 1981, PhD Thesis, University of California

Koo D.C., 1986, in Chiosi C., Renzini A., eds, Spectral Evolution of Galaxies, Reidel, Dordrecht, p419

Koo D.C., Kron R.G., 1980, PASP, 92, 537

Koo D.C., Kron R.G., Cudworth K.M., 1986, PASP, 98, 285

Kunth D., Sargent W.L.W., 1986, ApJ, 300, 496

Larson, R.B., 1974, MNRAS, 166, 585

Lilly S.J., Cowie L.L., Gardner J., 1991, ApJ, 369, 79

Longair M.S., 1981, High Energy Astrophysics, Cambridge University Press, Cambridge

Longair M.S., 1984, Theoretical Concepts in Physics, Cambridge University Press, Cambridge

Loveday J., Efstathiou G., Peterson B.A., Maddox S.J., 1992, ApJ, 400, 43

Lowenthal J.D., Hogan C.J., Leach R.W., Schmidt G.D., Foltz C.B., 1990, ApJ, 357, 3

McCarthy P.J., Spinrad H., Djorgovski S., Strauss M., van Breugal W., Liebert J., 1987, ApJ, 319, L39

McCarthy P.J., Spinrad H., van Breugal W., Liebert J., Dickinson M., Djorgovski S., Eisenhardt P., 1990, ApJ, 365, 487

Maddox S.J., Efstathiou G., Sutherland W. J., Loveday J., 1990, MNRAS, 242, 43P

Mather J.C. et al., 1990, ApJ, 354, L37

Meier D.L., 1976, ApJ, 207, 343

Metcalfe N., Shanks T., Fong R., 1991, MNRAS, 249, 498

Miralda-Escudé J., Ostriker J.P., 1990, ApJ, 350, 1

Moore B., Frenk C.S., Weinberg D.H., Saunders W., Lawrence A., Ellis R.S., Kaiser N., Efstathiou G., Rowan-Robinson M., 1992, MNRAS, 256, 477

Mountain C.M., Robertson D.J., Lee T.J., Wade R., 1990, in Crawford D.L., ed, Proc. SPIE 1235, Instrumentation in Astronomy VII, SPIE, Bellingham, p25

Murdoch H.S., Hunstead R.W., Pettini M., Blades J.C., 1986, ApJ, 309, 19

Partridge R.B., 1974, ApJ, 192, 241

Partridge R.B., Peebles P.J.E., 1966, ApJ, 147, 868

Peacock J.A., 1987, in Kundt W., ed, Astrophysical Jets and their Engines, NATO ASI Series C, Vol 208, Reidel, Dordrecht

Peebles P.J.E., 1992, ApJ 258, 415

Peebles P.J.E., 1993, Principles of Physical Cosmology, Princeton University Press, Princeton, New Jersey

Penzias A.A., Wilson R.W., 1965, ApJ, 142, 419

Pickles A.J., van der Kruit P.C., 1991, A&AS, 91, 1

Plionis M., Coles P., Catelan P., 1993, MNRAS, 262, 465

Press W.H., Flannery B.P., Teukolsky S.A., Vetterling W.T., 1986, Numerical Recipies, Cambridge University Press, Cambridge

Pritchet C.J., Hartwick, F.D.A., 1987, ApJ, 320, 464

Pritchet C.J., Hartwick, F.D.A., 1990, ApJ, 355, L11

Quinn P.J., Goodman J., 1986, ApJ, 309, 472

Radford S.J.E., Brown R.L., Vanden Bout P.A., 1993, A&A, 271, L21

Ramsay S.K., Mountain C.M., Geballe T.R., 1992, MNRAS, 259, 751

Rees M.J., 1986, MNRAS, 218, 25P

Rowan-Robinson M. et al., 1990, MNRAS, 247, 1

Rowan-Robinson M. et al., 1991, Nat, 351, 719

Rowan-Robinson M., et al., 1993, MNRAS, 261, 513

Rubin V.C., 1991, in Cornell, J., ed, Bubbles, Voids and Bumps in Time: the New Cosmology, CUP, Cambridge

Sandage A., 1986, A&A, 161, 89

Sargent W.L.L., Young P.J., Boksenberg A., Tytler D., 1980, ApJS, 42, 41

Saunders W., et al., 1991, Nat, 349, 32

Schneider D.P., Schmidt M., Gunn J.E., 1989, AJ, 98, 1951

Schneider D.P., Schmidt M., Gunn J.E., 1991, AJ, 102, 837

Shane C.D., Wirtanen C.A., 1967, Pub Lic Obs, 22

Silk J., Szalay A., 1987, ApJ, 323, L107

Smoot, F.G. et al., 1992, ApJ, 396, L1

Soifer B.T., Sanders D.B., Madore B.F., Neugebauer G., Danielson G.E., Elias J.H., Lonsdale C.J., Rice W.L., 1987, ApJ, 320, 238

Songaila A., Cowie L.L., Lilly S.J., 1990, ApJ, 348, 371

Thompson D.J., Djorgovski S., Trauger, J., 1993, in de Carvalho R.R., ed, ASP Conference Series 24, Cosmology and Large Scale Structure in the Universe, Astronomical Soc Pacific, San Fransisco, p147

Turner E.L., 1993, in Sato, K., ed, Proc Yamada Conf XXXVII, Evolution of the Universe and its Observational Quest, Universal Acad Press, in press

Tyson A.J., 1988, AJ, 96,1

van den Bergh, S., 1990, QJRAS, 31, 153

Walker T.P. et al., 1991, ApJ, 376, 51

Wasserman I., 1978, ApJ, 224, 337

Weinberg S., 1972, Gravitation and Cosmology, Wiley, New York

Weyman R.J., Carswell R.F., Smith M.G., 1981, ARA&A, 19, 41

White S.D.M., Frenk C.S., Davis M., 1983, ApJ, 274, L1

White S.D., Frenk C.S., 1991, ApJ, 379, 52

Whitmore B.C., Schweizer F., Leitherer C., Borne K., Robert C., 1993, AJ, 106, 1354

Winget D.E., Hansen C.J., Liebert J., Van Horn H.M., Fontaine G., Nather R.E., Kepler S.O., Lamb D.Q., 1987, ApJ, 315, L77

Wolfe A.M., 1986, Phil Tran R Soc$\mathbb{A}$, 320, 503